DEVELOPMENT OF NOVEL COMPACT ULTRASHORT PULSE LASERS FOR BIOMEDICAL APPLICATIONS

DIANA GALIAKHMETOVA

Doctor of Philosophy

ASTON UNIVERSITY

Aston Institute of Photonic Technologies

November 2023

© Diana Galiakhmetova, 2023

Diana Galiakhmetova asserts her moral right to be identified as the author of this thesis

This copy of the thesis has been supplied on condition that anyone who consults it is understood to recognise that its copyright belongs to its author and that no quotation from the thesis and no information derived from it may be published without appropriate permission or acknowledgement.

Aston University
Aston Institute of Photonic Technologies

Development of novel compact ultrashort pulse lasers for biomedical applications

Diana Galiakhmetova

Doctor of Philosophy

2023

Lasers have established their ubiquity across a broad spectrum of applications, ranging from manufacturing and communication to entertainment, and the medical field is no exception. However, biomedical applications place unique demands on laser parameters such as operating mode, wavelength, and output power. Furthermore, the physical characteristics of the laser must include reliable operating stability, high resistance to fluctuations of environmental conditions, and compact size.

The requirements for these laser parameters strongly depend on the specific application, as different laser modes, irradiation levels, and exposure durations cause diverse effects on various tissue types. Therefore, a comprehensive understanding of light-tissue interaction with the target tissues is essential before designing lasers for biomedical purposes.

This thesis provides experimental and computational research, shedding light on the interaction of post-mortem mouse head tissues with continuous-wave light and ultrashort pulses. The study reveals the tissue penetration depth of single- and multi-layers of skin, skull, and brain in visible and near-infrared ranges, providing valuable information about their optical properties and required laser parameters for non- or minimal invasive neurostimulation.

The dissertation is devoted to the improvement of neurostimulation methods, including a comprehensive study of the optical properties of light-sensitive proteins applicable as optogenetic tools and fluorescent biomarkers and the development of a compact ultrashort-pulse high-peak-power laser system for optogenetic research on *in vivo* animal samples.

In addition, the work presents a developed tunable fibre laser operating at wavelengths of 850 nm and 1700 nm that can be used as a versatile light source in the multimodal cancer detection system.

The work presented in the dissertation includes the development of different laser sources intended for applications in biomedical research, neurophotonics, and tumour diagnostics.

Keywords: Light-tissue interaction, oncology, optogenetics, phytochrome, fibre laser.

Acknowledgements

I want to express my deepest gratitude to my supervisors, Edik Rafailov and Sergei Sokolovski, who mentored my PhD journey, giving advice not only about scientific research, pushing me to write and re-write papers until perfection but also providing valuable resources about various grants and competitions for PhD students that helped me to improve my CV. I am thankful for the activities outside the university and the opportunity to degustation a wide range of world cuisine and discuss Persian restaurants in Birmingham. And special thanks for the jokes and optimistic point of view on the world.

I want to thank my colleagues Dr Natalia Bazieva, Dr Amit Yadav, Dr Dmitrii Stoliarov, Dr Viktor Dremin, and Dr Aleksandr Koviarov for their mentorship and help in spectrophotometric measurements, computer modelling of light-tissue interactions, and laser development. Also, I am very grateful for the funny stories and for cheering me up in the periods when all experiments went down.

Thanks to many current and graduated PhD students for various bright events in the third-floor kitchen. Thanks to Nasir, Paulami, Gabriella, Karina, Manuel, Juan, Shirin, Arooj, and many-many others.

Separate gratitude to my friends Liliya, Aizira, Elvina, Ramilya, Arthur, Sasha, and Artem. I am happy that for more than nine years, we continue to be friends, supporting each other, even living in different countries.

Additional thanks to a French guy, Florent Bessin, a personal teacher of the nonlinear effects in fibre optics. I do not have enough words to thank you for your patience, help, and 24/7 support.

And the prominent, special thanks to my family, who listened to hours of complaining, cries, and worries and always supported me on each step of my life. Great thanks to my “twin”, Liana. You know you are the best sister ever, and I am so lucky to have you in my life.

The work was financially supported by the Return to Research Grant, The Rank Prize Optoelectronics.

Contents

List of Publications

Peer-Reviewed Journals

Galiakhmetova, D., Gladush, Y., Mkrtchyan, A., Fedorov, F.S., Khabushev, E.M., Krasnikov, D.V., Chinnambedu-Murugesan, R., Manuylovich, E., Dvoyrin, V., Rozhin, A., Rümmeli, M., Alyatkin, S., Lagoudakis, P. and Nasibulin, A., 2021. Direct measurement of carbon nanotube temperature between fiber ferrules as a universal tool for saturable absorber stability investigation. Carbon, 184, pp.941-948;

Galiakhmetova, D., Dremin, V., Koviarov, A., Stoliarov, D., Ngum, N., Murugesan, R.C., Parri, R., Sokolovski, S. and Rafailov, E.U., 2022. Ultra-short laser pulses propagation through mouse head tissues: experimental and computational study. IEEE Journal of Selected Topics in Quantum Electronics, 29(4: Biophotonics), pp.1-11;

Stoliarov, D., Koviarov, A., Korobko, D., Galiakhmetova, D. and Rafailov, E., 2022. Fibre laser system with wavelength tuning in extended telecom range. Optical Fiber Technology, 72, p.102994;

Galiakhmetova, D., Koviarov, A., Dremin, V., Stoliarov, D., Gorodetsky, A., Maimaris, M., Shcherbakova, D., Baloban, M., Sokolovski, S., Verkhusha, V. and Rafailov, E., 2023. Optical properties of photosensory core modules of dimeric and monomeric bacterial phytochromes. Angewandte Chemie (Under Review);

Stoliarov, D., Koviarov, A., Manuylovich, E., Galiakhmetova, D. and Rafailov, E., 2023. Gain-Managed Nonlinear Amplification of ultra-long mode-locked fiber laser. Optics Express, 31(26), 43427-43437;

Galiakhmetova, D., Koviarov, A., Dremin, V., Stoliarov, D., Shcherbakova, D., Baloban, M., Verkhusha, V., Sokolovski, S. and Rafailov, E, 2023. Non-linear fluorescence of dimeric and monomeric *Deinococcus radiodurans* phytochromes. Biophysical Journal (Under Review).

Conference Proceedings

Galiakhmetova, D., Dremin, V., Koviarov, A., Stoliarov, D., Ngum, N., Parri, R., Sokolovski, S. and Rafailov, E., 2022, May. Evaluation of penetration depth of near-infrared irradiation generated by tunable ultra-short pulsed laser in *ex vivo* samples of mouse head. In Tissue Optics and Photonics II (Vol. 12147, pp. 45-51). SPIE;

Koviarov, A., Stoliarov, D., Galiakhmetova, D. and Rafailov, E. (2022, June). “Efficient frequency doubling of soliton self-frequency shifted ultrashort pulses.” 2022 International Conference Laser Optics (ICLO) (pp. 1-1). IEEE;

Galiakhmetova, D.I., Koviarov, A.S., Dremin, V.V., Gorodetsky, A.A., Maimaris, M., Stoliarov, D.A., Baloban, M., Verkhusha, V.V., Sokolovski, S.G. and Rafailov, E.U., 2023, March. Linear and nonlinear photoconversion of monomeric and dimeric *DrBphP* bacterial phytochrome variants. In Optogenetics and Optical Manipulation 2023 (p. PC123660H). SPIE (**The first-place winner JBO/NEUROPHOTONICS 3-Minute Poster Competition**);

Galiakhmetova, D., Dremin, V., Koviarov, A., Stoliarov, D., Ngum, N., Parri, R., Sokolovski, S. and Rafailov, E., 2023, March. Ultrashort pulsed laser in deep head tissues penetration for non-invasive optogenetics in near-IR windows (Conference Presentation). In Optical Biopsy XXI: Toward Real-Time Spectroscopic Imaging and Diagnosis (p. PC123730A). SPIE (**Invited**);

Koviarov, A., Stoliarov, D., Galiakhmetova, D. and Rafailov, E., 2023, March. Highly efficient frequency doubling of 1700 nm ultrashort pulsed fiber laser in PPLN bulk crystal. In Nonlinear Frequency Generation and Conversion: Materials and Devices XXII (p. PC124050S). SPIE;

Galiakhmetova, D.I., Koviarov, A.S., Dremin, V.V., Gorodetsky, A.A., Maimaris, M., Stoliarov, D.A., Baloban, M., Verkhusha, V.V., Sokolovski, S.G. and Rafailov, E.U., 2023, August. Comparison of nonlinear properties of monomer and dimer of bacterial phytochrome from *Deinococcus radiodurans*. In Translational Biophotonics: Diagnostics and Therapeutics III (Vol. 12627, pp. 255-257). SPIE;

Stoliarov, D., Manuylovich, E., Koviarov, A., Galiakhmetova, D. and Rafailov, E., 2023, June. Spectral broadening of low repetition rate pulses in a fibre gain-managed nonlinear amplifier. In The European Conference on Lasers and Electro-Optics (p. cj_p_9). Optica Publishing Group;

Koviarov, A., Stoliarov, D., Galiakhmetova, D. and Rafailov, E., 2023, June. Highly efficient frequency doubling of ultrashort-pulse fiber laser at 1700 nm in PPLN bulk and waveguide crystals. In The European Conference on Lasers and Electro-Optics (p. cj_p_23). Optica Publishing Group.

Other Presented Works

Galiakhmetova, D., Dremin, V., Koviarov, A., Stoliarov, D., Ngum, N., Parri, R., Chinnambedu-Murugesan, R., Sokolovski, S. and Rafailov, E., 2022, August. Attenuation of near-infrared light in *ex vivo* samples of mouse head: experimental and computational studies. In VI 'Photonics Meets Biology' Summer School and Workshop 2022, Spetses, Greece (**Winner of the Best Elevator Pitch Award**);

Galiakhmetova, D.I., Koviarov, A.S., Dremin, V.V., Gorodetsky, A.A., Maimaris, M., Stoliarov, D.A., Baloban, M., Verkhusha, V.V., Sokolovski, S.G. and Rafailov, E.U., 2023, October. Enhancing optogenetics: first demonstration of nonlinear properties of monomeric and dimeric *Deinococcus radiodurans* bacterial phytochrome. In 17th International conference on Laser Applications in Life Sciences, Mugla, Turkey;

Galiakhmetova, D.I., Koviarov, A.S., Dremin, V.V., Gorodetsky, A.A., Maimaris, M., Stoliarov, D.A., Baloban, M., Verkhusha, V.V., Sokolovski, S.G. and Rafailov, E.U., 2023, November. Non-invasive Optogenetics: Pipedream or Impending Reality. In “Women in Photonics” Workshop, Jena, Germany (**Winner of Travel Grant**).

List of Abbreviations

AOM – Acousto-Optic Modulator;

Ar – Argon;

BDF – Bismuth-Doped Fibre;

BDFL – Bismuth-Doped Fibre Laser;

Bi – Bismuth;

BPF – Bandpass Filter;

BV – Biliverdin;

CNT – Carbon Nanotube;

CW – Continuous Wave;

DCF – Dispersion Compensating Fibre;

DSF – Dispersion-Shifted Fibre;

EDF – Erbium-Doped Fibre;

EDFA – Erbium Fibre Amplifier;

EDFL – Erbium-Doped Fibre Laser;

Er – Erbium;

EYDF – Erbium-Ytterbium-Doped Fibre;

FBG – Fibre Bragg Grating;

FOPO – Fibre Optical Parametric Oscillator;

FWHM – Full Width Half Maximum;

FWM – Four-Wave Mixing;

He-Cd – Helium Cadmium;

He-Ne – Helium-Neon;

HNLF – Highly Nonlinear Fibre;

Ho – Holmium;

HWP – Half-Wave Plate;

IAD – Inverse Adding-Doubling;

ISO – Isolator;

Kr – Krypton;

LD – Laser Diode;

LMA – Large Mode Area;

LPF – Long Pass Filter;

MO – Master Oscillator;

MMF – Multimode Fibre;

NALM – Nonlinear Amplifying Loop Mirror;

Nd – Neodymium;

ND – Neutral Density;

NIR – Near-Infrared;

NLF – Nonlinear Fibre;

NLP – Noise-Like Pulse;

OCT – Optical Coherent Tomography;

OM – Output Module;

OPA – Optical Parametric Amplifier;

OPO – Optical Parametric Oscillator;

PC – Polarisation Controller;

PCF – Photonic Crystal Fibre;

PCM – Photosensory Core Module;

PDF – Praseodymium-Doped Fibre;

PM – Polarisation-Maintaining;

PPLN – Periodically Poled Lithium Niobate;

RBW – Resolution Bandwidth;

RF – Radio Frequency;

RM – Roof Mirror;

PP – Pulse Picker;

Pr – Praseodymium;

QWP – Quarter-Wave Plate;

SA – Saturable Absorber;

SBS – Stimulated Brillouin Scattering;

SC – Supercontinuum;

SESAM – Semiconductor Saturable Absorber Mirror;

SHG – Second Harmonic Generation;

SMF – Single Mode Fibre;

SPM – Self-Phase Modulation;

SRS – Stimulated Raman Scattering;

SSFS – Soliton Self-Frequency Shift;

Ti:Sa – Titanium-Sapphire;

Tm – Thulium;

TDF – Thulium-Doped Fibre;

TDFL – Thulium-Doped Fibre Laser;

UR – Unidirectional Ring;

UV – Ultraviolet;

VIS – Visible;

VLMA – Very Large Mode Area;

WDM – Wavelength Division Multiplexer;

Yb – Ytterbium;

YDF – Ytterbium-Doped Fibre;

YDFL – Ytterbium-Doped Fibre Laser.

List of Figures

List of Tables

Chapter 1

Introduction

In the last centuries, life science research and medicine have seen remarkable improvements through the integration of light sources in diagnosing and treating diseases. Optical techniques have proven exceptionally versatile, extending beyond traditional physical examinations, electrical or magnetic methods, pharmaceutical treatments, and surgical procedures. Most examination and therapy procedures use light-based clinical techniques such as optical coherence tomography (OCT), bioimaging, fluorescence, diffuse correlation, elastic, Raman, and Brillouin scattering spectroscopy, phototherapy, and laser surgery.

The principal advantage of optical techniques in diagnostics is their non-invasive nature, which minimises disruption to biological functions and mitigates impact on the surrounding areas [1].

Biomedical optical techniques use a variety of light sources, including lamps, diodes, gas, liquid, and solid-state lasers. These sources may have various sizes, shapes, working physical principles, and operating characteristics, including output power, operating modes, and wavelengths. The most used laser types operating in the ultraviolet (UV), visible (VIS), and near-infrared range (NIR) are shown in Figure 1.1 [1]-[13].

Ultraviolet range covers light wavelengths from 100 nm to 400 nm [4]. The primary laser sources operating in that spectral region are excimer lasers, which consist of a mix of halogen and noble gases [5]. These lasers are characterised by a high average power of hundreds of watts and nanosecond pulse durations. The exceptionally high peak power offers their application for vision correction procedures.

Another laser operating in UV and VIS wavelengths (325 nm, 442 nm) is the Helium Cadmium (He-Cd) laser [13]. This gas laser usually emits coherent light caused by the gas discharge. The other common examples of VIS gas lasers include Argon (Ar) ion (488-514 nm), Krypton (Kr) ion (531-569 nm), and Helium-neon (He-Ne) (633 nm) lasers [6]. The first two find application in ophthalmology, dermatology, and blood coagulation methods, while the He-Ne laser is used for flow cytometry, gene sequencing and microscopy [1].

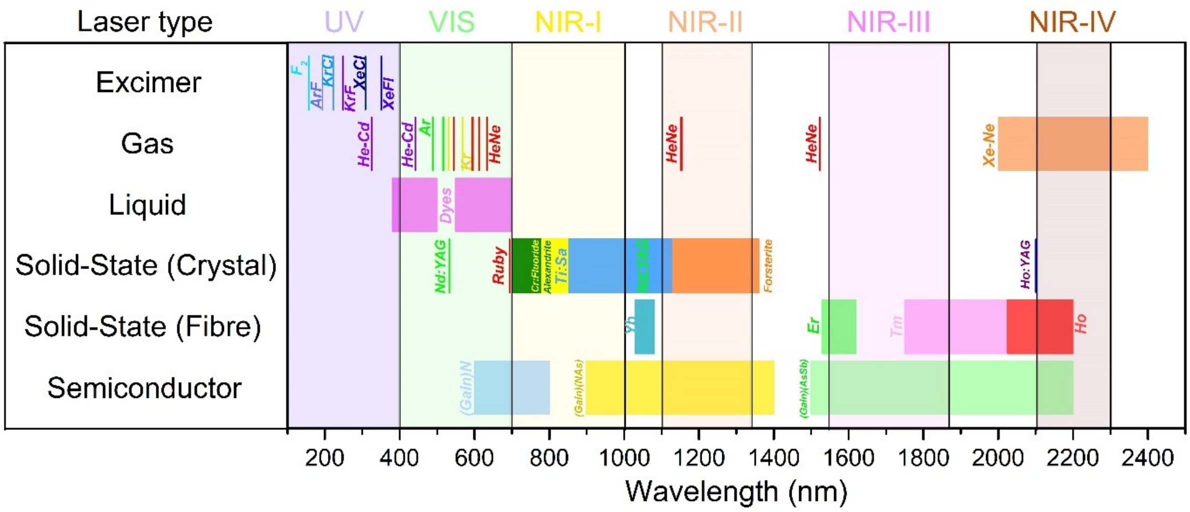

Figure 1.1. Various laser source types used for biomedical applications.

As well as gas and liquid lasers, solid-state lasers can operate in the VIS range (400-700 nm). For example, Neodymium:YAG (Nd:YAG) can be used to generate the second harmonic at 532 nm, while Ruby emits light at 694 nm wavelength. However, the majority of solid-state lasers operate in NIR spectral range (700-2500 nm): Alexandrite, Titanium-sapphire (Ti:Sa), Cr:Forsterite, and Holmium:YAG (Ho:YAG) [2], [7], [8], [14]. These lasers are actively used in biomedicine: Ruby and Alexandrite lasers in cosmetology [15] and dermatology [16], [17], Ti:Sa in multiphoton microscopy [18], ND:YAG in oncology and urology [19], while Ho:YAG is used in kidney stone removal [1] and dentistry [20]. Crystal-based solid-state lasers have high peak power and exceptional beam quality; however, they are quite bulky and require expensive cooling systems.

Fibre lasers are another subcategory of solid-state lasers based on silica doped with rear-earth elements such as Erbium (Er), Thulium (Tm), Holmium (Ho), Ytterbium (Yb) or with Bismuth (Bi) ions [9]. Their advantages are compactness, relatively cheap price, and various operating modes. Depending on the wavelength, they have found applications in spectroscopy, arthroscopy, urology, and microsurgery [3].

Another class of lasers with a solid medium that is categorised separately is semiconductor or diode lasers. Their emission is generated through the recombination of charged pairs in a laser medium [10]. (GaIn)N, (AlGaIn)P, (GaIn)(NAs), and (GaIn)(AsSb) cover the spectral range from 400 nm to 2400 nm [11]. They are commonly used in OCT and confocal microscopy because of their relatively small size, low cost, and broad operation spectrum [12].

Each laser category offers unique advantages. For example, excimer and crystal-based solid-state laser systems provide high peak power, while fibre and semiconductor lasers are known for their compactness and relatively low cost. These lasers have found their niche in specific areas, trying to satisfy the main requirements of biomedical applications.

The requirements can be based not only on the laser operating wavelength but also on other parameters such as output power, irradiance, beam quality profile, and whether the laser source operates in continuous-wave (CW) or pulsed mode.

In the case of pulsed lasers, the repetition rate and pulse duration ranging from femtoseconds to nanoseconds become essential characteristics. Depending on the exposure time and irradiated area, lasers can cause various effects, such as stimulation of tissues, photoablation, thermal irradiation, tissue shrinking, evaporation or mechanical damage of different biotissues [1], [3]. Therefore, it is essential to know how various laser source parameters influence specific biological tissues for the effective use of lasers in biomedical applications.

To evaluate the effects of lasers on multilayer tissues, it is necessary to experimentally determine the light-tissue interaction, understanding how much of the light is reflected, scattered, and absorbed.

Considering that biological tissues have an uneven surface, granular structure or porosity, part of the incident light is reflected from the surface of the material. In addition, light can experience a scattering that occurs in all directions in tissue components such as proteins (collagen) and lipids (fat) [21].

Moreover, epithelial, connective, muscle, and nervous tissues have different spectral characteristics that depend on their components [22]. Various tissue substances, including proteins, water, melanin, and haemoglobin, absorb light and prevent its penetration into the deep tissues. Figure 1.2 shows the main components of biological tissues that absorb light and their absorption coefficients as a function of wavelength [23].

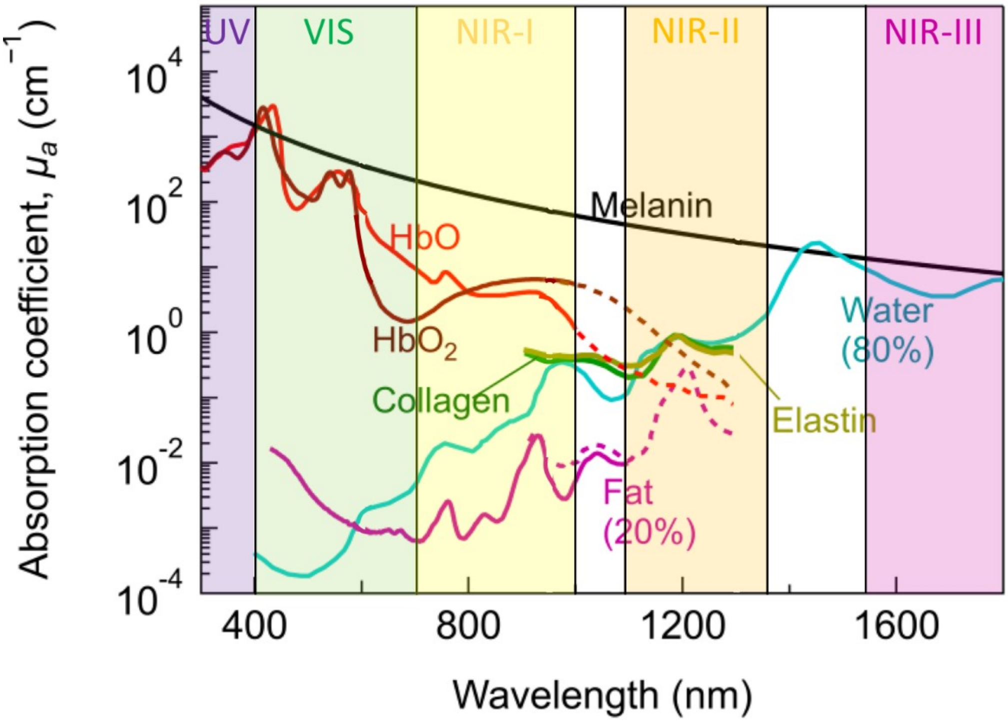

Figure 1.2. Absorption coefficients of various components of biotissues depending on the light wavelength [23].

The areas where the absorption of water, blood, melanin, and other proteins is relatively low are named biological or tissue transparency windows. Four near-infrared biological windows cover wavelength regions of 700-1000 nm (NIR-I), 1000-1350 nm (NIR-II), 1550-1870 nm (NIRIII), and 2100-2300 nm (NIR-IV) [24], [25] that are highlighted in Figures 1.1 and 1.2.

It is worth noting that there are a limited number of laser sources operating in these specific biological windows (Fig. 1.1). Understanding how different laser modes and various output parameters influence the light interaction with various biological tissues at these wavelengths remains a topic of research and requires a detailed study to determine which laser systems can be applied in the biomedical field.

Chapter 2 discusses the light-tissue interactions in skin, skull, and brain tissues. It includes a detailed post-mortem study of different mouse head tissue types and their components influencing light scattering and absorption. The second chapter consists of the demonstration and discussion of experimental results obtained from spectroscopic measurements and computer simulations, illustrating the penetration depth of various wavelengths. In addition, Chapter 2 presents a developed laser prototype operating at continuous-wave and pulsed modes in the NIR-I and NIR-II spectral ranges. This laser system was used for the experimental study to compare how CW light and femtosecond pulses interact with samples of single and multiple layers of mouse head tissues.

Understanding laser interaction with complicated multilayer biological tissues enables the development of laser systems designed to meet the specific requirements of diverse biomedical applications, such as dermatology, cardiology, angiology, dentistry, gastroenterology, ophthalmology, neurology, and oncology. Chapters 3 and 4 focus on developing lasers for optogenetics, while Chapter 5 is devoted to designing the laser system applicable to multimodal cancer diagnostics.

Chapter 3 focuses on neuroscience and manipulating neuron functionality using light. It reviews various light-sensitive proteins, such as opsins and phytochromes, and their role as optogenetic tools. In addition, the chapter demonstrates the potential improvement of current neurostimulation techniques using light. More precise and deeper light delivery to the brain cortex can be achieved by shifting the operating wavelength from the VIS to the NIR-II spectral range.

The third chapter includes the development of laser systems designed for biological research of the linear and nonlinear optical properties of light-sensitive proteins and the study of new genetically engineered truncated dimeric and monomeric variants of bacterial phytochromes. This study is the first demonstration of two-photon conversion and two-photon fluorescence in these protein samples, shedding light on their unique characteristics and implementation as optogenetic tools for improving neuroscience research.

Chapter 4 is devoted to the development of a compact ultrashort pulsed laser system that can be used for *in vivo* non- or minimal invasive neuronal stimulation of animals in biomedical and clinical conditions. The chapter includes a detailed review of lasers operating in the second tissue transparency window with a discussion of the optimal laser parameters required for neurostimulation. The fourth chapter consists of a detailed description of the development of the master oscillator (MO), preamplifier, and amplifier. The developed versatile, compact (34x46x46 cm), and tunable (1064-1170 nm) Ytterbium-doped fibre laser (YDFL) system has a reduced repetition rate of 608 kHz and reaches a pulse peak power of 82 kW at an average power of 250 mW. This level of peak power should be sufficient for two-photon conversion of light-sensitive proteins [26].

Chapter 5 presents the development of an ultrashort-pulse laser source operating in the NIR-I and NIR-III spectral regions that can be used in oncology detection techniques. The chapter overviews lasers operating in the third tissue transparency window, their advantages and disadvantages for biomedical research and clinical studies. It also discusses nonlinear optical effects in optical fibres that can be used to design a compact laser source operating in NIR-III. The chapter shows the development of a sub-180 fs laser system with an Erbium-doped fibre laser (EDFL) and amplifiers operating at wavelengths of 815–850 nm and 1625–1700 nm with an average power of hundreds of milliwatts. The developed laser system, combining 1.70 μm operating wavelength and second harmonic generation at 0.85 μm, can be used as a laser source for a versatile imaging technique for cancer detection and therapy monitoring.

Chapter 6 represents the overall discussion and conclusion of the studies presented in this thesis and demonstrates future works.

Chapter 2

Light-Tissue Interaction

2.1 Introduction

Understanding the optical properties of biological tissues is essential in advancing optical methods and bioimaging technologies for the early detection and treatment of various diseases. This knowledge is crucial in developing innovative approaches to minimise the thermal impact and potential tissue damage during medical therapies and imaging procedures.

Developing optical laser systems for biomedical applications requires a comprehensive study of light-tissue interactions. Although specific laser parameters may vary depending on the needs of specific biomedical research, a detailed analysis of the optical properties of various biotissues remains important.

To study how deeply light penetrates biological tissues, scientists mainly use spectroscopic methods. However, the experimental results of various research groups have shown significant differences between the values of the attenuation length. Figure 2.1 represents experimentally measured values of attenuation length for skin (blue), skull (green), and brain tissues (red) of mouse and rats depending on the wavelength [25], [27]-[32].

The agreement among experimental findings from different research groups is only in the general observation that light penetrates head tissues more deeply within the near-infrared transparency windows compared to the visible range. For skin, the average attenuation length in the visible spectrum is about 0.20 mm, while in I-IV optical windows, it is 0.40 mm, 0.44 mm, 0.47 mm, and 0.41 mm, respectively [25].

However, reaching a definitive conclusion for the skull attenuation length is more challenging due to variations in the measurements of skull optical properties across different studies. For example, M. Cano-Velazquez *et al.* [29] measured the transmittance of *ex vivo* mouse samples and demonstrated that the attenuation length of the skull bones varies from 0.20 mm (NIR-IV) to 0.75 mm (NIR-II and III). In contrast, measurements of the skull of 4-month-old rats by

S. Golovynskyi *et al.* [25] show a maximum value of 0.23 mm in all four near-infrared transparency windows.

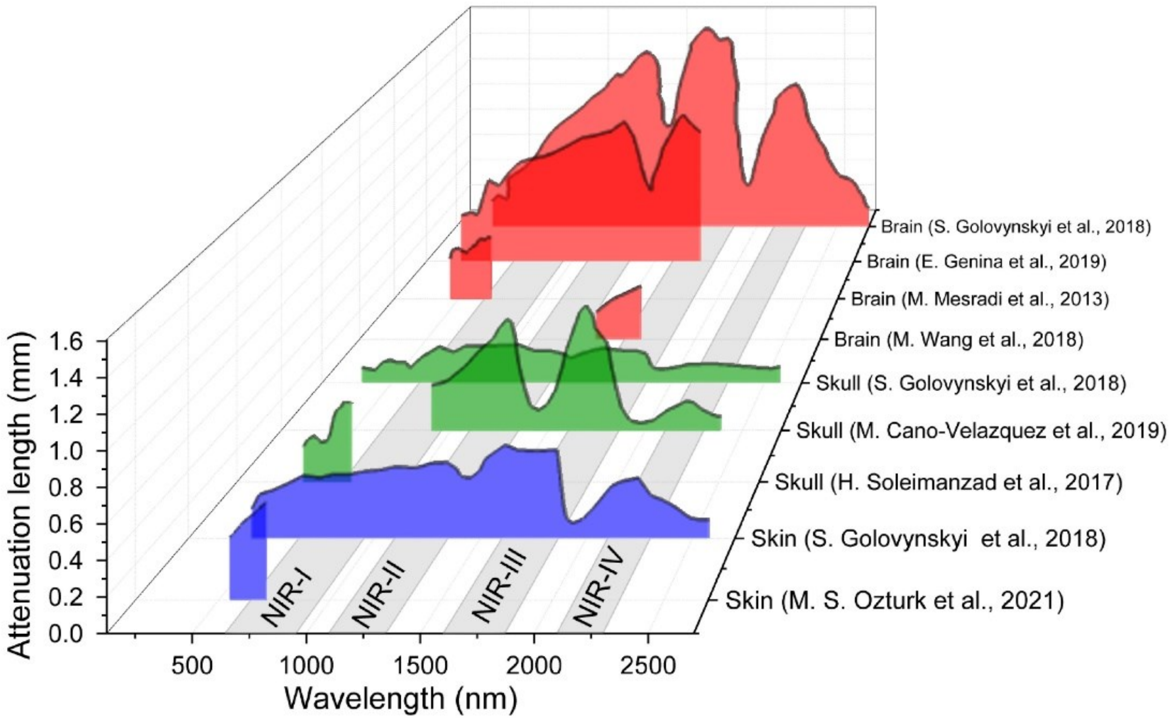

Figure 2.1. Attenuation length of brain, skull, and skin samples measured by different research groups.

Light penetration depth in brain tissues also depends on the measurement methods. For instance, M. Wang *et al.* [30] used a three-photon imaging technique with four pulsed excitation sources at a wavelength of 1450–1700 nm to measure the light propagation through the brain samples. The results demonstrated values of attenuation length varying from 173 μm to 410 μm which is three times smaller than values measured by E. Genina *et al.* [32] (0.6-1.1 mm) and S. Golovinskyi *et al.* [25] (0.8-1.55 mm) using a UV-3600 spectrophotometer with an integrating sphere for optical measurements of brain slices of healthy rats at the same wavelength range.

The explanation for the lack of agreement can include the diverse array of variations in the age of animals used in experiments and discrepancies in the thickness and composition of the tissue samples. Moreover, the contrasting experimental results reported in the literature may be explained by the different laser modes used in these studies. While spectrophotometers typically use standard halogen or deuterium lamps that emit continuous-wave light, three-photon imaging techniques use ultrashort pulsed lasers. Therefore, conducting additional research to understand how different laser modes and operating wavelengths influence the light penetration depth is fundamental in developing laser systems for medical therapies and imaging techniques to minimise heating and adverse effects on surrounding tissues.

According to studies [33]-[35], ultrashort pulse lasers penetrate deeper into biological tissues and cause less tissue heating than continuous-wave light due to high instantaneous power and prompt temperature distribution between pulses in tissues. For instance, the experimental results of J. Huang *et al.* [35] demonstrated that the femtosecond laser can deliver more energy, causing less heating of the samples than the continuous-wave laser. To investigate the thermal effect on freshly prepared pig skin samples, they used a 1035 nm ultrashort pulse laser with a tunable pulse duration of 300 fs – 10 ps.

In contrast, T. Ando *et al.* [36] demonstrated that the transmittance of laser power through mouse scalp and skull did not differ significantly for various laser pulse frequencies, which can be likely due to the thinness of the samples.

The contradiction in research papers prompted J. Hashmi *et al.* [34] to review nine studies with an experimental comparison of the tissue interaction with continuous-wave and pulsed light. Six papers [37]-[42] demonstrated the benefits of the use of pulsed lasers, while two other studies [43], [44] presented the opposite, and one work [45] did not show a difference between the effect of pulsed and CW light on biological tissues. However, it was noted that the benefits of one mode over another depend on the thickness and components of samples [46], [47].

The same outcomes were highlighted by R. Barbosa *et al.* [46], who compared light attenuation in rat and pig skin samples using 830 nm continuous-wave and 904 nm nanosecond pulsed lasers. The results of the experiments showed that in 1.17-1.63 mm thick rat samples, CW light attenuated more than pulses, while in pig skin, the effect was the opposite.

The study of another research group also demonstrated that various tissues influence light attenuation differently due to the individual composition and structure of the studied samples [47]. They showed that under the same experimental conditions, the 5-fs pulsed irradiation penetrated almost seven times deeper than continuous-wave light in chicken breast and only five times deeper in beef rib samples.

Furthermore, some reported studies have high observational error, unclear outcomes or different output characteristics for CW and pulsed lasers. Therefore, more precise investigations are needed for a detailed understanding of the light interaction with fresh head tissues. The study of CW and ultrashort pulsed light penetration through biological tissues has a significant influence on the development of novel laser sources for various biomedical applications, including *in vivo* multiphoton microscopy, cell manipulation, flow cytometry, optogenetics, and label-free imaging.

2.2 Materials and Methods

2.2.1 Sample Preparation

To study the interaction of near-infrared light with mouse head tissues, skin, skull, and brain samples from two healthy mice with background C57BL/6J were collected according to the standard procedure [48]. The mice were euthanised by administering an overdose of isoflurane followed by cervical dislocation. Local ethical review approved all experiments designed with the principles of replacement, refinement, and reduction.

The area of the forehead was shaved, and a skin sample of 1.5x1.5 cm was cut. The skin thickness was 0.5 mm, measured with a digital calliper. A 0.5 mm thick sample of the frontal and interparietal bones was cut out in a square shape and carefully removed from the mouse head to avoid brain damage. The brain sample was removed from the skull and cut into 1 mm thick layers from the cortex to the medulla. The schematic view of samples is presented in Figure 2.2 (a).

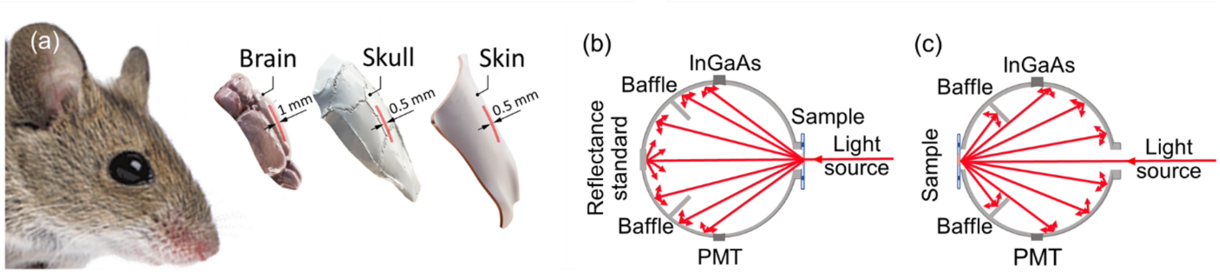

Figure 2.2. (a) Mouse head samples used for optical measurements: 1 mm thick mouse brain slice, 0.5 mm thick skull, and 0.5 mm thick skin; Schematic views of spectrophotometer configurations to measure (b) transmittance and (c) diffuse reflectance spectra.

All samples were kept on ice and used for optical experiments no later than 2 hours after mouse sacrification.

2.2.2 Spectrophotometer Setup

The transmittance and diffuse reflectance spectra of fresh samples were measured with a spectrophotometer (Lambda 1050+, PerkinElmer) with an integrating sphere. In the 300-2000 nm wavelength range, two different setups were used to measure spectra. In the first one, the sample was positioned between the integrating sphere and the light source, as shown in Figure 2.2 (b). The light transmitted through the sample was reflected by a reflectance standard that covered the second window of the integrating sphere and collected by a photodetector. In another configuration for diffuse reflectance measurements (Fig. 2.2 (c)), the light was reflected by a sample located in the second window of the integrating sphere.

To avoid tissue stretching and leakage, skin and brain samples were fixed between two microscopic glasses, which were glued on top and bottom and fastened with blu tack stoppers of the same thickness. The schematic representations of a brain sample between glasses are shown on the right side of Figure 2.2 (b) and the left side of Figure 2.2 (c) by pink spots (samples) in blue rectangles (microscopic glasses).

Since placing two glasses in front of the spectrophotometer beam can lead to a Fabry-Perot cavity, the conditions for the effect occurrence and its influence on the measurement results were reviewed.

According to the criteria for the appearance of constructive interference between parallel planes, a standing wave pattern can be formed by only specific wavelengths that satisfy the condition $\lambda = {}^{2L}/_{k}$, where L is the distance between parallel planes and k is the integer number [49]. For the measuring brain samples, the distance L equals 1 mm, while for skin samples, the distance L is 0.5 mm. Therefore, constructive interference can only occur at wavelengths 320, 400, 500, 640, 800, 1000, 1250, 1600 and 2000 nm for spectrophotometric measurements from 300 to 2000 nm with 2 nm step. That means that only in 9 of 851 experimental points, the effect can appear and affect the measurements. The resonator does not perceive other wavelengths that do not meet this criterion.

Moreover, the Fabry-Perot effect appears only when a constant optical path length is maintained between reflective surfaces. However, due to the heterogeneity of the thickness of measuring biological samples, the glasses cannot be placed perfectly parallel to each other. Secondly, tissue refractive index changes can result in different optical path lengths for other sample regions, preventing the coherent superposition required for the Fabry-Perot effect. Thirdly, the microscopic glasses may have surface roughness and imperfections that can disrupt the continuity required for the interference effect.

Therefore, the Fabry-Perot effect can be neglected for the spectrophotometer measurements of mouse brain slices and skin samples located between microscopic glasses. It is attributed to the inherent complexities and optical characteristics of biological samples that contribute to disrupting the conditions required for the Fabry-Perot cavity. The unique properties of tissues, such as absorption, scattering, and surface irregularities, prevent possible distributions of the transmittance and diffuse reflectance measurements using glasses for holding mouse head tissues.

2.3 Theoretical and Experimental Results

The interaction of light with the mouse skin, skull and brain has been studied using spectrophotometer and femtosecond pulsed laser setup that described in the following Subsections 2.3.1-2.3.4.

The transmission and diffuse reflection spectra were measured by spectrophotometry technique (Subsection 2.3.1). The calculated radiation transfer coefficients were used to estimate the penetration depth for continuous-wave light (Subsection 2.3.2.1) and simulate the fluence rate distribution of the ultrashort pulses in biological tissues using the Monte Carlo Method in COMSOL Multiphysics Software (Subsection 2.3.2.2). Theoretical results were confirmed by experimental studies of the transmission of pulsed light through the mouse head tissues (Subsection 2.3.4).

2.3.1 Spectrophotometry

The transmittance and diffuse reflectance spectra of mouse skin (0.5 mm), skull (0.5 mm), and brain slices (1 mm) were measured using a spectrophotometer with a wavelength range of 350-2000 nm and 2 nm step. Figure 2.3 demonstrates (a) total transmittance and (b) diffuse reflectance spectra for mouse head samples. The total transmittance is the amount of light that passes through a medium, including unscattered light.

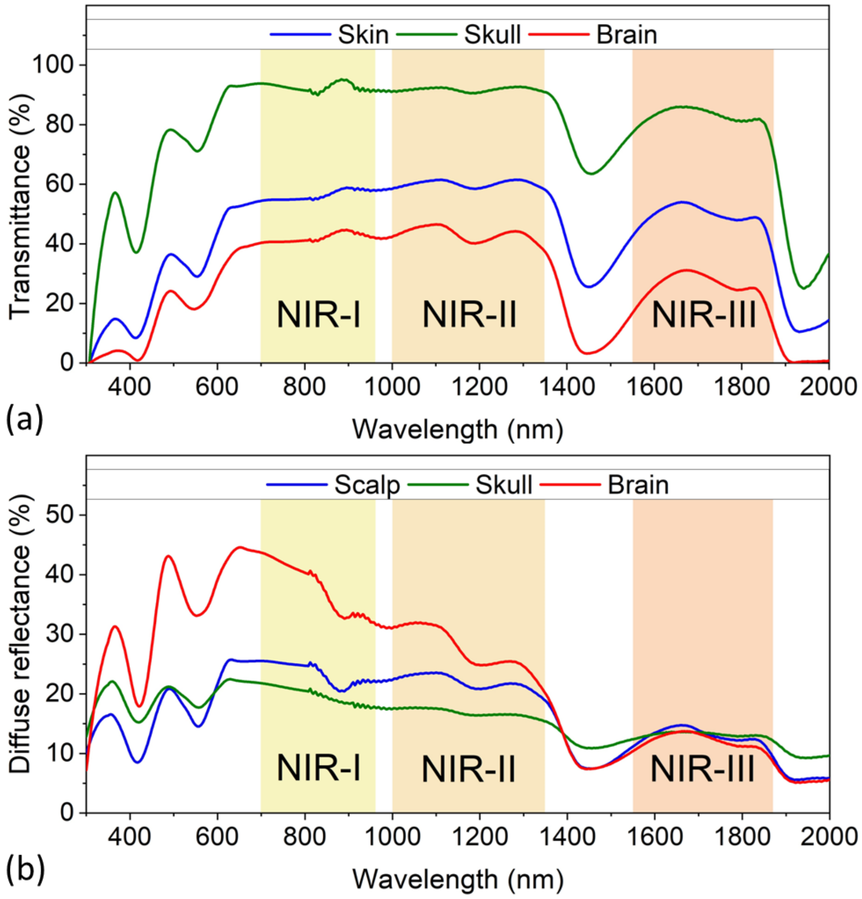

Figure 2.3. (a) Transmittance and (b) diffuse reflectance spectra of mouse skin (0.5 mm), skull (0.5 mm), and brain slices (1 mm) measured with a spectrophotometer.

Figure 2.3 also includes three near-infrared tissue transparency windows: (I) 700-950 nm; (II) 1000-1350 nm; (III) 1550-1870 nm separated by blood and water absorption peaks. Oxy- and deoxyhaemoglobin have high absorbance at wavelengths of ~420 nm and ~550 nm [50], while water molecules significantly absorb light at wavelengths of ~970 nm, ~1450 nm, and ~1950 nm [51].

The highest transmission is observed in samples of skull bones. In the first tissue transparency window, the transmittance reaches 95%. The second and third windows are characterised by a lower transmission level of 93% and 86%, respectively. The porous structure of the bones and the specific chemical composition influence light propagation through the skull. The main components that absorb light are HbO_2 (540 nm and 575 nm), collagen (1200 nm), and H_2O (1450 nm).

The maximum transmittance for skin is 62% (1110 nm). All three NIR windows have similar transmittance levels of about 55% with a slight fluctuation in NIR-III (48%). For skin, the main transmittance troughs in spectra are associated with haemoglobin (550 nm), collagen

(1200 nm), water (1200 nm, 1500 nm, and 1950 nm), and lipids (1500-1700 nm). In addition, fat scattering also prevents the penetration of light into the skin tissues (Fig. 2.3 (b), blue).

Light penetrates brain samples worse than other samples due to a large number of blood vessels and capillaries. The maximum transmittance values for biological windows are 45% (NIR-I), 47% (NIR-II), and 31% (NIR-III). There is high light absorbance by deoxyhaemoglobin (550 nm), water (1200 nm and 1500 nm), lipids (1700-2000 nm), and other proteins (1500-1700 nm) (Fig. 2.3(a), red).

As can be seen from the transmission and diffuse reflectance spectra, visible light penetrates biological tissues worse than near-infrared light due to the high reflection coefficient in the brain and strong absorption by blood. These results highlight the benefits of using light sources operating within NIR windows, which improve light penetration through biological tissues.

2.3.2 Calculation of Penetration Depth

The estimation of the penetration depth of continuous-wave light and ultrashort pulses within biological tissues is possible through the application of transport coefficients derived from the analysis of experimental spectra of mouse head tissues.

2.3.2.1 Continuous-Wave Light Propagation

Computer simulation of CW light propagation through biological tissues was performed using the inverse adding-doubling (IAD) method coupled with the Monte-Carlo model.

In biomedical optics and photonics, the inverse adding-doubling method is a computer approach used to calculate the optical characteristics of biological tissues, such as the absorption and scattering coefficients [52]. In contrast to the "forward" adding-doubling approach, which simulates the propagation of light through a known media, the "inverse" adding-doubling method works backwards from the measured light to determine the optical characteristics of the medium. The main advantages include high accuracy and the requirement of only integrations over angle.

In tissue optics, the IAD method is commonly used to determine tissue's absorption, scattering coefficients and scattering anisotropy factor by measuring unscattered transmission, total transmission, and diffuse reflectance of tissues [53]. However, measurements of light that does not scatter passing through thin samples, such as mouse skin, skull, and brain slices, are challenging to perform. Therefore, the transmittance T_t and diffuse reflectance R_d can provide information about the reduced albedo a' and reduced optical thickness τ'. In that case, the scattering anisotropy factor g remains constant value, while the reduced scattering factor g' would be equal to zero. During the calculations, the scattering factor was set to 0.9 as it is the most observed value for biological tissues at visible and near-infrared spectral wavelengths [1].

The reduced albedo can be calculated with the use of Eq. (2.1) [53]:

$$a' = \begin{cases} 1 - \left(\frac{1 - 4R_d - T_t}{1 - T_t}\right)^2 & \text{if } \frac{R_d}{1 - T_t} < 0.1 \\ 1 - \frac{4}{9}\left(\frac{1 - R_d - T_t}{1 - T_t}\right)^2 & \text{if } \frac{R_d}{1 - T_t} \geq 0.1. \end{cases} \quad (2.1)$$

The reduced optical thickness can be found by the formula shown in Eq. (2.2):

$$\tau' = \begin{cases} \frac{-\ln T_t \ln(0.05)}{\ln R_d} & \text{if } R_d \leq 0.1 \\ 2^{1+5(R_d+T_t)} & \text{if } R_d > 0.1. \end{cases} \quad (2.2)$$

According to the definition, the reduced optical properties can be represented by Eq. (2.3), where dimensionless albedo a and optical thickness τ are (Eq. (2.4))

$$a' = \frac{a(1-g)}{1-ag}, \qquad \tau' = (1 - ag)\tau, \quad (2.3)$$

$$a = \frac{\mu_s}{\mu_s + \mu_a}, \qquad \tau = d(\mu_s + \mu_a), \quad (2.4)$$

where d is the thickness of sample.

Therefore, we can estimate absorption μ_a and reduced scattering μ'_s coefficients with Eq. (2.5) and Eqs. (2.1-2.2), where $\mu'_s = \mu_s(1-g)$:

$$a' = \frac{\mu'_s}{\mu'_s + \mu_a}, \qquad \tau' = d(\mu'_s + \mu_a). \quad (2.5)$$

Since a spectrophotometer with an integrating sphere did not collect all light loss at the boundaries of samples, the Monte Carlo model was performed to make corrections of optical properties until the changes of calculated scattering and absorption coefficient values were less than 10 μm^{-1} between interactions. The accuracy of calculated parameters was controlled by the Nelder-Mead method [54]:

$$\frac{\left|R_d^{exp} - R_d^{calc}\right|}{R_d^{exp}} + \frac{\left|T_t^{exp} - T_t^{calc}\right|}{T_t^{exp}} < 0.0001, \quad (2.6)$$

where R_d^{exp} and R_d^{calc} are experimental and calculated diffuse reflectance, and T_t^{exp} and T_t^{calc} are experimental and calculated total transmittance.

The absorption coefficient is the length that a photon travels before it is absorbed by a biological tissue (Fig. 2.4 (a)), and the reduced scattering coefficient is a parameter describing the diffusion of a photon with a random step of $1/\mu'_s$ in a turbid medium. The relation between the light wavelength and the reduced scattering coefficient for skin, skull, and brain tissues is presented in Figure 2.4 (b).

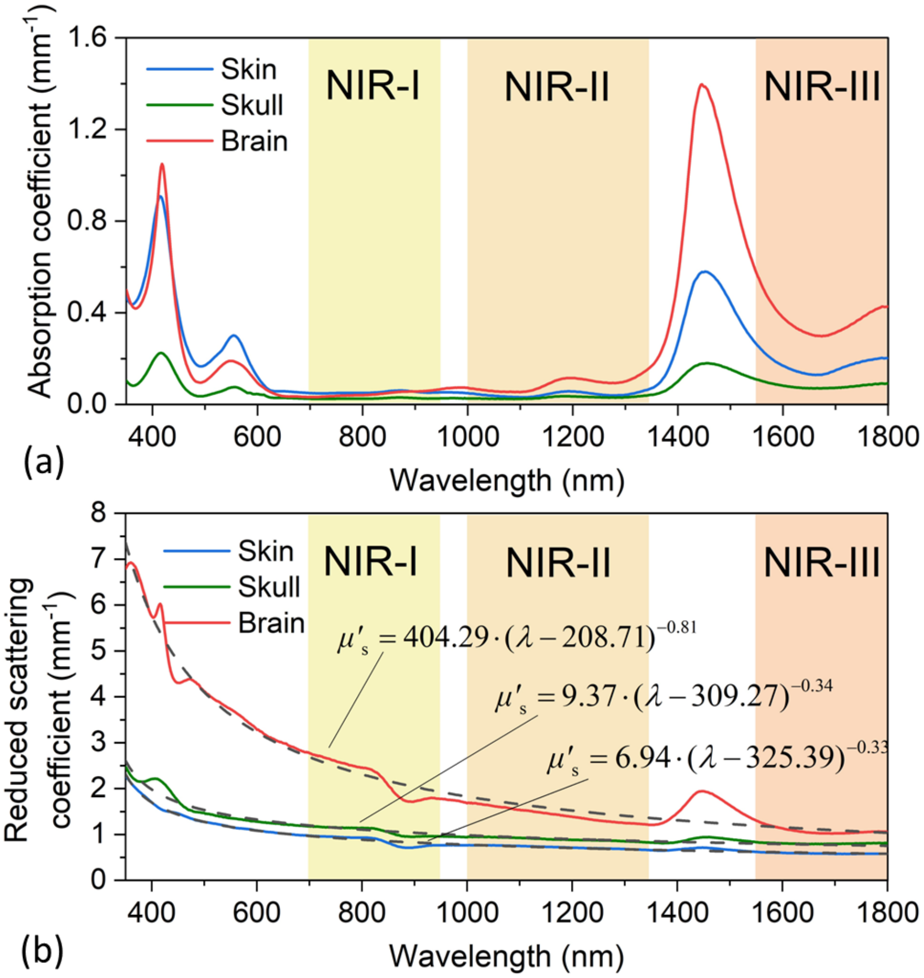

Figure 2.4. (a) Absorption and (b) reduced scattering coefficients for mouse head tissues.

The absorption coefficient peaks are associated with the absorption of blood (370-480 nm, 490-630 nm) and water (1100-1270 nm, 1300-1670 nm). The NIR windows located between them are highlighted by yellow, peach, and orange colours in Figure 2.4.

The penetration depth of mouse skin, skull, and brain samples was estimated using the absorption and reduced scattering coefficients. This parameter describes a length at which the radiation's internal intensity is reduced to 1/e of its surface-level value. The Eq. (2.7) was used to determine the penetration depth for different samples:

$$\delta = \frac{1}{\sqrt{3\mu_a(\mu_a + \mu'_s)}} . \qquad (2.7)$$

The penetration depth of CW light into mouse head tissues is demonstrated in Figure 2.5. The calculated parameter δ reaches the values of 2.8 mm, 3.6 mm, and 1.9 mm in NIR-I, 3.7 mm, 3.8 mm, and 1.9 mm in NIR-II, and 1.9 mm, 2.3 mm, and 0.9 mm in NIR-III for skin, skull, and brain, respectively. The maximum light penetration for all samples is in the first (750-830 nm) and second (1080-1190 nm) near-infrared transparency windows. These regions with the deepest tissue penetration were chosen to simulate a fluence rate distribution of ultrashort pulses.

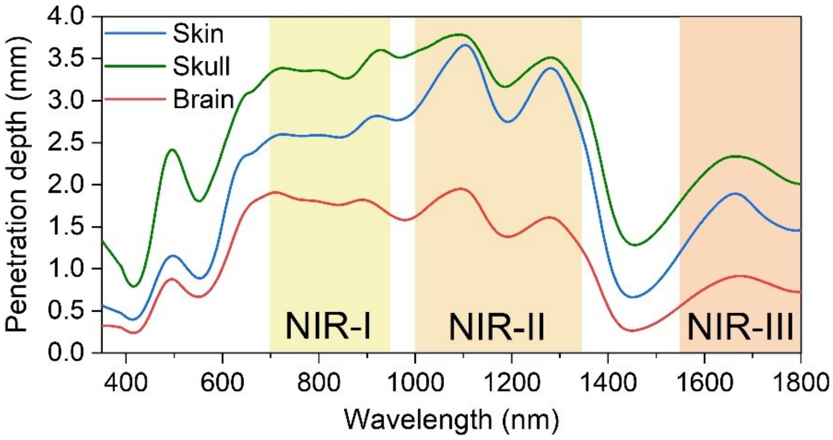

Figure 2.5. Penetration depth of continuous-wave light into mouse head tissues.

2.3.2.2 Ultrashort Pulse Propagation

The fluence rate distribution of ultrashort pulses into mouse head tissues was simulated by solving the radiative transfer equation with diffusion approximation. This approximation is well suited to highly scattered media such as biological tissues. COMSOL Multiphysics Software Environment was used to perform the simulation, where the sample geometry was divided into finite elements. The Helmholtz representation of the diffusion equation is shown in Eq. 2.8 [55]:

$$-\nabla(D\nabla\Phi) + \mu_a\Phi = S\,, \qquad (2.8)$$

where Φ is the fluence rate, *S* is the isotropic light source function depending on position vector and time, and *D* is the diffusion coefficient represented in Eq. 2.9.

$$D = \frac{1}{3(\mu_a + \mu'_s)}\,. \qquad (2.9)$$

A mouse head model with a three-layer system was used to evaluate the fluence rate. The thickness of each layer of skin and skull was set to 0.5 mm based on experimentally measured samples.

The sample optical properties were described by the determined absorption and reduced scattering coefficients for each layer. The simulation was performed in the NIR-I (750-830 nm) and NIR-II (1080-1190 nm) regions, which are characterised by the most significant penetration depth for all three layers (Fig. 2.5).

The selection of ultrashort pulse laser parameters was based on the characteristics of Ti:Sa laser setup that was developed for the experimental measurements of light-tissue interactions. The average power level of this laser system is 20 mW, laser irradiance values are 3.18 W/m² and 2.41 W/m², and beam diameters are measured as 200 μm and 230 μm for the NIR-I and NIR-II wavelength ranges, respectively. The laser system for experimental study will be separately discussed in Subsection 2.3.3.

Figure 2.6 shows how the irradiance of ultrashort pulses decreases depending on the depth of the three-layer mouse head model. When 780 nm (NIR-I) light passes through a 0.5 mm skin sample, 28% of initial irradiation transmits the tissue. In the case of 1190 nm (NIR-II), the transmittance value is higher and reaches 34%.

However, for the two-layer system, including 0.5 mm skin and 0.5 mm skull bone, only 9% of the initial level of 780 nm irradiance is retained, whereas 12% of 1190 nm light effectively reaches the brain cortex, as shown in Figure 2.6 (b).

At a depth of 1.5 mm, including three layers (0.5 mm skin, 0.5 mm skull, and 0.5 mm brain), there are a 6% initial irradiance of 780 nm light and a 9% light retention at a wavelength of 1190 nm.

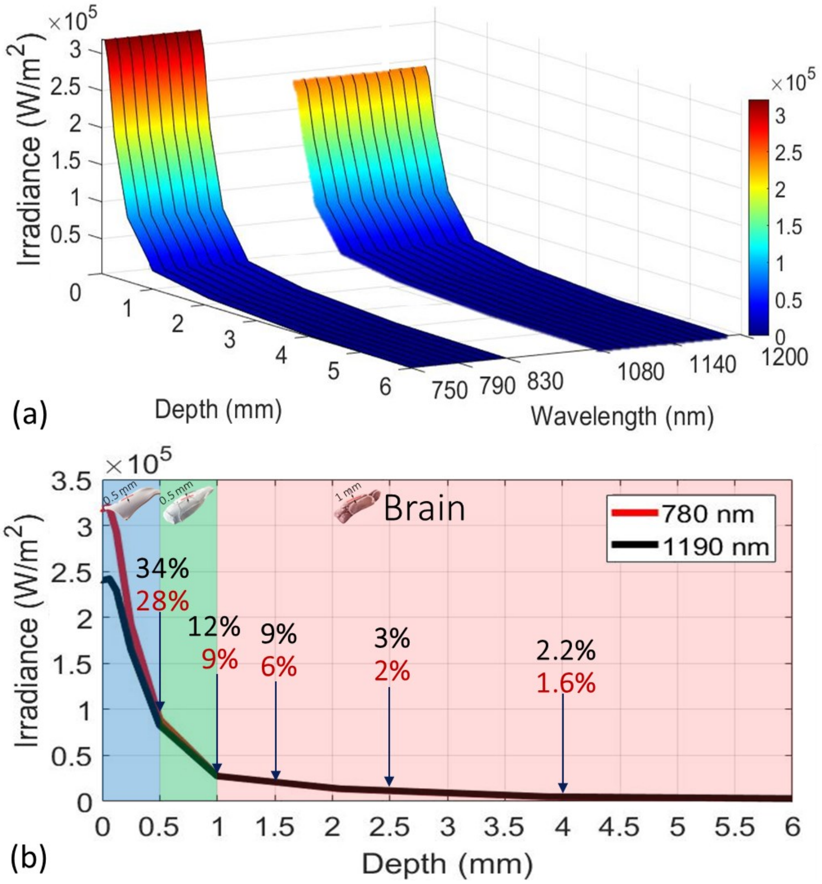

Figure 2.6. Fluence rate distribution of ultrashort pulses in mouse head tissues: (a) depending on the wavelength; (b) depending on the penetration depth for wavelengths of 780 nm and 1190 nm.

For the visual representation of ultrashort pulsed light attenuation in mouse head tissues, the visual demonstration was performed in COMSOL Software. Figure 2.7. demonstrates the fluence rate of ultrashort pulses in a mouse head model for a wavelength of 1190 nm. The modelled propagation of ultrashort pulses through only the brain is shown in Figure 2.7 (a), while the light penetration through the skin, skull, and brain tissues is demonstrated in Figure 2.7 (b).

The simulation confirms that sufficient laser irradiance (0.4 W/m^2) reaches the brain tissue passing through mouse skin and skull bone (Fig. 2.7 (b)). These results prove that the ultrashort pulse lasers operating in the near-infrared range efficiently deliver high power to the brain cortex through the skin and skull without overheating and damage. The computer simulation results were confirmed by the experiments on the laser light transmittance through fresh post-mortem mouse head tissues (Subsection 2.3.4).

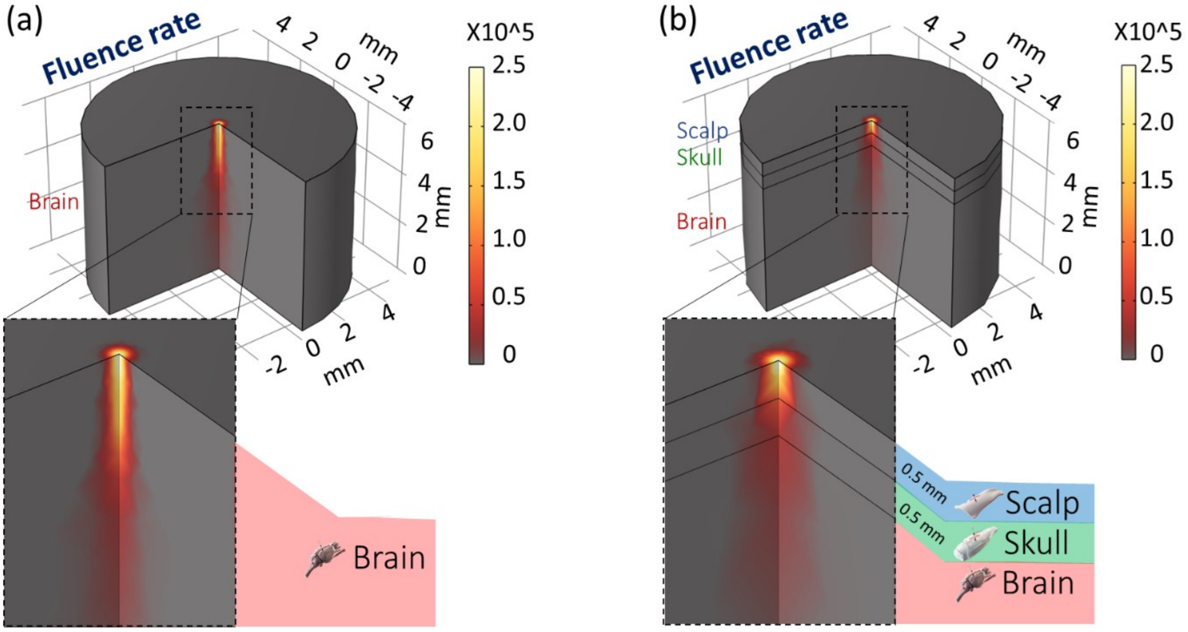

Figure 2.7. Ultrashort pulse fluence rate distribution into (a) mouse brain; (b) 0.5 mm thick skin, 0.5 mm thick skull, and brain for a wavelength of 1190 nm.

For simplicity, the demonstrated computer model was based on the assumption that the studied biological samples are isotropic. However, the skin, skull and brain are complex structures consisting of various elements, cells, and tissues with different optical properties. To gain a deeper understanding of the structure or pathology of a sample, a more detailed exploration of the scattering anisotropy in biological tissues is essential.

For example, M. Borovkova *et al.* [56] investigated the non-invasive detection of Alzheimer's disease using Mueller imaging polarimetry to identify amyloid-beta plaques, crucial pathological markers. The study revealed that structural changes primarily occurring in the grey matter and hippocampi can be detected by analysing the polarimetric properties of the brain. The presence of Aβ plaques with parallel alignment fibrils is associated with higher anisotropy of scattering in brain tissue and increased inhomogeneity of refractive index. This information provides valuable insights into the structural changes associated with Alzheimer's disease, demonstrating the potential of polarimetry for non-invasive detection and characterisation of pathological features in complex biological tissues.

2.3.3 Development of Laser System for Light-Tissue Interaction Study

The spectrophotometry method provided information about the interaction of continuous-wave light with biological samples. The absorption and reduced scattering coefficients extracted from the spectroscopic studies were used for the computer simulation of pulsed light propagation through mouse head tissues. However, experimental research is essential to ensure the correctness of the modelling method and to compare mouse head tissue interaction with continuous-wave light and ultrashort pulses.

The primary criteria for a laser setup applicable to a comprehensive study of how ultrashort pulses and CW light propagate through head tissues involve operating within the first and second biological windows and ensuring uniform parameters for both ultrashort pulsed and continuous-wave laser modes.

The laser system includes three main blocks operating in the first and second near-infrared regions: a 750-830 nm pulsed laser and 1086-1183 nm CW and pulsed lasers (Fig. 2.8). Block 1 consists of a tunable Ti:Sa laser (Sprite XT, M Squared) operating in 750-830 nm for measuring tissue transmittance in the first biological window. The pulse width of 130 fs and the repetition rate of 78 MHz are stable over the NIR-I region. The laser light is attenuated by a neutral-density (ND) filter until 20 mW average power. The beam is collimated by a system of optical lenses and has a diameter of 200 μm. Simultaneous monitoring and control of the incident and transmitted light are facilitated by splitting the beam using a plane parallel plate and utilising both a S121C Thorlabs photodiode power sensor and a S145C Thorlabs integrating sphere photodiode sensor shown schematically in Figure 2.8 in the blue area.

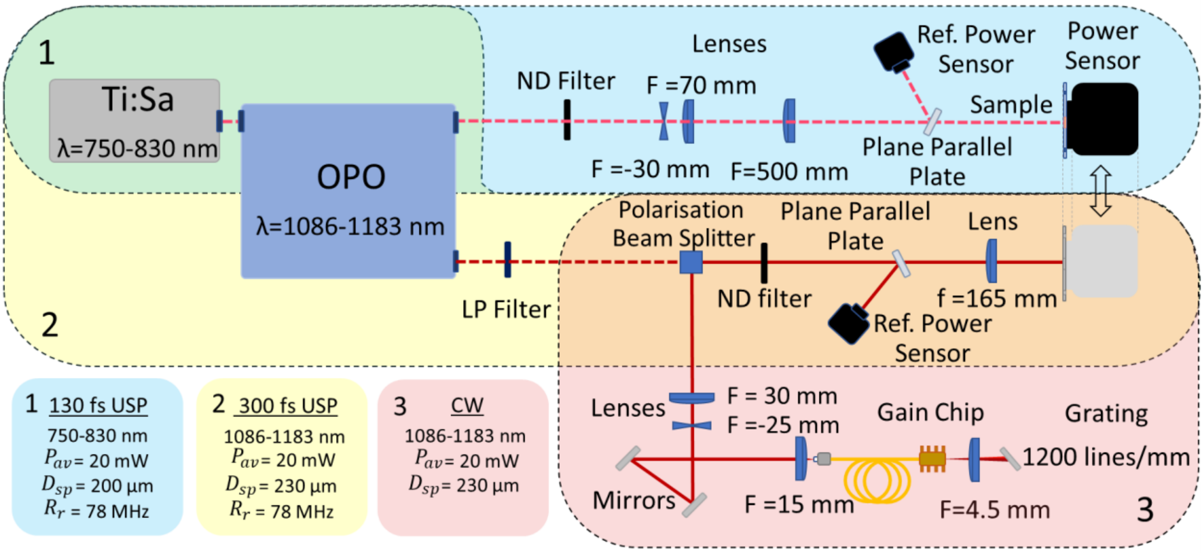

Figure 2.8. Schematic diagram of the developed experimental setup to measure transmission spectra of biological tissues in the first and second near-infrared ranges: (Block 1) 130 fs pulsed laser operating at a wavelength range of 750-830 nm; (Block 2) 300 fs pulsed laser with a wavelength range of 1086-1183 nm; (Block 3) CW laser tunable in the wavelength of 1086-1183 nm.

The integrating sphere photodiode sensor can be used for the transmission measurements of biological tissues that tightly cover the sensor window. Figure 2.9 (a) shows the integrating sphere with a brain sample fixed between microscopic glasses. As it was discussed before (Subsection 2.2.2), the effect of the plane-parallel Fabry-Perot cavity between two glasses can be neglected because the distance between glasses is 0.5 mm (skin sample) or 1 mm (brain slice), and only a wavelength of 800 nm can have a standing wave pattern between the glasses. Other wavelengths of 750-830 nm and 1086-1183 nm regions have reflected waves that interfere destructively because their phase difference is not equal to even integer multiples of π radians [49].

However, even at a wavelength of 800 nm, the probability of a Fabry-Perot cavity effect occurring is low since biological samples are characterized by inhomogeneous structures with different reflectance indices and tissue thicknesses, which can lead to the non-parallel arrangement of microscopic glasses and different optical path lengths for various areas of the sample, which prevents coherent superposition required for the Fabry-Perot effect. Therefore, placing the sample between the glasses should not affect the experimental results of light transmission measurements. The schematic representation of the direction of transmitted light inside the integrating sphere photodiode power sensor is illustrated in Figure 2.9 (b).

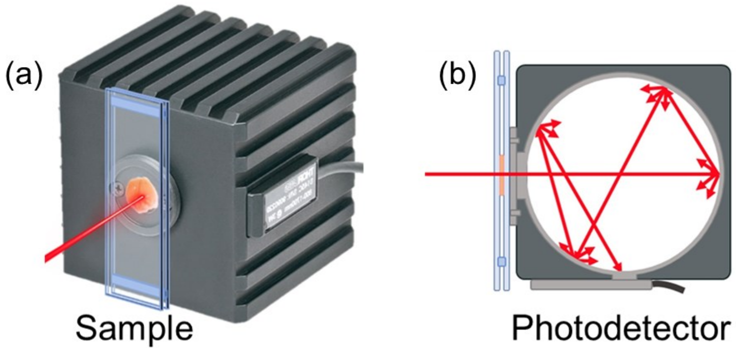

Figure 2.9. (a) Brain sample fixed between glasses; (b) schematic view of transmitted light distribution inside the integrating sphere photodiode power sensor.

The integrating sphere photodiode sensor and the sample can be moved from Block 1 to Block 2 to measure transmittance in the second biological window. A blue rectangle and a black box on the right side of Block 1 (Fig. 2.8) is a schematic representation of the sample and detector, respectively. Moving the detector system with the glued sample between Blocks is possible by saving the position of the target sample point for the corresponding repetition of the measurement conditions in the first and second biological windows. The small black arrow between Block 1 and Block 2 (upper right part in Fig. 2.8) shows the possible horizontal movement of the integrating sphere and sample between Blocks.

Block 2 comprises a Ti:Sa laser emitting light within the 750-830 nm wavelength range. However, in contrast to Block 1, this light passes through an optical parametric oscillator (OPO) and is transformed into 300 fs pulses within the 1086-1183 nm range (Fig. 2.8, yellow area). The ND filter attenuates the average power to 20 mW. The lens (f=165 mm) focuses the laser beam onto the sample with a spot diameter of 230 µm.

Block 3 has been designed to compare how tissues interact with pulsed and continuous-wave laser modes. The main light source used in this block is the Innolume gain-modules CW fibre laser with a central wavelength of 1140 nm. The grating can tune the light between 1086 nm and 1183 nm wavelengths. The 1200 lines/mm grating is located on the rotation stage, the changing angle of which allows the gradual shift of an operating wavelength of the laser. This block is visually highlighted in Figure 2.8 in red colour.

A fundamental principle of laser system design is ensuring identical beam direction and diameter for both pulsed and continuous-wave lasers operating in NIR-II (Blocks 2 and 3). The beams are co-directed using a polarising beam splitter cube, focused on the sample, and detected by integrating sphere photodiode sensor moved from Block 1 to Block 2 (black rectangle and grey box in the right part of Block 2, Fig. 2.8). The adjustment process of collimating two beams was monitored using a digital beam profiling camera (UCD12, WinCamD).

The developed experimental setup enables the measurement of tissue transmittance using continuous-wave and ultrashort pulse lasers that operate in the first and second near-infrared regions.

2.3.4 Transmission Measurements with CW and Ultrashort Pulsed Lasers

The study includes a comparison of how continuous-wave and ultrashort pulsed light penetrate post-mortem mouse head samples and light transmission measurements of one-, two-, and three-layer samples in NIR-I and NIR-II.

A developed laser source was used to compare the penetration of continuous-wave and pulsed light into 0.5 mm skin, 0.5 mm skull bone, and 1 mm brain slices. The incident beams were carefully adjusted to ensure equal parameters between the two laser modes, operating within the 1086-1183 nm wavelength spectrum (Fig. 2.8).

The tissue temperature was controlled during the experiments and did not increase more than 2 ºC. Each measurement was repeated three times in different parts of the freshly prepared tissues.

Figure 2.10 shows the transmittance spectra of post-mortem mouse head tissues in the second near-infrared window. The solid line represents the CW light transmission results, while the dotted line depicts the transmittance of mouse head tissues irradiated with a pulsed laser.

In experiments of skin tissues, evaluation of the penetration efficiency between continuous and pulsed light sources gave uncertain results. The skin transmission of the CW light demonstrates a relatively constant value of 45% (Fig. 2.10, blue solid line). For the pulsed light, the transmission values fluctuate between 42% and 48% depending on the wavelength (Fig. 2.10, blue dashed line). The demonstration of similar transmission efficiency in the skin for both laser modes is due to the small sample thickness, which leads to reduced transmission length and infrequency of scattering events. However, it is worth noting that the error bar associated with continuous-wave laser transmittance overlaps with the transmitted power values of the pulsed laser, making it inconclusive to determine whether CW irradiation leads to higher tissue transmission values.

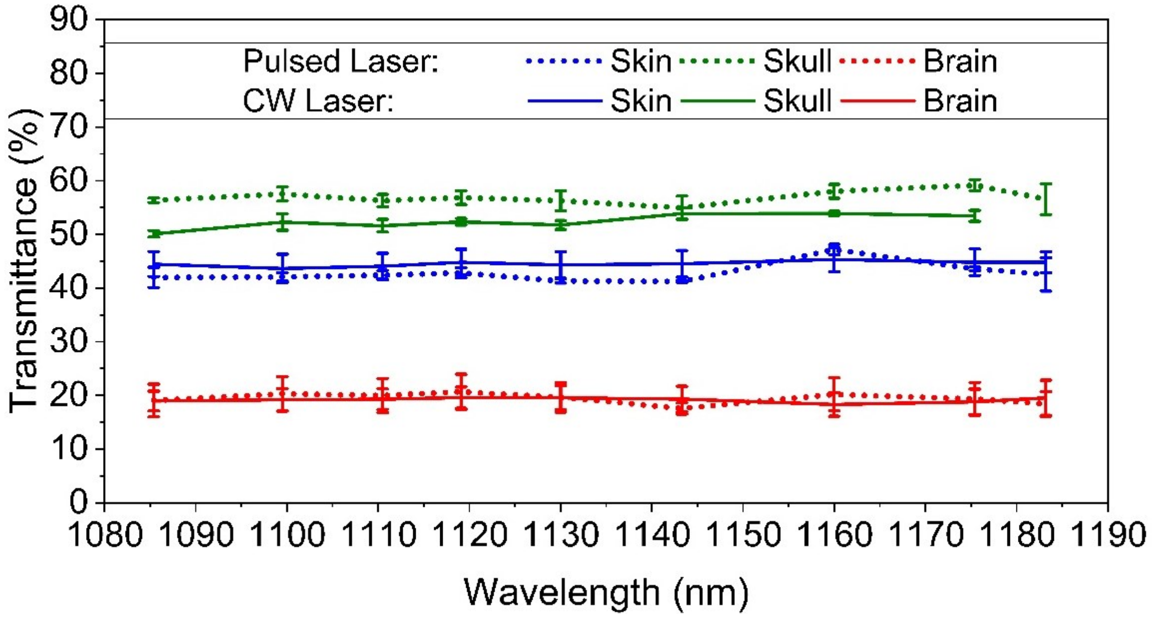

Figure 2.10. Transmittance of post-mortem mouse head samples (0.5 mm thick skin, 0.5 mm thick skull, and 1 mm thick brain) irradiated by continuous-wave and ultrashort pulse lasers.

In the brain tissue measurements (Fig. 2.10, red lines), both laser modes demonstrate similar transmission levels. There are only a few percentage differences between pulsed (20.5%) and CW (19%) light irradiations passed through a 1 mm brain sample.

However, in skull bone samples, pulsed light exhibits significantly higher transmission than continuous-wave light. The gap between CW and pulsed light transmittance is visible in Figure 2.10 (green solid and dashed lines, respectively). The maximum transmittance value of 59% is observed for ultrashort pulses, while the transmittance of CW light in the skull varies from 50% to 54%.

The results demonstrate that ultrashort pulses penetrate deeper into biological tissues than continuous-wave light in skull bone because the high photon density and short pulses create an instantaneous transparent area for photons to pass through and cause less tissue interaction. However, this difference is insignificant for studied samples of skin and brain. Since all samples are relatively thin, the absorption and scattering coefficients (Fig. 2.4) obtained from spectrophotometric measurements can be used for modulation of pulse generation in narrow layers of tissues with quite high accuracy (Fig. 2.6).

To estimate the impact of the intricate curvatures in the different layers of head tissues and complex bends between them on photon migration, additional measurements of pulsed light transmittance of freshly prepared mouse head tissues consisting of two and three layers were performed. For this purpose, a developed laser system operated in the mode of ultrashort pulses in the first (750-830 nm) and second (1086-1183 nm) near-infrared windows.

A freshly prepared two-layer head sample was 1 mm thick and included undivided skin and skull tissues. A 2.5 mm thick three-layer system consisted of unseparated layers of skin (0.5 mm), skull bone (0.5 mm), and brain slice (1.5 mm). The thickness of layers was determined only after completing optical experiments.

Figure 2.11 shows the transmittance of single-, two-, and three-layer mouse head tissues with the use of the femtosecond pulsed lasers operating in the NIR-I and NIR-II ranges.

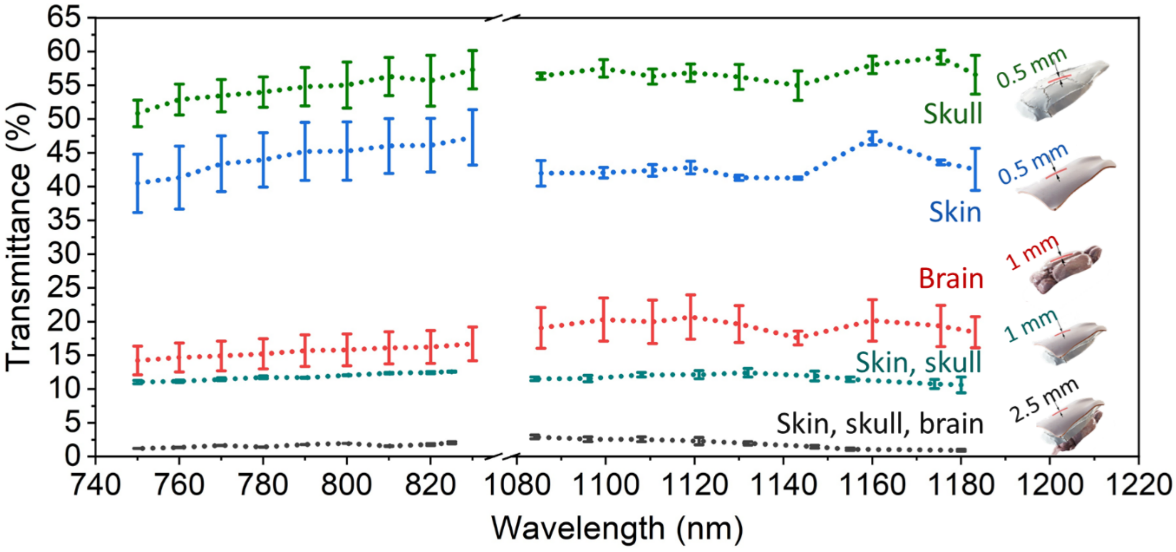

Figure 2.11. Transmittance of post-mortem one-, two-, and three-layers of mouse head samples irradiated by ultrashort pulse lasers.

Experimental results demonstrate that the skull bone (green line) has the highest transmittance compared to other samples. Transmission of laser light through skull bone varies from 50% to 57% in the NIR-I region and from 55% to 59% in the NIR-II window. Skin tissue (blue line) is characterised by a lower transmittance level of 41-47%. Both samples have a gradual increase of transmittance in the wavelength range of 770-830 nm, which is higher than in the NIR-II region (1080-1180 nm). This behaviour is due to light absorption by water components, which are present in large quantities in fresh skin and skull bone samples.

A similar approach is noted in the two-layer sample of skin and skull. In both near-infrared windows, 10-12% of the initial irradiation of ultrashort pulse laser passes through the two-layer system in near-infrared windows.

The one- and three-layer systems that include brain slices are characterised by reversed behaviour regarding the comparison of transmittance in NIR-I and NIR-II. Since brain tissues contains many blood vessels and capillaries, and blood absorbs light significantly at wavelengths up to 1 μm, the transmittance values in NIR-I are slightly lower than in NIR-II. Light transmission through one layer of the 1 mm thick brain varies from 14% to 21%. In comparison, the results of three-layer sample measurements show transmittance values in the range of 2-3% with a maximum at a wavelength of 1080 nm.

In the first near-infrared window, all measured samples demonstrate a growth in transmittance with increasing wavelength due to reduced blood absorption. On the contrary, in the NIR-II, the transmittance values decrease slightly in the wavelength range of 1160–1180 nm because the influence of water absorption begins at those wavelengths.

The computer simulation and experimental results of ultrashort pulses passing through two- and three-layer samples are consistent. This fact confirms the high accuracy of the simulation method. Both methods show that 10-12% of the initial ultrashort-pulse radiation reaches the upper layers of the brain cortex, passing through the skin and skull without overheating them.

The extent of overheating and skin damage can be assessed by measuring radiant exposure and dose. According to the experimental study of different research groups, the minimum visible skin lesion can be observed at the radiant exposure of 20-179 J/cm^2 [57]-[61]. The wide range of values is due to the significant dependence of lesion on wavelength, average power, laser mode, and exposure time. Table 2.1 shows the radiant exposure values for the minimum damage of various samples, such as human, porcine, and Yucatan miniature pig skins, experimentally found by multiple research groups [57]-[61].

Table 2.1. Values of radiant exposure for a minimum visible skin lesion.

Sample Type	Wavelength, nm	Power, W	Laser Mode	Beam Diameter, cm	Time, s	Radiant Exposure, J/cm^2
Human	1060	200	CW	1.05	1	20-80, Ref. [57]
Yucatan miniature pigs	1070	8.5	CW	1.9	10	112, Ref. [58]
Yucatan miniature pigs	1070	4.3	CW	1.1	10	179, Ref. [58]
Porcine	1314	0.2	Pulsed, 350 us	0.07	1	99-111, Ref. [59]
Yucatan miniature pigs	1319	1	CW	0.61	10	62, Ref. [60]
Porcine	1319	15.4	CW	0.98	1	40.8, Ref. [61]

The significant differences in outcomes prompt quantifying radiation exposure and dose for mouse skin lesions when the developed prototype laser irradiates samples. For these purposes, the average power of the Ti:Sa laser with OPO was increased to 50 mW. The parameters of the laser system for measuring skin damage are given in Table 2.2.

Minimum visible skin damage was observed only after almost three minutes of laser exposure (dose of 24062 J/cm^2), characterized by a gradual increase in light transmission through the post-mortem samples.

Table 2.2. Radiant exposure and dose for a minimum visible mouse skin lesion under 1080-1180 nm radiation of developed prototype laser.

Average Power, W	Pulse Duration, fs	Repetition Rate, MHz	Beam Diameter, cm	Energy Fluence, μJ/cm^2	Radiant Exposure, J/cm^2	Exposure Time, s	Dose, J/cm^2
0.05	300	78	0.03	1.8	141.5	170	24062

The light irradiation of the developed prototype laser system with an average power of 20 mW and beam diameter of 230 μm that was used in the transmittance measurements (Fig. 2.10-2.11), has an energy fluence of 1.2 μJ/cm^2 and a radiant exposure of 96.3 J/cm^2. The minimum visible skin lesion can appear only after 4 minutes of continuous laser irradiation in the same focused spot of the size of 1 pixel. However, modern optical imaging has a scanning speed of 1 pixel per few milliseconds or even femtoseconds [62], [63]. Therefore, this level of laser exposure is much lower than the tissue damage threshold, and the developed prototype laser can be safely used for *ex vivo* and *in vivo* experiments.

2.4 Conclusions

Light-tissue interactions for various mouse head tissues have been evaluated to develop laser systems for potential biomedical research applications, such as brain imaging and therapy. A comprehensive analysis of transmittance and diffuse reflectance spectral measurements was performed in a broad spectral range from 350 to 2000 nm, demonstrating three tissue transparency windows. The light-tissue interaction studies demonstrate the deepest penetration through head tissues in the first and second NIR windows.

The optical transport coefficients have been calculated for all examined head tissues, including skin, skull bone, and brain. These coefficients were subsequently used in computer simulations to model the propagation of continuous-wave and pulsed laser light within biological tissues. The theoretical calculations reveal that, for the 780 nm laser light, approximately 9% of initial irradiation penetrates through the skin and skull, while for the 1190 nm wavelength, about 12% of the incident ultrashort pulsed light reaches the brain cortex.

These findings are confirmed through experimental investigations of the light transmittance characteristics of head tissues, demonstrating the high accuracy of the simulation model. Furthermore, the experimental results illustrate the superior transmittance of ultrashort pulses compared to continuous-wave light, indicating potential higher efficiency in thicker tissue samples of other animals.

A prototype laser system operating within the first and second NIR regions has been demonstrated to explore the effectiveness of light propagation within mouse head tissues. This system holds promise for potential applications in a wide range of biomedical research areas, including optical imaging, blood flow monitoring, photodynamic therapy, and optogenetic studies.

Chapter 3

Optical Properties of Optogenetic Tools

[Pages 41-64 redacted from open access version including Figures 3.1, 3.2, 3.3, 3.4, 3.5, 3.6, 3.7, 3.8, 3.9, 3.10, 3.11, 3.12, 3.13, 3.14.]

Chapter 4

Laser System for Optogenetics

4.1 Motivation

Optogenetics allows the monitoring and controlling of neuronal activity using genetically engineered light-sensitive proteins expressed in neurons that can be modulated by light sources, enabling the stimulation or inhibition of neurotransmitters [75]. However, modern optogenetics approaches usually need the skull drilling and inserting an optical fibre into the brain tissues to transmit light to certain parts of the brain cortex [142]. Figure 4.1 demonstrates the stimulation of the neuronal activity in the mouse brain that leads to animal locomotion.

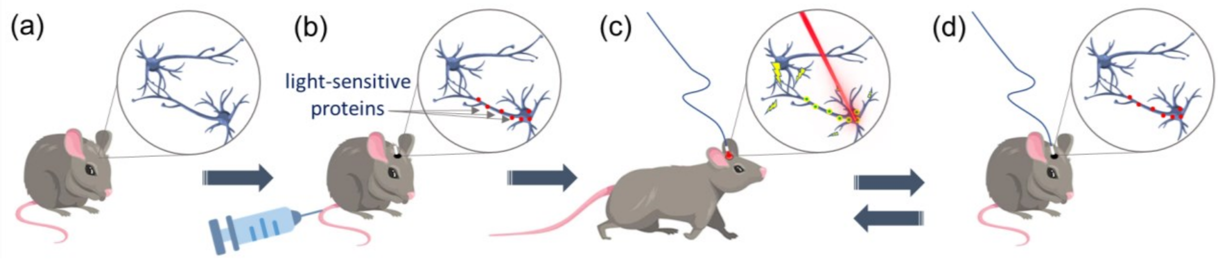

Figure 4.1. Schematic representation of optogenetic neurostimulation. (a) Mouse before optogenetic processing; (b) implementation of a cannula and injection of viral vectors or plasmids encoding photosensitive proteins; (c) activation of neurons with light delivered via optical fibre; (d) termination of neuronal stimulation.

The optogenetics process includes several stages, such as preparing the animal for the optogenetics procedure, including anaesthesia and insertion of a cannula into the brain cortex [143] (Fig. 4.1 (a)).

Depending on the type of disease, various genetic constructs express opsin/phytochromes and deliver them to specific types of neuronal cells. This step includes the modification of genetic constructs and introduction of viral vectors or plasmids into the animal body [144]. Usually, the genetically modified photosensitive proteins are expressed in neuronal cells through peripheral exposure (Fig. 4.1 (b)).

After three weeks, required for full expression of opsin/phytochromes within neuronal cells [145], neurostimulation experiments continue with the delivery of light to the cortex via cannula and optical fibres (Fig. 4.1 (c)) and stimulation or termination of neurons (Fig. 4.1 (d)). The interaction of photons with the photoactuators induces conformational changes through photoisomerisation, which result in the opening of channels or activation of pumps, influencing the membrane potential of the neuronal cells [146]. Stimulated neurons initiate communication with each other through neurotransmitters activating the functionality of specific brain areas. The process of activation and termination can be repeated several times depending on the type of photosensitive proteins.

Non-invasive optogenetics could be a breakthrough in the treatment of neurological diseases. This method that does not require invasive surgical intervention can prevent tissue damage and inflammation that exist in modern optogenetics.

One of the methods to realise the non-invasive optogenetics is using ultrashort pulse lasers with a high peak power operating in the second near-infrared window (1100-1350 nm). The light-tissue interaction study presented in Chapter 2, has shown that between 10% and 12% of ultrashort pulse radiation can be delivered to the mouse brain cortex by passing through the skin and skull (Fig. 2.11). Ultrashort pulses of this power should be enough to stimulate neurons without damaging the surrounding areas [26].

Moreover, the demonstration of two-photon conversion of phytochrome in Chapter 3 (Fig. 3.7) supports the potential use of light-sensitive proteins in optogenetics to treat various neurological diseases using near-infrared laser sources. Therefore, a possible non- or minimal invasive neurostimulation method involves using a NIR-II femtosecond laser and phytochrome as a light-sensitive protein expressed in neuronal cells (Fig. 4.2 (a)).

Phytochrome can be converted from the Pr to the Pfr state by linear light absorption in the wavelength range of 630-690 nm and two-photon absorption at 1180-1360 nm wavelength [26]. Passing through the skin and skull, 1180-1360 nm light of ultrashort pulsed laser excites the phytochrome molecules, causing large-scale conformational changes in the structure and switching the D-ring of biliverdin from *cis* to *trans* configuration due to two-photon absorption (Fig. 4.2 (b)). The Pfr phytochrome connected to the neuron helps positively charged ions enter the cell, which leads to signalling between neurons. Stimulation of neurons could be stopped by returning the phytochrome molecule to the Pr state (Fig. 4.2 (c)). This is possible when the phytochrome is illuminated with 740–780 nm light for a fraction of a minute [130]. As this light operates in the first near-infrared window (700-1000 nm), it can penetrate deeply through biological tissues.

Alternatively, the phytochrome could be converted to its original *cis* configuration by relaxation in the dark after 8-15 hours. These cycles of phytochrome photoconversion (Fig. 4.2 (a-c)) could be repeated hundreds of times [96].

The developed prototype of the laser designed for two-photon activation of phytochromes (Fig. 3.4) demonstrates remarkable results, making it a promising laser prototype for non-invasive optogenetics applications. The study of light-tissue interactions has revealed that sufficient light irradiance can penetrate the skin and skull and reach the brain cortex, where photoactuators can be expressed (Fig. 2.11).

However, the current laser setup, comprising a Ti:Sa laser combined with an OPA and complicated cooling system, has a relatively high price, bulky design, numerous free-space optical elements necessitating initial adjustments. Also, the system is sensitivity to humidity, temperature changes and fluctuation of other environmental conditions. These factors prevent the practical use of solid-state laser sources for potential biomedical and clinical applications outside photonics laboratories.

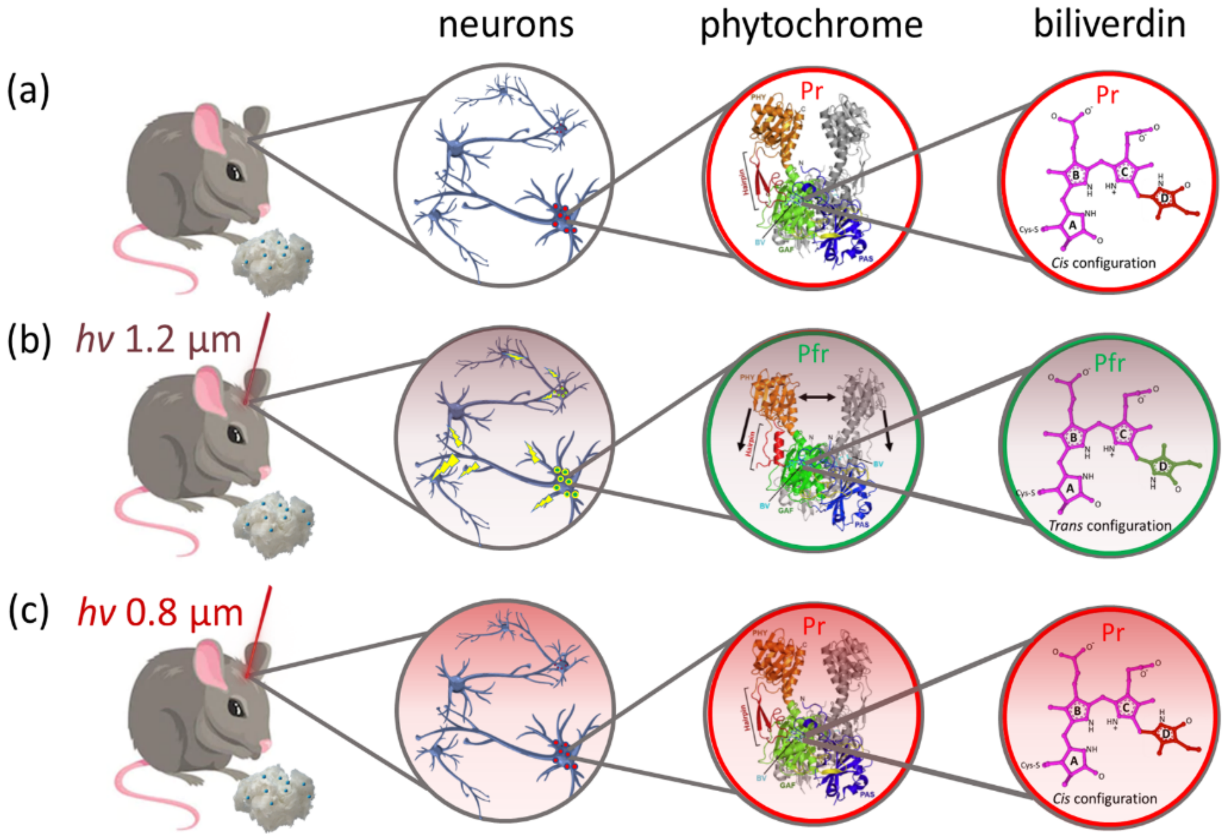

Figure 4.2. Schematic representation of phytochrome molecules expressed in neuronal cells and photoconversion mechanism: (a) in dark conditions, (b) under 1180-1360 nm, and (c) 750-820 nm light illumination.

For clinical applications, achieving non-invasive optogenetics demands compact, high-peak-power laser systems operating at a wavelength between 1180 nm and 1360 nm. Such systems should prioritise robustness, affordability relative to solid-state lasers, and long-term effectiveness and stability while offering a user-friendly interface. A brief overview of potential pulsed laser sources that meet these criteria is presented in the next section.

4.2. Review of NIR-II Pulsed Laser Sources

Laser sources operating within the NIR-II region are in great demand for applications in the field of biomedicine. Various laser types have been developed to produce pulses within this specific wavelength range.

As an illustration, semiconductor lasers utilising materials like GaAs and InAs have expanded their coverage to encompass the entire second tissue transparency window [11]. Nevertheless, apart from their cost-effectiveness and compactness, these lasers are characterised by their sensitivity to elevated temperatures, electrical noise, restricted output power, and a shortened operational lifespan attributable to material degradation. All these limitations result in significant drawbacks for potential clinical applications.

Other sources like gas [2] or chemical [147], [148] lasers are characterised by narrow wavelength tunability. In contrast to them, solid-state lasers can cover a wide range of operating wavelengths, especially when they are combined with optical parametric oscillators or amplifiers. However, crystal-based solid-state lasers such as Cr:forsterite [7], Nd: YAG [14], or Ti:Sa [8] are very complex and expensive systems, primarily due to the need for cooling systems and free-space optical components. These lasers are excellent tools for studying biological samples in photonics laboratories but may not be suitable for use in hospitals or clinical settings due to their bulkiness and cost. Figure 4.3 shows the laser sources operating at the second tissue transparency window [2], [7], [8], [11], [14], [149]-[153].

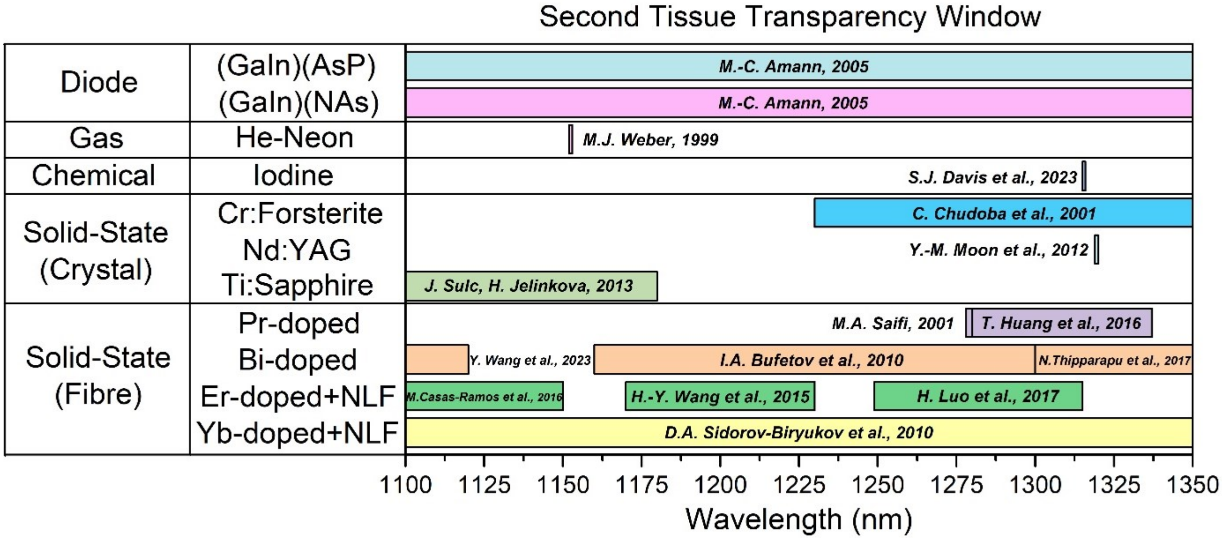

Figure 4.3. Review of pulsed laser sources, including fibre lasers with nonlinear fibres (NLFs), operating at second tissue transparency window.

Finally, another category of solid-state lasers which is based on optical fibres doped with rare ions instead of crystals as the gain medium, operates in NIR-II. Compared to crystal-based solid-state lasers, fibre lasers are much more economical, compact, and reliable since they do not include many free space components and consequently do not require additional alignment of the optical elements. However, their development is also challenging due to the lack of conventional rare earth-doped fibres for the wavelength range of 1100-1350 nm.

Fibre lasers and amplifiers have gained popularity, especially using Praseodymium, Bismuth, Erbium, or Ytterbium-doped fibres, as these systems generate pulses in NIR-II due to nonlinear phenomena in the optical fibres. This is possible through the integration of nonlinear elements that enable wavelength shifting from primary rare-earth element emission wavelengths to 1100-1350 nm (Fig. 4.3, Section Doped Fibre) [149]-[154].

In 1994, M.J. Guy *et al.* [155] demonstrated the first 1302 nm ultra-short pulse laser based on Pr-doped fibre (PDF). In their study, the PDF laser generated 620 fs pulses with an output power of about 4 mW. However, the laser was not all-fibre and required a lot of space since the PDF laser built with a figure-eight architecture was pumped by a laser source based on Ti:Sa laser.

Y. Song *et al.* [156] demonstrated a ring subpicosecond fibre laser operating at a wavelength of 1300 nm with a repetition rate of 3.18 MHz. They used a Pr-doped fibre as a gain medium and carbon nanotubes (CNTs) as a saturable absorber (SA). The disadvantage of their system is that CNT-saturable absorbers limit the maximum output power of lasers (1.67 mW) due to their low thermal threshold [157]. This poses a significant issue since optogenetic applications necessitate high-peak power to stimulate neurons by a two-photon absorption mechanism.

Another example is the multiwavelength Brillouin Praseodymium fibre laser [158], which combines Pr-doped fluoride and a Brillouin gain media. The laser emission is generated through stimulated Brillouin scattering (SBS). SBS is a nonlinear optical effect occurring in Kerr medium, such as single-mode fibres (SMFs) [159]. When an intense pulse propagates through this medium, the electric field itself can generate acoustic waves due to electrostriction, locally changing the refractive index as it propagates through the medium. The light interacts with these acoustic waves, causing a significant portion of its power to be reflected with an additional frequency shift (about 10 GHz in quartz fibres). H. Ahmad *et al.* [158] built a tunable laser source with a linewidth of 500 kHz and a power of 8 dBm as the Brillouin pump. When the double-spaced multiwavelength signal started to be generated, a laser ring cavity was disconnected by a micro-air gap, which attenuated Odd-Stokes due to Fresnel reflection, resulting in the generation of 36 Stokes lines in 0.16 nm increments at a central wavelength of 1300 nm.

However, the Brillouin Praseodymium fibre lasers are complex systems that require careful design and optimisation to achieve the necessary output parameters with a low repetition rate and high peak power.

Bi-doped fibre is used in lasers that operate at various luminescence windows, namely 1050-1120 nm, 1150-1270 nm, 1250-1310 nm, 1300-1350 nm, and 1500-1800 nm. The operating wavelength strongly depends on the rare earth element concentration and the type of silicate present in the fibre core [152], [160]. Aluminosilicate, germanosilicate, and phosphosilicate fibres are used for lasers operating in a wavelength range of 1100-1350 nm.

The example of a laser with a Bi-doped aluminosilicate fibre was demonstrated by I.A. Bufetov *et al.* [161]. Two Ytterbium-doped fibre lasers operating at wavelengths of 1058 nm and 1085 nm were used as pump sources. Fibre laser with 12 m long Bismuth-doped fibre (BDF) emitted an output power of 1 W at a wavelength of 1160 nm. They also demonstrated another continuous-wave laser based on Bismuth-doped germanophosphorosilicate fibre operating at a wavelength of 1318 nm [161]. In this work, the BDF laser was pumped by the 1230 nm co-propagating Raman, providing an output power of 10 W with an efficiency of 37%. The same doped fibre with a length of 39 m was used in a picosecond laser with a central wavelength of 1322 nm [162]. This pulsed laser was designed with a linear cavity, including a semiconductor saturable absorber mirror (SESAM) and a chirped fibre Bragg grating (FBG). The developed Bismuth-doped fibre laser (BDFL) generates 2.51 ps pulses with a repetition rate of 2.49 MHz and an average power of 0.3 mW.

In another all-fibre scheme, the mode-locked laser contained 25 m of a highly Bi-doped phosphosilicate fibre as a gain medium [163]. The laser built on a ring cavity configuration was pumped by a 1270 nm laser diode. At a pump power of 335 mW, the laser generates 3 ns pulses with a repetition rate of 6.3 MHz. The central wavelength was 1340 nm, while the maximum output power was about 3 mW. To increase the average power, the output was connected to an amplifier with 100 m of Bi-doped fibre. The maximum average power after amplification reached a value of 18 mW with a pulse duration of 2.5 ns.

Although Bismuth-doped fibres are a promising medium for fibre lasers and amplifiers, there are still several challenges associated with low Bismuth concentration and high losses in long fibres [152].

Er-doped fibres are commonly used in lasers operating at 1550 nm due to the high emission peak at this wavelength. However, it has also been shown that Erbium-doped fibre (EDF) can be used as a gain medium for lasers operating at a central wavelength of 1100-1300 nm if they are combined with highly nonlinear fibres (HNLFs).

In 2015, H.-Y. Wang *et al.* [164] developed an EDF ring cavity seed laser and an EDF amplifier with HNLF operating at a wavelength of 1190 nm. The all-fibre seed laser included two PCs, polarisation-dependent isolator (ISO), and a 0.75 m long EDF pumped by a 980 nm laser diode. This seed source generated 300 fs pulses with a repetition rate of 52 MHz, and an average power of 170 mW at a central wavelength of 1550 nm. This signal was amplified in a 1.4 m EDF, followed by a 2.1 m single mode fibre, and compressed in a 1 m dispersion compensating fibre (DCF). In the final stage, HNLF of about 20 cm allowed to shift the operating wavelength from 1550 nm to 1190 nm, resulting in 125 fs pulses with a peak power of 8.56 kW and an average power of 103 mW.

Another example of a 29 fs Erbium-doped fibre laser with HNLF operating at a wavelength of 1315 nm was demonstrated by H. Luo *et al.* [153]. The oscillator source was a ring cavity laser with a 1.4 m Er-doped fibre, a polarisation-dependent ISO, and PCs, ensuring a mode-locking mechanism through nonlinear polarization rotation. Then, 95% of output power was compressed into a 1.1 m long SMF. Following compression, the resultant parameters for pulses were a duration of 82 fs, a central wavelength of 1593 nm with a bandwidth of 72 nm and a fundamental frequency of 42.4 MHz. In the final stage, the compressed pulses moved along a 24 cm long HNLF, where they underwent high-order soliton compression due to the combined effects of self-phase modulation and anomalous dispersion ($\beta_2<0$), following which the higher-order solitons were perturbed by higher-order dispersion and fission, emitting dispersive waves in normal dispersion wavelength window. Fission followed by soliton self-frequency shift (SSFS) caused the central wavelength to shift to 1315 nm, with a decrease in output pulse duration to 29 fs and an average power of 2.6 mW. The central wavelength can be shifted even to 1249 nm depending on the input power.

In 2019, Y. Qin *et al.* [165] developed a high-power femtosecond fibre laser at 1300 nm. They used a ring cavity EDFL with a CNT-saturable absorber as an oscillator. The oscillator emitted sub-picosecond pulses with a repetition rate of 53.48 MHz and an average power of 1.5 mW. As a result of the first amplification by EDFA, the output power was increased to 100 mW, while the spectrum broadened to 38 nm due to the self-modulation process. Then, the pulse generation was divided into two main parts: 90% of power for the signal seed and 10% for the pump of the optical parametric chirped-pulse amplifier. The primary part of power (90 mW) propagated through a 180 cm long SMF to compensate pulse duration to 80 fs and through a 5 cm long HNLF to generate a supercontinuum (SC) centred at a wavelength of 1300 nm which was used as a signal seed source. With only 10% of power, the second arm was necessary to amplify the 1543 nm pulse generation. This arm included a 5 nm bandpass filter, 1.6 km long SMF, delay line, and second EDFA. The SMF was needed to generate down-chirp pulses, while the delay line was required to synchronise both generation parts before the main amplification stage. In the final step, combined pump and signal seed pulses were directed to the Er/Yb doped double-clad amplifier in which 1543 nm pulse generation from the second arm amplified the 1300 nm signal. After passing through a dispersion-shifted fibre (DSF), which reduced the overall dispersion, the output signal at 1300 nm had a pulse duration of 306 fs, a peak power of 37 kW, and an average power of 1.1 W.

Erbium-doped fibre lasers exhibit high optical conversion efficiency, stability, and reliability. However, non-invasive optogenetics needs a laser source with a low average power and a high peak power of up to a hundred kilowatts, which is possible in fibre lasers with low repetition rates (1-10 MHz).

Ytterbium-doped fibre lasers are characterised by high efficiency, a broad emission spectrum of 1030-1070 nm [154], and can provide high output powers to tens of kilowatts. One of the examples is the 100 ps YDFL with an average power of 22 W, demonstrated by P. Muniz-Cánovas *et al.* [166]. Their laser had a Fabry-Perot cavity with 100% and 10% reflection fibre Bragg grating-couplers and a 15 m long Ytterbium-doped fibre (YDF) pumped by 976 nm laser diodes. The system was designed to generate pulses at a wavelength of 1061 nm with a narrow bandwidth of 2 pm. However, the average power is too high to implement this laser system for biomedical purposes.

Another possible method for generating mode-locked pulses in Yb-doped fibre lasers is using a nonlinearly amplified loop mirror (NALM) [167], [168]. A.F.J. Runge *et al.* [167] demonstrated a figure-eight laser that included a nonlinear amplifying loop mirror and a unidirectional ring (UR) loop. Yb-doped fibres of different lengths in both loops compensated for cavity losses and provided nonlinear transmission. The loops were made of PM SMFs and PM YDFs pumped by 980 nm laser diodes through wavelength division multiplexers (WDMs). The UR also included an isolator, a bandpass filter, and an output coupler. The laser system generated 120 fs pulses with a peak power of 7.5 kW and a repetition rate of 1.7 MHz at a central wavelength of 1030 nm. This all-polarisation-maintaining fibre laser can be used as a master oscillator for a laser system with an operating wavelength of 1100-1350 nm.

One way to shift the operating wavelength from 1030-1070 nm to the region of the second tissue transparency window is using a soliton self-frequency shift. D.A. Sidorov-Biryukov *et al.* [154] demonstrated a highly nonlinear photonic crystal fibre (PCF), which could shift the operating wavelength from 1058 nm to 1400 nm. A 30 cm long PCF and a solid-state Ytterbium mode-locked laser were used to produce 100 fs pulses with a peak power of around 1 kW and a repetition rate of 70 MHz.

Despite notable progress in laser technology, studies of NIR-II fibre lasers generating femtosecond pulses at a low repetition rate are still ongoing. Therefore, it becomes essential to innovate and create new sources of high-peak-power ultrashort pulse lasers to attain robustness, stability, and effortless self-starting within the desired wavelength range.

4.3 Development of Compact High-Peak Power Fibre Laser

4.3.1 Master Oscillator

The primary conditions for a fibre laser operating at a second tissue transparency window are high stability, minimal noise propagation, and a low repetition rate of the master oscillator to achieve high peak power after the amplification stages.

The figure-eight master oscillator configuration is highly versatile and suitable for accommodating various operational conditions. Seed lasers based on intracavity birefringent elements, saturable absorbers, or reflectors have drawbacks such as the need for constant polarisation control [169], laser power limitation due to low-temperature thresholds of saturable absorbers [157], and optical spectrum modulation due to broadened reflections or a modeless behaviour [170]. Passive mode locking without these elements can be achieved within the cavity by using a unidirectional loop together with a nonlinear amplifying loop mirror. There are notable advantages to using this setup because the noise generated in the NALM can be controlled by manipulating the dispersion within the laser cavity [171]. By changing the total group delay dispersion, the amplitude of the noise can be reduced, improving the signal-to-noise ratio [172]. This is beneficial for the precise tuning of the required laser parameters since the overall dispersion response of the resonator can be easily controlled by adjusting the length of the resonator or integrating dispersion-compensating fibres.

Figure-eight lasers with YDF NALMs feature self-mode locking, long-term stability, and an operational central wavelength ranging from 1030 to 1070 nm [168]. This wavelength can be transitioned into the 1200 nm range due to gain-managed nonlinearity effects.

Polarisation-maintaining fibres significantly contribute to the stability of the master oscillator by reducing the laser sensitivity to polarisation changes due to bending, twisting, or environmental stress on the fibre. PM lasers maintain the quality of the signal output parameters and effectively balance the nonlinear phase shifts between polarisation modes. The schematic view of the PM Yb-doped fibre laser with NALM and UR loop is shown in Figure 4.4.

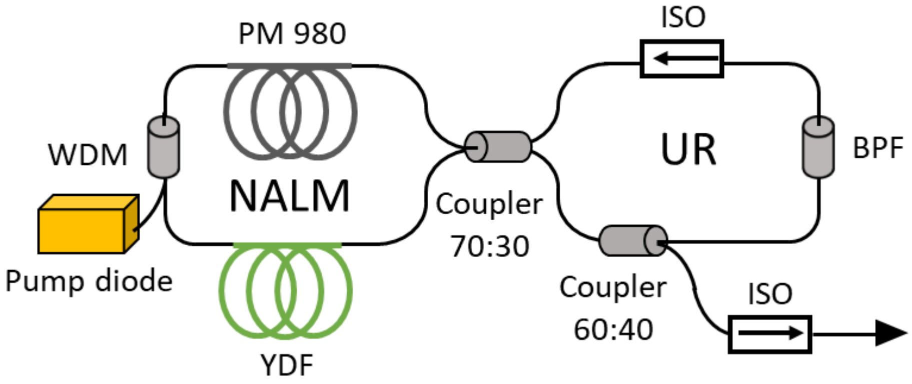

Figure 4.4. Schematic diagram of figure-eight Ytterbium master oscillator.

The nonlinear amplifying loop mirror includes a 2 m long 6/125 polarisation-maintaining Ytterbium-doped fibre (Nufern, PM-YSF-HI-HP) pumped by a 976 nm butterfly laser diode (UM96Z440-76) via a polarisation-maintaining WDM. The NALM is connected to the unidirectional loop by a 70:30 coupler with a PM980 fibre.

The UR loop includes an isolator, a bandpass filter (BPF), and an output coupler (60:40). The isolator blocks the backward propagating light that causes destructive interference, while bandpass filter selects a centre wavelength of 1064 nm, reducing noise, suppressing spontaneous emission, and enhancing the resonant response of the loop cavity.

The NALM includes an additional 13 metres of PM980 fibre to achieve a low repetition rate required for the laser application for two-photon conversion of light-sensitive proteins. The developed laser exhibits excellent stability, operating with a repetition rate of 9.1 MHz.

The repetition rate of the MO system can be further decreased up to 1 MHz by adding hundreds of PM980 fibre, because pulses propagating through long resonators have a lower repetition rate [150]. However, it leads to laser instabilities due to the influence of optical nonlinear phenomena such as self-phase modulation (SPM) and stimulated Raman scattering (SRS) inside long fibre cavities with normal dispersion.

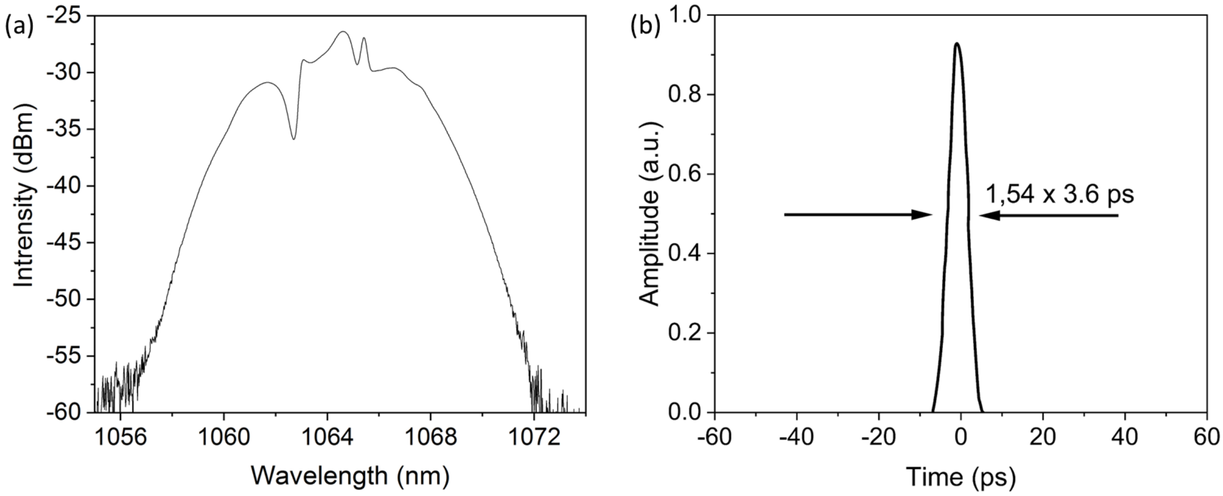

Figure 4.5. Laser characteristics of the master oscillator: (a) the optical spectrum with a central wavelength at 1064 nm; (b) autocorrelation trace with a pulse duration of 3.6 ps.

The full width half maximum (FWHM) of the MO optical spectrum is 2 nm (Fig. 4.5 (a)), while a pulse duration is about 3.6 ps (Fig. 4.5 (b)). The average power of the master oscillator is 1.4 mW. The output coupler is combined with an isolator to prevent the back reflection from the amplifier stages.

A compact, environmentally stable mode-locked all-polarisation maintaining fibre laser with a NALM and single pump module is developed for further amplification and wavelength shifting from 1064 nm to the NIR-II range. The following section will describe subsequent laser amplifier and wavelength shifting stages.

4.3.2 Amplification and Wavelength Shifting Stages

To increase the average power of the master oscillator, following preamplifier and amplifier stages are required in the laser system. A schematic representation of these stages is shown in Figure 4.6.

In the preamplifier stage, to selectively amplify a specific wavelength while reducing the gain of unwanted noise, a bandpass filter is installed after the master oscillator. The main element of this pre-amplification step is a 6/125 PM Yb-doped optical fibre pumped by a 980 nm laser diode. An optical isolator is included in the scheme to prevent back reflections from the following amplification stages, which could damage vulnerable optical components in the pre-amplification segment. The 99:1 optical coupler is used as a controller tool to measure the output power and optical spectrum of a femtosecond laser operating at a wavelength of 1064 nm after preamplifier stage.

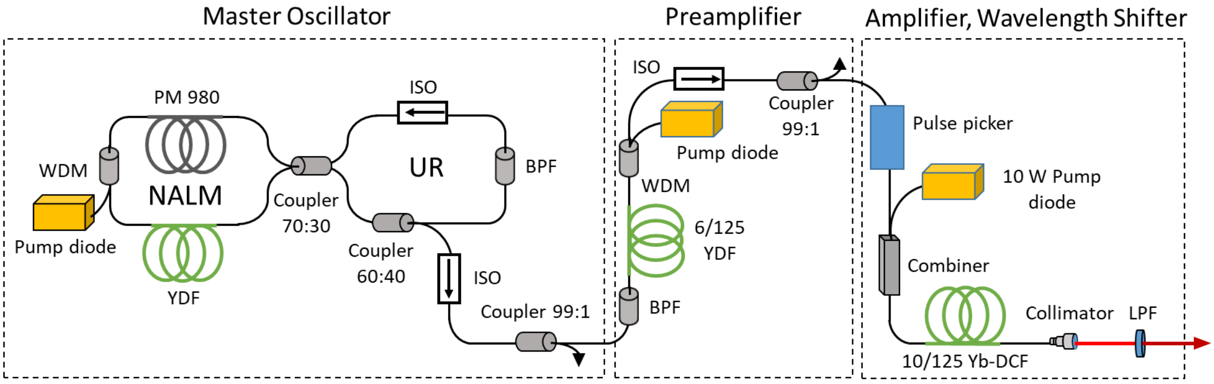

Figure 4.6. Schematic diagram of 1170 nm fibre laser.

Increasing the pump power significantly affects the laser output power, amplifying it approximately 43 times. The correlation between the input pump power and the output power of the preamplifier is shown graphically in Figure 4.7.

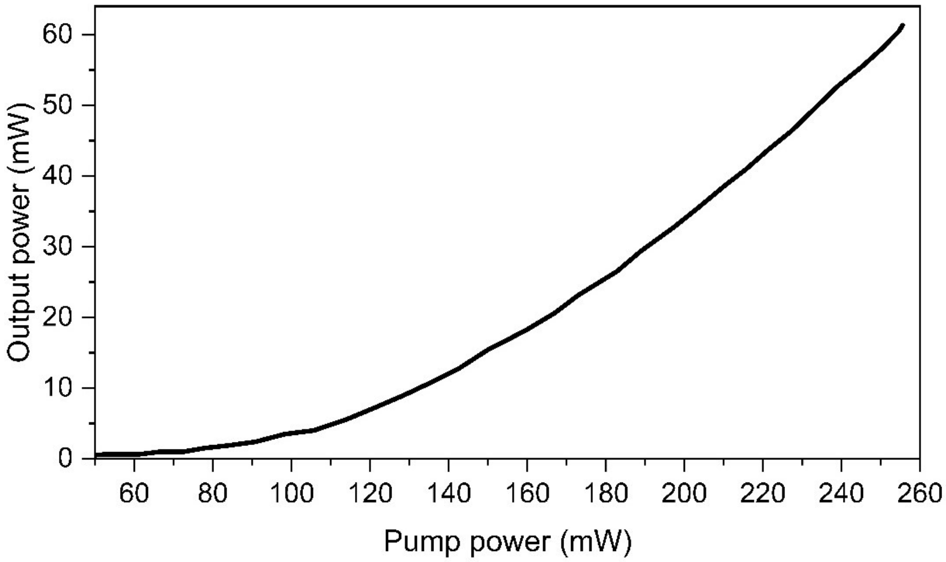

Figure 4.7. Dependence of the output power of the preamplifier on 980 nm laser diode pump power.

The increase of the 980 nm laser diode pump power from 60 mW to 255 mW correspondingly enhances the output power of the 1064 nm fibre laser from 1.4 mW to 61 mW. As a result, the pulse energy grows to 6.7 nJ, and the peak power reaches a value of 1.75 kW.

To meet the demands of biomedical applications requiring a high peak power while maintaining low average power, the pulse repetition rate of the laser was decreased by incorporating a pulse picker at the final stage. Despite the notable energy losses, worsening the signal-to-noise ratio, and increased system complexity, an acousto-optic modulator (AOM) used as a pulse picker in an amplifier offers the benefit of a tunable pulse repetition rate from tens of MHz to hundreds of kHz.

The AOM operating at 150 MHz (1060 nm) with a Gooch & Housego driver, a pulse picker board (Evolase), and a photodetector (Hamamatsu) were integrated into the laser system. The driver generates a short radio frequency signal that creates an acoustic wave within the modulator crystal to deflect pulses in a specific direction. Selected pulses subsequently pass through an aperture designed to block unwanted ones. The system offers real-time monitoring and control of the laser repetition rate by periodically triggering the AOM. This pulse picker tool effectively reduces the repetition rate of the fibre laser from 9.1 MHz to 608 kHz. The RF spectra of input and output signal of pulse picker is shown in Figure 4.8 (a), while in Figure 4.8 (b), the fundamental frequency (608 kHz) of the RF spectrum after pulse picker is depicted.

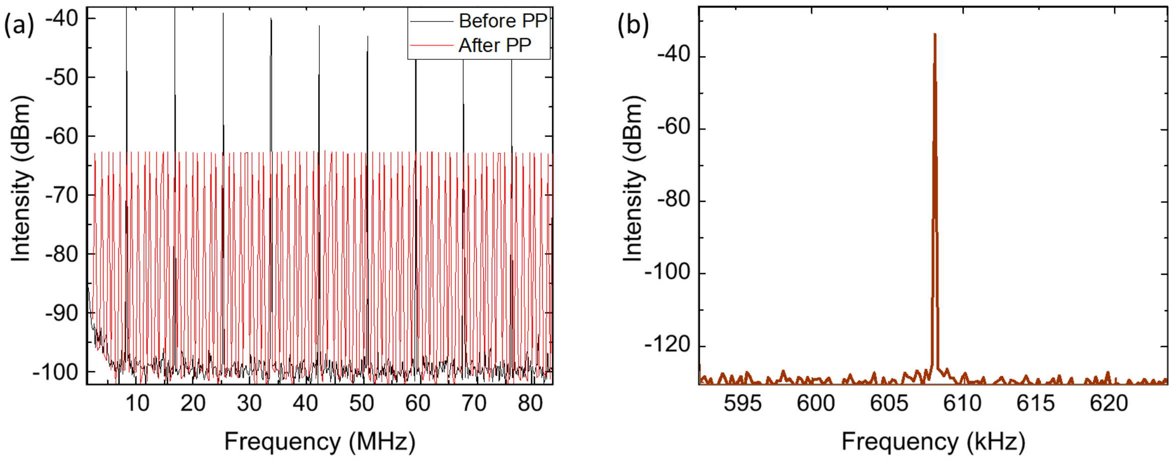

Figure 4.8. (a) RF spectra of the YDFL before and after pulse picker (PP); (b) fundamental frequency (608 kHz) of the YDFL after pulse picker.

The final step includes the wavelength shift from 1064 nm to the second near-infrared region required for two-photon phytochrome conversion. However, this process is challenging for an all-normal dispersion mode locked YDF laser operating in a dissipative soliton regime.

The difficulty arises from the restricted availability of optical fibres with large core diameters and anomalous dispersion characteristics within this wavelength range. For example, the wavelength shifts through nonlinear mechanisms in fibres, such as soliton self-frequency shift, result in a relatively small output pulse energy because the low damage threshold of the available fibres limits the increase of pump power. However, the generation of redshifted high peak power pulses is possible by generating short noise-like pulses (NLPs) based on a method of cascaded Raman scattering.

Noise-like pulses typically occur as nanosecond-scale waveforms comprising an inner structure with picosecond pulses characterised by irregular amplitudes and durations. A nonlinear amplifier can be used to increase their emission energy and shift the spectrum towards longer wavelengths. These simultaneous amplification and spectral broadening are possible in Yb-doped fibres, where rare-earth dopants amplify the 1064 nm signal, while the interaction of high-intensive light with dielectric medium results in nonlinear effects such as

Raman scattering [159]. This phenomenon is characterised by the transfer of energy from input photon to lower-energy photon (first-order Stokes wave), whose frequency difference is equal to the vibrational excitation modes of the medium. For silica fibres, this frequency difference typically does not exceed 13.1 THz.

When the first-order Stokes wave reaches a sufficiently high intensity, it has the potential to trigger additional Raman scattering, giving rise to a second-order Stokes wave that is shifted by the same frequency difference [173]. The energy transfer process and the generation of higher-order Stokes wave can be iterated multiple times, continuing until the pump power has a sufficient level to surpass a Raman threshold in the fibre. This phenomenon of cascaded Raman scattering for the *n* th Stokes wave depends on the interaction between Raman gain coming from *(n-1)* th Stokes wave and losses occurring due to the energy transfer to the *(n+1)* th Stokes wave [174].

The amplifier and wavelength-shifting stage includes a 3 m long double-clad large mode area Yb-doped PM fibre (PLMA-YDF-10/125-VIII, Coherent) pumped by a 10-W 976 nm laser diode through a high-power combiner. The stimulated Raman scattering effect in the 10/125 Yb-DCF fibre is noticeable with the increase of the pump power. Once the pump power surpasses 1 W, a Raman threshold is passed, and pump energy converts to the Stokes wave energy, resulting in the first-order Stokes wave appearing at a wavelength of 1114 nm. Further power increase until 1.7 W leads to the growth of the amplitude of the first-order Raman component. A pump power of 1.7 W stimulates the energy transfer to the appearing second-order Stokes wave (1170 nm). At a pump power of 2.3 W, the second-order Raman component reaches maximum intensity at a central wavelength of 1170 nm with a bandwidth of 80 nm (Fig. 4.9 (a), black curve).

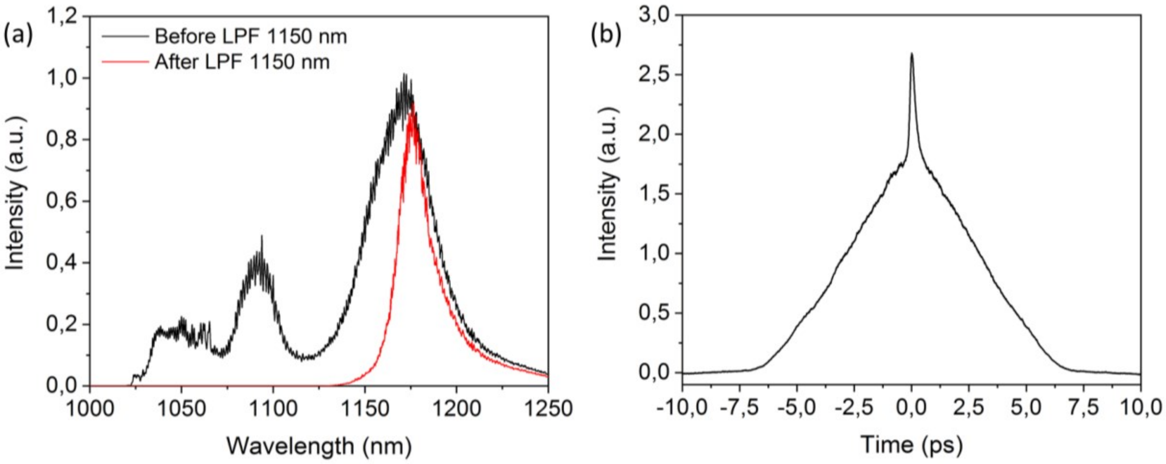

Figure 4.9. Laser characteristics of 1170 nm fibre laser: (a) the optical spectrum before and after 1150 nm long pass filter (LPF); (b) autocorrelation trace.

The transition from optical fibre to free-space light propagation using a collimator allows the laser output parameters to be preserved since the pulses can be modified and evolve during propagation in the fibre due to dispersion and nonlinear effects. An 1150 nm long pass filter is added to neglect shorter wavelength components of NLPs (Fig. 4.9 (a), red curve).

The developed laser system based on YDFL and YDFA is a versatile source with a tunable operating wavelength from 1064 nm to 1170 nm and a repetition rate from 0.6 MHz to 9.1 MHz. Figure 4.9 (b) illustrates an autocorrelation trace featuring a distinctive noise-like pulse, where a narrow spike is superimposed on a 5-ps baseline pedestal. The laser's average power is 250 mW, which relates to a pulse energy of 411 nJ and a peak power of 82 kW.

4.3.3 Laser Size Miniaturisation

One of the main benefits of fibre lasers is their remarkable compactness, allowing them to be conveniently folded and occupy minimal space. The developed laser system, operating at a wavelength of 1170 nm, is efficiently housed in a multi-tier shelving system inside a compact box measuring just 34 cm x 46 cm x 46 cm. Figure 4.10 demonstrates the developed NIR-II laser in its robust metallic case.

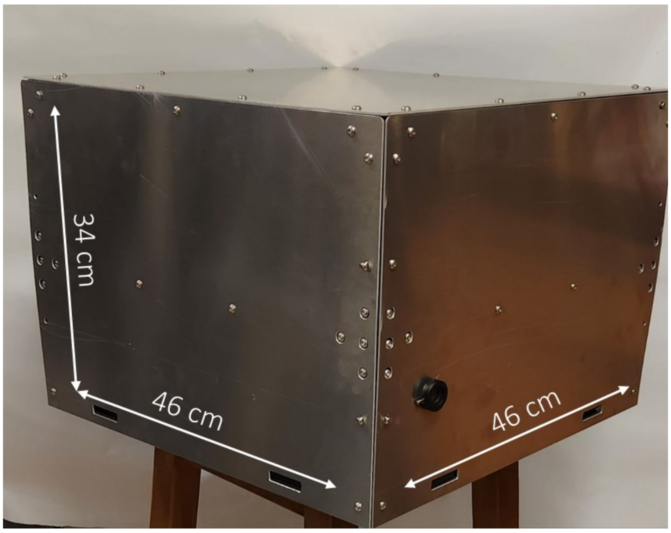

Figure 4.10. Compact laser source operating at a wavelength of 1170 nm.

This small and portable laser system can be easily relocated to biological laboratories or medical research institutes, where it finds applications in exploring light-sensitive proteins or conducting *in vivo* optogenetics studies on animal samples.

4.4 Conclusion

The developed fibre laser is a robust, compact, and tunable source, offering versatile utility across biological and medical applications such as coherent tomography, low speckle, and multiphoton imaging in which light penetration into biological tissues is essential. Its operational wavelength can range from 1064 nm to 1170 nm, covering part of the second tissue transparency window. The laser system effectively competes with Ti:Sa laser and OPO/OPA systems regarding laser output performance in the NIR-II range and outperforms crystal-based solid-state lasers in compactness and cost-effectiveness. Moreover, the fibre laser is superior to gas and liquid lasers due to a tunable range of operating wavelengths and to semiconductor lasers due to reliability and robustness to changing environmental conditions such as vibrations or temperature fluctuations.

The compactness (34x46x46 cm) and portability of the system ensure that it can be effortlessly transported without concerns of potential damage. Its design, which minimises the need for optical adjustments through the reduced use of free-space optical elements, and its user-friendly interface for controlling the laser pump diodes via a laptop application establish the developed EDFL as the ultimate laser source choice for medical and clinical studies of biological samples or animals.

The tunable repetition rate can extend to lower values (608 kHz), resulting in the generation of high-peak pulses with minimal average power. The significance of maintaining a low average power is necessary to prevent tissue overheating, damage, or shrinking [3]. High peak power is essential for facilitating two-photon processes, which enable precise stimulation, manipulation, or control of specific target cells.

As shown in Chapter 3 (Subsection 3.5), the minimum laser energy fluence required for the two-photon conversion of *Deinococcus radiodurans* phytochrome is 41 mJ/cm^2. The preliminary estimations show that the developed laser with an average power of 250 mW focused through a lens (F=50 mm) should deliver the required energy fluence to brain tissues through the skin and skull without overheating. Since the laser beam will be focused on the brain cortex, the beam diameter on the skin surface will be around 840 μm. With the average power of 250 mW, the energy fluence of light onto the skin will be 0.15 mJ/cm^2. Figure 4.11 shows how a focused laser beam can pass through the skin and skull.

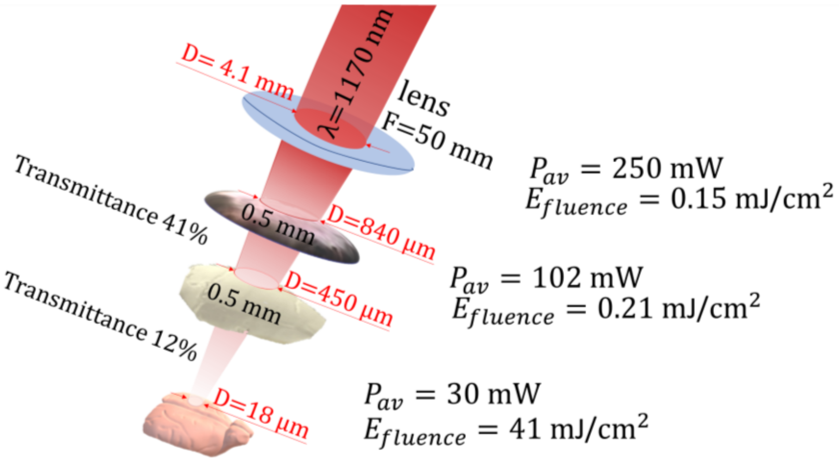

Figure 4.11. Schematic representation of light propagation through biological tissues and reaching a brain cortex.

The transmittance measurements of skin samples demonstrated that only 41% of initial average power passes through 0.5 mm mouse skin samples (Subsection 2.3.4). As a result, an average power of 102 mW will reach the mouse skull. At the same time, the beam diameter will experience a decrease to 450 μm, leading to an energy fluence of 0.21 mJ/cm^2.

After propagating through the skin and skull, only 12% of initial power (~30 mW) will reach the brain cortex. Since a focused beam spot will be small enough (D~18 μm), the energy fluence can get the required value (41 mJ/cm^2) for potential non-invasive neurostimulation by two-photon conversion of phytochrome.

As shown in Subsection 2.3.4, minimal tissue damage begins at laser radiation doses greater than 24062 J/cm^2. If the exposure time is less than 1 s, laser light can be delivered to the brain cortex through the skin and skull without adverse effects such as heating or damage. In this case, the dose to the skin and skull will be no more than 90 J/cm^2 and 128 J/cm^2, respectively. For the brain cortex, due to the small diameter of the beam, the dose can reach 23590 J/cm^2, which is still less than the tissue damage threshold but close to the initiating lesion.

This effect can be mitigated by reducing the average power lever, which is possible by using two or more laser beams that will pass through the skin and skull at different points and focus on the same place in the brain cortex or deeper layers of the brain. Besides minimally invasive neurostimulation, which involves cutting the skin and passing light only through the skull, another method is to increase the transmission of light through the skin. This is possible through tissue clearing using special chemical techniques that make biological samples "transparent" [29].

The laser system opens the potential for advancements in biomedicine, particularly in non- or minimally invasive therapies for neurological disorders. The laser operating wavelength is well-matched for the two-photon activation of a range of photoactuators (Fig. 3.1), including VChR1, NpHR, ReaChR, Jaws, and PhyB, which can require less laser energy fluence for the stimulation of two-photon conversion process and, therefore, less average power. For example, *Deinococcus deserti* phytochrome needs twice smaller laser energy fluence (18 mJ/cm^2) to begin 2P conversion from the Pr to the Pfr state [26].

Applications of the developed laser encompass various uses, such as exploring the nonlinear optical characteristics of novel optical materials, studying two- or three-photon conversion, and analysing fluorescence emissions of proteins applying as biosensors, markers, or optogenetic tools.

Chapter 5

Laser Source for Multimodal Cancer Diagnostic

5.1 Motivation

According to the World Health Organisation, more than ten million people die due to cancer every year in the world [175]. This term includes a large group of diseases that influence different parts of the body. The most prevalent types are breast, lung, colorectal, prostate, stomach, and brain cancers.

A common characteristic among various types of cancer is their tendency to present higher probability rates with a person's age [176]. In age groups under 20 years old, only one of 4000 examined people has a cancer diagnosis [177]. The risk factor significantly increases for people who are older than 60 years. In this case, every hundredth respondent has a cancer diagnosis. As global life expectancy continues to rise, having reached an average of 73 years in 2023 [68], the challenge of managing an increasing population of individuals with cancer tumours has emerged as a significant healthcare concern on a global scale.

The early detection of diseases can play a pivotal role in addressing this issue, as any delay in initiating cancer treatment, even as short as 12 weeks, noticeably impacts the likelihood of a patient's survival and consequently influences the global prognosis [178].

One of the most widely used methods for determining pathology is the optical one [179]. The presence of cancer affects changes in tissue morphology and metabolic activity that can be recognised by bioimaging [180]-[182]. Compared to traditional methods such as screening tests, biopsy and blood tests, modern imaging studies based on laser sources have advantages such as non-invasive detection and high resolution of the biological tissues and tumours. These benefits lead to the popularisation of the development of the laser as a light source in cancer detective devices.

Laser sources operating within the biological windows show significant potential as imaging tools for biological tissues. These near-infrared tissue transparency windows possess remarkable attributes, facilitating the deep penetration of laser radiation for effective cancer visualisation applications. In these wavelength regions, the light absorption by water, oxy-, deoxygenated blood, and fat is minimal [24].

The first window of this spectral region covers 700-950 nm wavelength. Experimental and computational results confirm that lasers operating in the NIR-I achieve imaging depths greater than those possible in the visible range (Fig. 2.3) [183].

Currently, this is the most common optical window for imaging and photodynamic therapy applications due to the availability of high-power laser sources such as Cr:forsterite, Ti:Sa, operating at these wavelengths (Fig. 1.1).

Furthermore, these wavelengths enable the excitation of a diverse array of biomarkers. Various fluorophores, including nanoparticles engineered to fluoresce under near-infrared light, are widely employed in applications such as bioimaging and photodynamic therapy [184], [185]. Additionally, the utilisation of fluorescent proteins (Fig. 3.1) activated through two-photon excitation permits precise targeting imaging at tissue focal points, effectively mitigating the risk of photodamage and photobleaching in the surrounding areas [133].

Three- and multiphoton excitation of naturally occurring fluorescent molecules like flavins enables the realisation of fluorescence imaging without the need for additional contrast agents [186]. This advancement facilitates the ability to visualise multiple cellular structures or molecules with distinct excitation wavelengths within a single experiment [187].

Femtosecond pulsed lasers operating in the first tissue transparency window find application in various biomedical fields, including microscopy and optical coherence tomography. They have emerged as a non-invasive and painless approach for conducting tissue studies, both *ex vivo* and *in vivo*.

The second biological window is located between blood and water absorption peaks (1100-1350 nm). OCT systems utilising 1300 nm laser sources showcase 2D and 3D imaging of the mouse brain with depths exceeding 1 mm [188], [189].

The third near-infrared tissue transparency window is located between two high water absorption peaks and covers a wavelength range from 1550 nm to 1870 nm. Laser sources operating at these wavelengths can effectively penetrate biological tissues, such as cancer tumours, and can be applied in morphological tissue imaging using three-photon fluorescence of naturally existing fluorophores such as collagen, keratin, and lipofuscin [190].

Moreover, the third tissue transparency window offers higher contrast images compared to the second window, because longer wavelengths have reduced Rayleigh and Mie scatterings [111], [191]. For instance, at a penetration depth of 1.1 mm, the signal-to-noise ratio is approximately 5 dB at 1700 nm, while it is 0 dB at 1300 nm [189]. This implies that the longer wavelength provides an improvement in image quality, resulting in enhanced contrast. Laser sources operating at a wavelength range of 1550-1870 nm can be used in various promising optical techniques applicable for medical purposes.

The second advantage of using a pulsed laser with a 1550-1870 nm wavelength is the possibility of doubling the frequency of laser radiation to operate in the first biological window. An ultrashort pulsed laser operating at a wavelength range between 800 nm and 935 nm can offer fluorescence imaging of metabolic activity indicators [192]. Understanding tissue metabolism and molecular fingerprinting at the cellular level can aid in early detection, therapy monitoring, and pathology characterisation.

The multimodal imaging technique based on the NIR-III laser and second harmonic generation at the NIR-I spectral region could be used for cancer diagnosis and therapy monitoring since light can penetrate deeply into the tissues due to low water absorption and optical scattering at these wavelength regions [193].

5.2 Review of NIR-III Pulsed Laser Sources

[**Section 5.2, pages 83-91 incl. Figure 5.1 redacted from open access version**]

5.3 Development of Compact 1700 nm Laser Source

In comparison to solid-state lasers, fibre lasers operating at a NIR-III wavelength range are preferable sources for biomedical applications. They satisfy main requirements such as robustness, stability, compactness, and minimal realignment.

The development of a fibre laser source operating at a wavelength of 1700 nm and doubling frequency at a wavelength of 850 nm divides into four main parts: development of master oscillator, power amplifier, soliton self-frequency shift stage, and second harmonic generation (SHG) stage (Fig. 5.2).

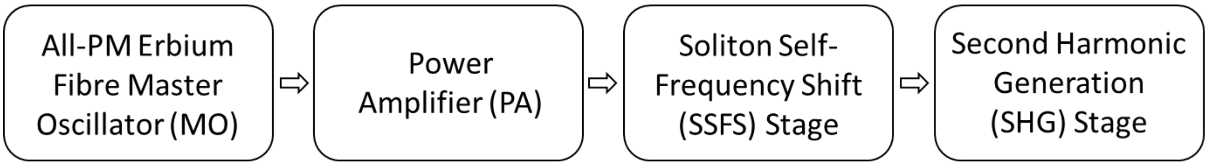

Figure 5.2. Schematic diagram of main stages of 1700 nm fibre laser with SHG stage.

5.3.1 Master Oscillator

To develop a 1700 nm fibre laser, it is important to focus on creating a master oscillator that possesses two essential characteristics: self-starting capability and high pulse stability. The most promising candidate that satisfies both requirements is a figure-eight all-polarisation-maintaining Er-doped fibre laser with a NALM. This choice is motivated by the fact that fibre lasers with NALM exhibit a higher stability level than fibre lasers based on saturable absorbers. Traditional saturable absorbers like SESAMs, as well as alternative options such as CNTs, graphene, black phosphorus, and topological insulators, have inherent limitations in terms of their intracavity power capacity, primarily due to their relatively low damage thresholds [157]. An all-PM Er-doped fibre laser without SAs is a robust system capable of sustaining higher intracavity power levels. It provides environmentally stable mode-locked laser operation insensitive to thermal and mechanical stress.

Figure 5.3 shows the all-PM fibre laser that has been developed using a nonlinear amplifier loop mirror scheme.

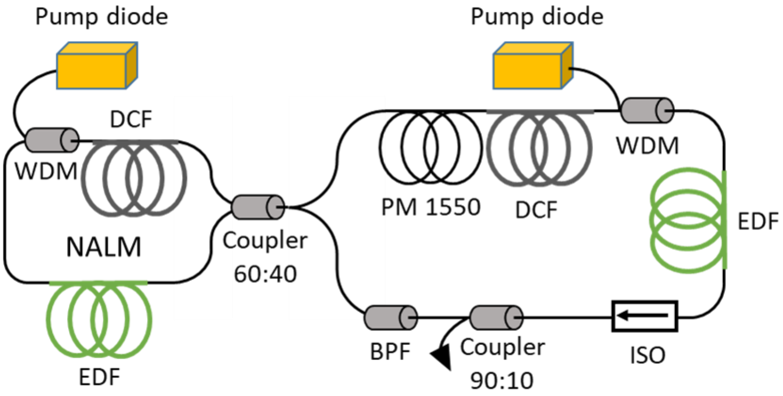

Figure 5.3. Schematic diagram of figure-eight master oscillator.

The advancement of NALM-based pulsed lasers offers notable advantages, primarily because the mode-locking technique does not need any specialised components within the cavity. The nonlinear amplifier loop mirror consists of a 60 cm long PM EDF (ER80 4/125 HD PM), pumped at 980 nm wavelength by a laser diode through a WDM. The WDM has a blocked fast axis of polarisation. The optical field from the NALM is launched into the unidirectional loop via the coupler with a splitting ratio of 60:40 and blocked fast axis of polarisation. The UR loop part has the twice shorter PM EDF than in NALM. The second laser diode at 980 nm combined with a fused WDM was used to pump the EDF added in the UR to provide gain. The purpose of the PM isolator within the UR is to ensure the propagation of radiation in a unidirectional manner. Additionally, a bandpass filter is implemented in the UR loop to filter the spectrum, while a coupler with a ratio of 90:10 is used to extract a fraction of the power circulating within the cavity. To reduce the repetition rate to 10.94 MHz, a 5 m long PM 1550 fibre is incorporated into UR. The total net dispersion of about 0.1 ps^2 is achieved using 3 m of dispersion compensating fibre (PM2000D, Coherent) in both the NALM and UR loop sectors of the system.

The self-starting process of the seed laser begins when the pump power reaches 350 mW in the main laser diode and 350 mW in the NALM loop laser diode. Once initiated, the pump power is gradually reduced to 75 mW in the main loop and 100 mW in the NALM loop, establishing a pulse regime characterised by enhanced stability. In this configuration, the average output power is 1.5 mW.

The radio frequency (RF) spectra from the laser output were measured by the RF spectrum photodetector and analyser Rohde & Schwarz FSP. The fundamental repetition rate is 10.94 MHz. Figure 5.4 (a) shows the RF measurement with a span of 850 Hz and a resolution bandwidth (RBW) of 10 Hz, while Figure 5.4 (b) depicts the RF spectrum with a span of 0.5 GHz and a resolution of 100 kHz. A clean, noise-free RF spectrum proves the quality of the developed all-PM figure-eight master oscillator.

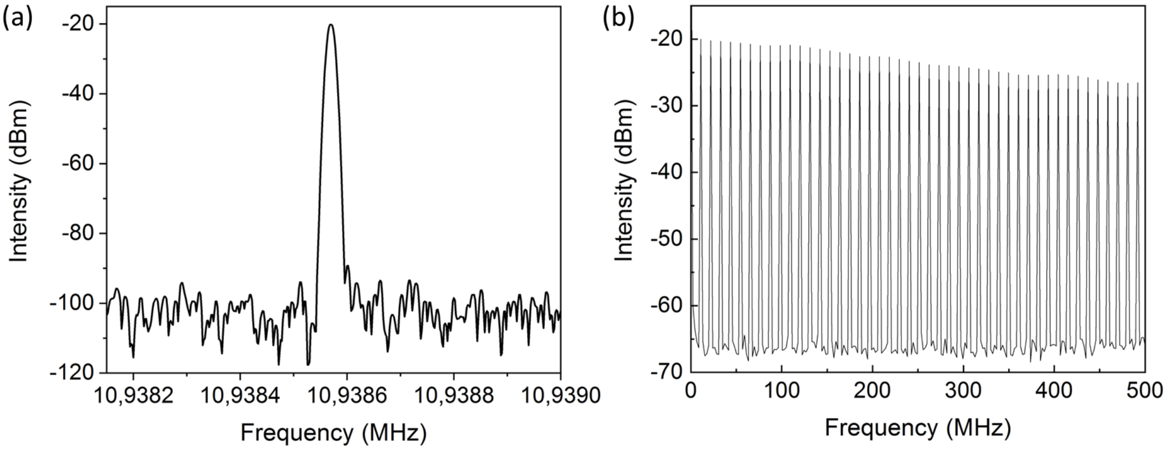

Figure 5.4. Radio frequency spectra with following parameters: (a) span: 850 Hz, RBW: 10 Hz and (b) span: 0.5 GHz, RBW: 100 kHz.

The optical spectrum of MO with a FWHM of approximately 6 nm centred at a wavelength of 1550 nm is shown in Figure 5.5 (a). The autocorrelation trace after MO is shown by black line in Figure 5.5 (b).

The autocorrelation trace after the master oscillator stage is approximately 1.7 ps. However, to mitigate the potential nonlinear effects that may arise in the preamplifier and amplifier stages, the pulse is stretched in a 60 m long PM dispersion-tailored fibre (Coherent, PM2000D). Implementing the fibre for pulse stretching increases the pulse duration to 21 ps. In Figure 5.5 (b), the red line shows the autocorrelation trace after pulse stretching in dispersion-tailored fibre.

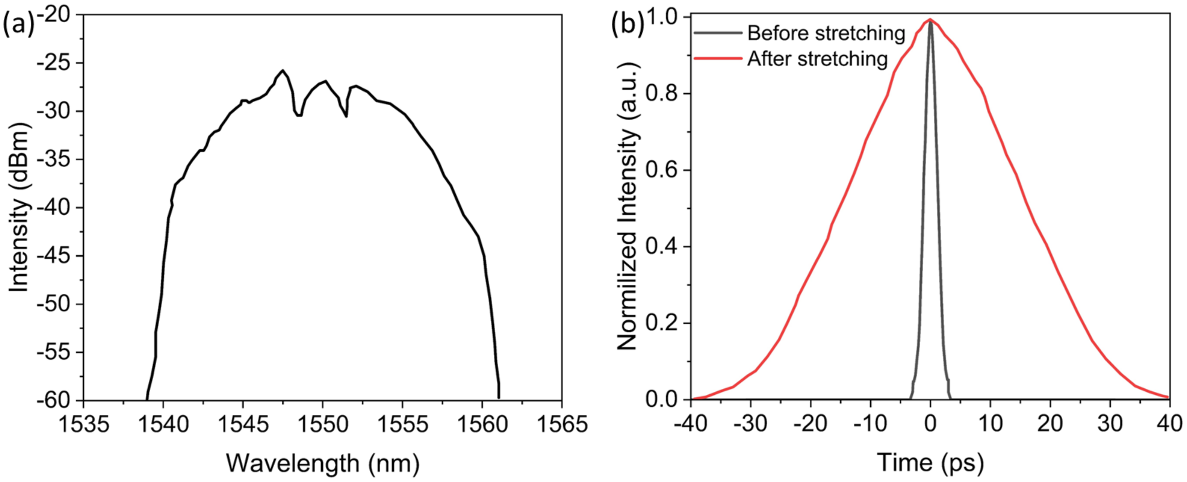

Figure 5.5. Laser characteristics of MO: (a) spectral FWHM of 6 nm; (b) autocorrelation traces of initial pulses of MO (black) and pulses stretched by 12 times (red).

To prevent back reflection and protect the seed laser from the generation of further amplifying stages, a PM isolator is installed in the output of the scheme. Moreover, an additional bandpass filter centred at 1550 nm was implemented to cut long tails of the pulse and avoid the amplification of spontaneous emission. A schematic diagram of the modified master oscillator is shown in Figure 5.6.

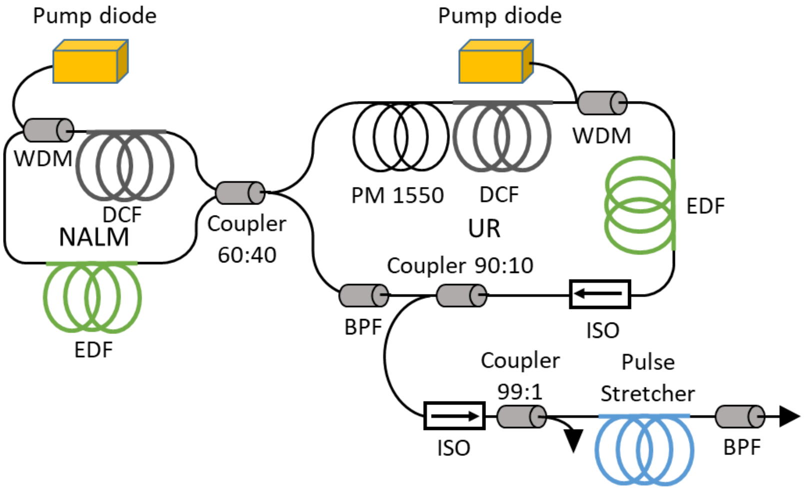

Figure 5.6. Schematic diagram of modified MO with output pulses stretched by 12 times.

5.3.2 Preamplifier and Amplifier

The following two stages are the Er-doped fibre preamplifier and amplifier. The preamplifier consists of 2 m long Er-doped fibre (Er30-4/125) pumped by the third 980 nm laser diode with a maximum output power of 450 mW. Figure 5.7 depicts a schematic view of the developed preamplifier and amplifier. When the pump power reaches the value of 250 mW, the average output power is 40 mW.

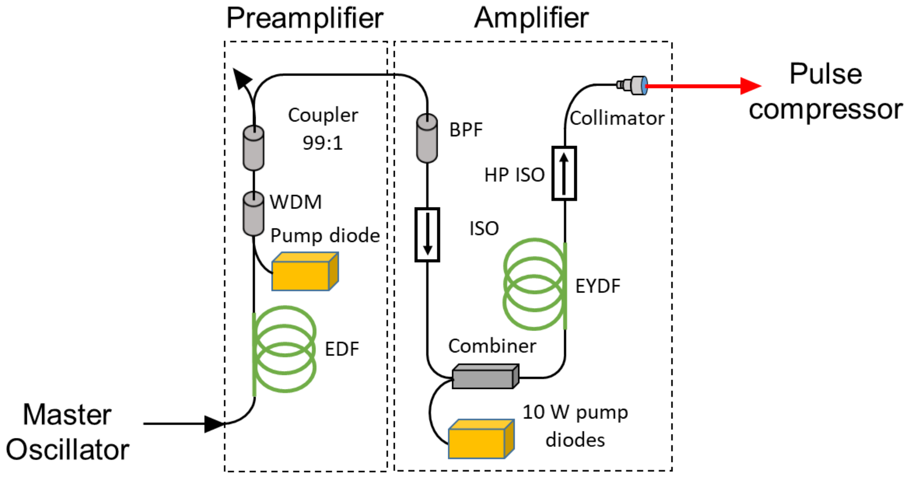

Figure 5.7. Schematic diagram of preamplifier and amplifier stages.

After preamplification, the pulses pass through BPF and isolator with a blocked fast polarisation axis. The bandpass filter helps to avoid amplification of noises, while the isolator prevents back reflection from the amplifier. The amplifier comprises a 2 m long, polarisation-maintaining double-clad Erbium/Ytterbium fibre (PM-EYDF-10/125, Coherent) that is pumped by a high-power 980 nm laser diode, capable of delivering a maximum output power of 10 W. Pre-amplified generation and 980 nm light are combined in a high-power PM combiner.

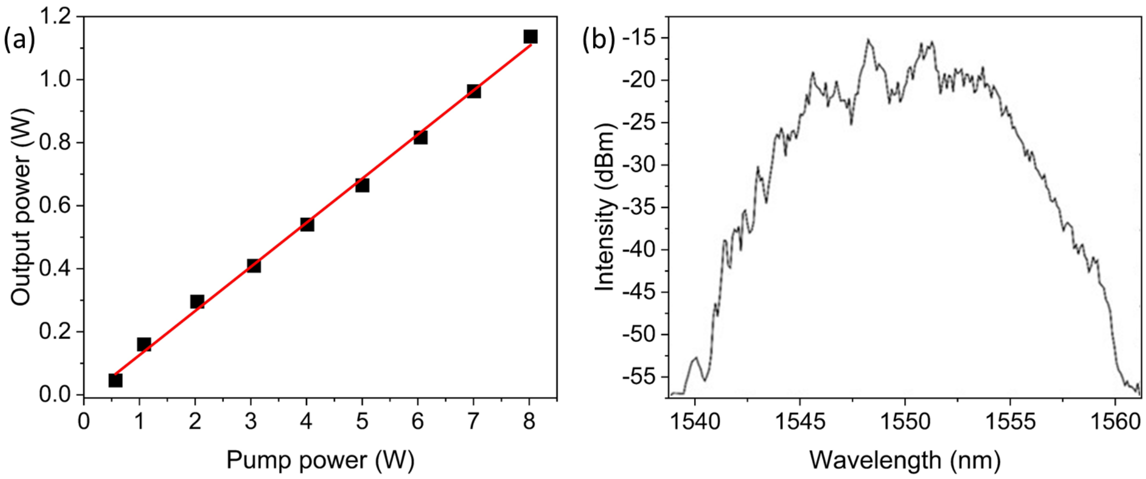

Figure 5.8. (a) Output power dependence on pump power; (b) the optical spectrum of pulse generation amplified until 1.1 W.

In the amplifier stage, the input power of the laser diode does not exceed the value of 8 W to avoid damage to the PM combiner. At this pump power level, the amplifier achieves a maximum average output power of 1.1 W, which scales linearly with pump power, indicating the potential for amplification up to the highest possible value. The dependency of the output power from the main amplifier on the pump power is illustrated in Figure 5.8 (a). The optical spectrum of pulse generation after two stages of amplification is shown in Figure 5.8 (b).

5.3.3 Pulse Compression

Following the amplification stage, the pulses undergo further processing to achieve pulse compression. The amplified pulses pass through a half-wave plate (HWP), a pair of transmission gratings with a density of 1200 lines per millimetre, and a roof mirror (RM). HWP is used to rotate linearly polarised light and reduce grating pair losses that depend on light polarisation. The schematic diagram of the pulse compressor stage is shown in Figure 5.9.

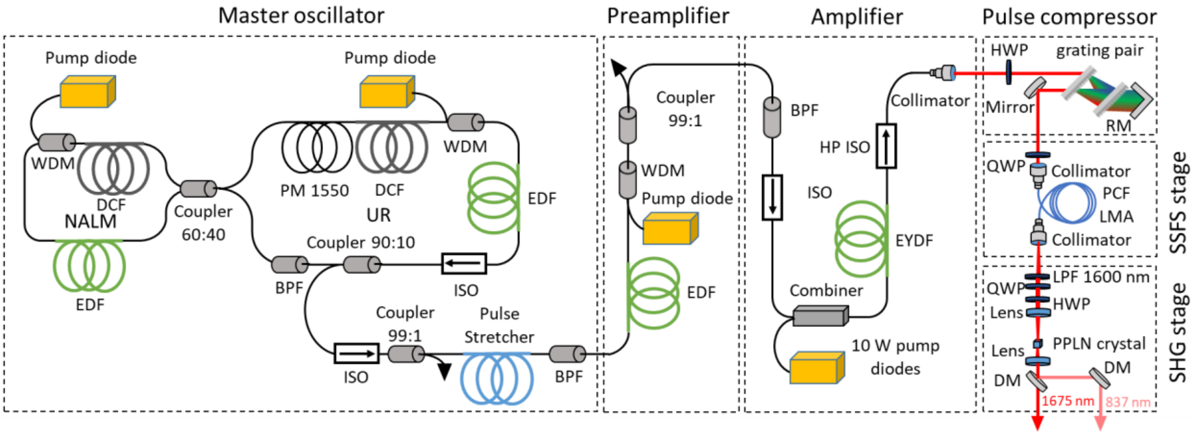

Figure 5.9. Schematic diagram of 1700 nm femtosecond laser with second harmonic generation at a wavelength of 850 nm.

To compensate for the temporal broadening experienced by a pulse as it propagates metres of fibre with normal dispersion and to counteract the distortion arising from the time delay among various spectral components travelling at varying speeds, a pair of gratings is introduced into the setup. These gratings diffract the pulses, affording precise control over their temporal characteristics.

A Treacy configuration induces negative dispersion by using a difference between the length of optical ways for various wavelengths. Initially, the first grating disperses incident light into various wavelengths, each following a distinct path to address the variation in their propagation speeds. Shorter wavelengths pass shorter paths, whereas longer wavelengths travel longer optical paths [244].

The light passing through the second grating results in a spatially incoherent beam. A roof mirror is integrated into the system to manipulate spectral components further. This mirror reflects the dispersed spectrum, doubling the optical path difference among the components. This scheme effectively compensates for the pulse broadening and resulting in a narrower pulse width. As a result of this process, the pulse duration is significantly reduced from 35 ps to 660 fs (Fig. 5.10 (a)), leading to a highly compact and intense pulse output with an average power of 920 mW and a repetition rate of 10.94 MHz.

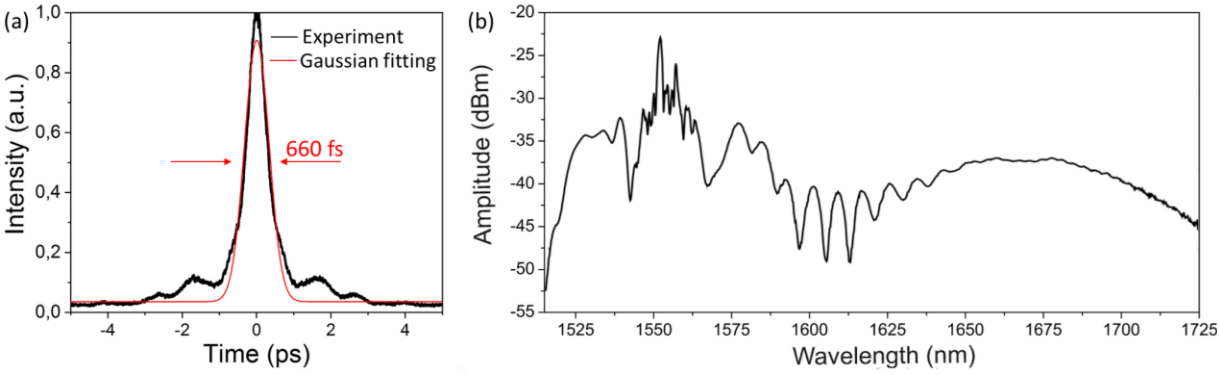

Figure 5.10. (a) Autocorrelation trace of the compressed pulse corresponding to the average output power of amplifier ~ 1 W; (b) optical spectrum at the output of PCF LMA with launched 660 fs pulses.

5.3.4 Soliton Self-Frequency Shift Stage

The next step is to shift the central wavelength of the laser system. Various methods, based on the nonlinear effects exhibited by optical fibres, are available to achieve a redshift of the wavelength from 1550 nm to the range of 1630-1700 nm. For example, in a soliton self-frequency shift, during propagation through a fibre, a soliton undergoes a change in its central frequency due to intrapulse Raman scattering.

However, standard SMF has a relatively high nonlinearity, which is a barrier to reaching output energy in the nanojoule scale required for bioimaging applications [245]. The desired pulse energy level and wavelength shift of a hundred nanometres can be achieved by carefully selecting fibre properties, including nonlinearity and dispersion coefficients.

For the SSFS effect, a large mode area photonic crystal fibre (PCF LMA-20, NKT Photonics) was chosen with dispersion coefficients β_2=-37 ps^2/km and β_3=0.15 ps^3/km at 1550 nm. The distinguishing feature of large-mode-area fibres is their low nonlinearity, which allows the generation of pulses with high energy [245]. In addition, PCF LMA offers the advantages of low bending losses and substantial tuning of the wavelength shift [246].

Since the wavelength shift caused by SSFS in PCF LMA requires a sufficient level of pulse energy, which depends on the polarization of the light [247], a QWP was added to the laser setup before the PCF LMA fibre. QWP creates elliptical polarization, which allows the generation of a higher power in the fibre than linear polarization at the same wavelength. The schematic representation of the optical components in the SSFS stage is shown in Figure 5.9.

Pulses with a central wavelength of 1550 nm and a duration of 660 fs are launched into the LMA fibre through a collimator. High-order solitons, propagating through PCF LMA, experience perturbation inside the fibre, which leads to the soliton fission phenomenon [231]. High-order solitons decay into fundamental solitons of different widths with initially a central wavelength of 1550 nm. Intrapulse Raman scattering leads to the SSFS effect, shifting the highest-order fundamental soliton central wavelength to up to 1700 nm. The spectrum at the output of PCF LMA with launched 660 fs pulse with the peak power of 24 kW is shown in Figure 5.10 (b).

Using a 1600 nm LPF filters the optical spectrum, reducing the peak at 1550 nm. The optical spectra of soliton self-frequency shift in a 1 m long of LMA-20 fibre, as a function of the input power, are shown in Figure 5.11 (a). At an average pump power of 221 mW, the central wavelength of the output spectrum is at 1625 nm with a soliton duration of 165 fs and an average power of 55 mW (Fig. 5.11(a), button figure).

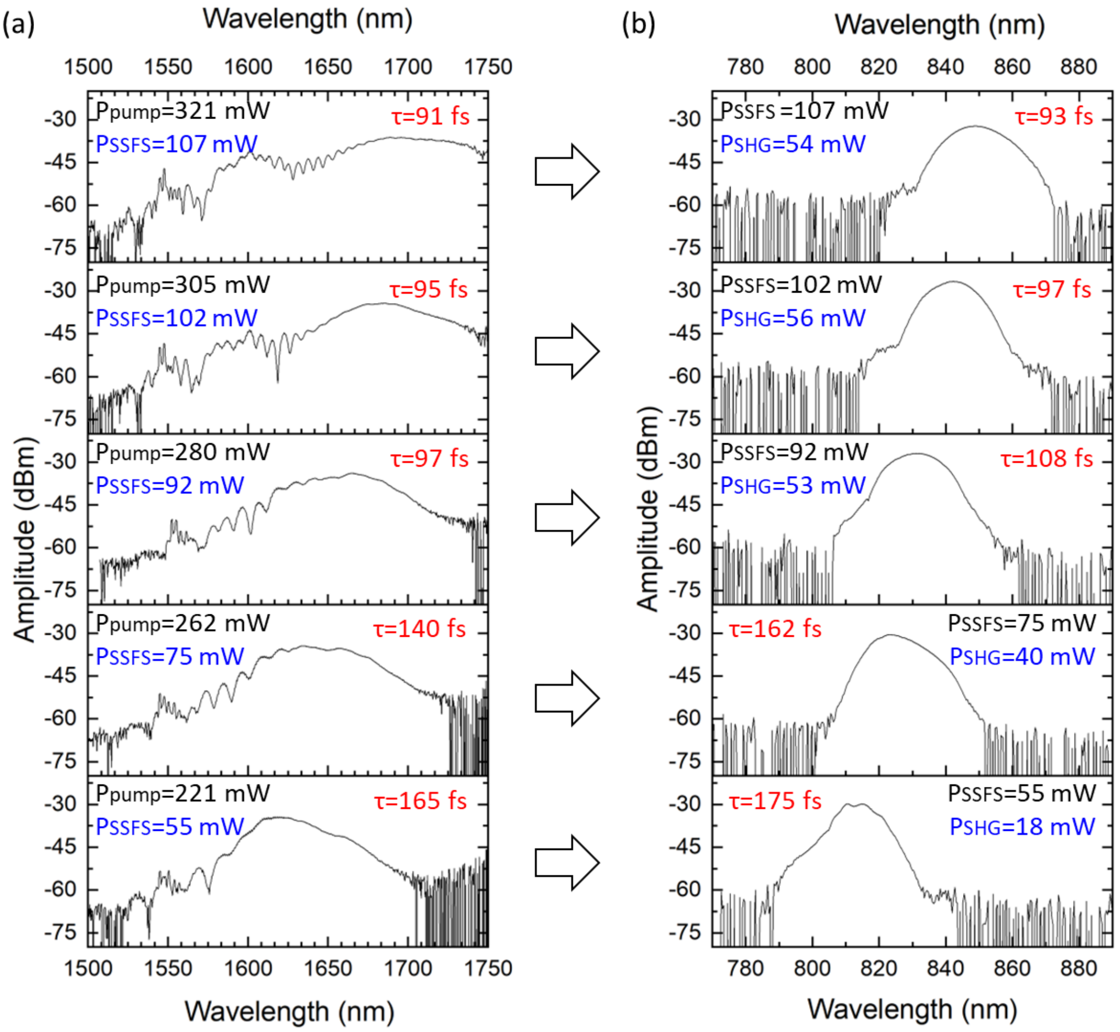

Figure 5.11. Optical spectra after (a) the SSFS stage and (b) the corresponding SHG stage with the indication of pulse duration, pump, and output power.

Notably, with anomalous dispersion, the SSFS effect is more significant for the shortest solitons, expanding the pulse spectrum to the red side. The increase in pump power influences the SSFS, causing a gradual reduction of the pulse duration and shifting towards longer wavelengths. Increasing the pump power to 321 mW, the central wavelength is shifted to 1700 nm, accompanied by an average output power of 107 mW, while the pulse duration reduces to 91 fs. The relationship between the laser pulse duration, the output power, and the operating wavelength in the SSFS stage is shown in Figure 5.12.

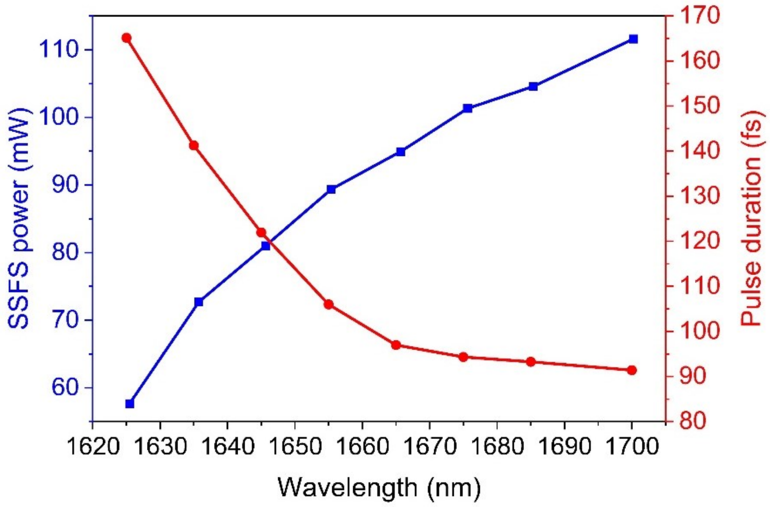

Figure 5.12. Relation between soliton central wavelength, soliton duration and output power in the SSFS stage.

5.3.5 Second Harmonic Generation Stage

The final stage of the laser is the second harmonic generation. SHG is a nonlinear phenomenon of frequency doubling, which occurs when two incident light photons pass through an optical medium with second-order nonlinearity, combine their energy, and generate a new photon with double frequency [248]. This process can be used in materials where the refractive index changes as the light propagates at different frequencies.

If a crystal has no constant phase matching between the incoming and generated photons, they can destructively interfere with each other, limiting the number of output photons as shown in Figure 5.13 (a).

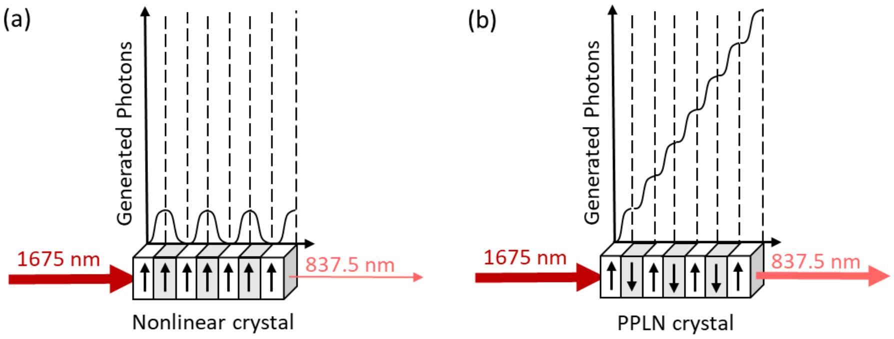

Figure 5.13. Second harmonic generation in (a) no phase matching nonlinear crystal, (b) quasi-phase matching PPLN crystal.

To address this issue, phase matching is achieved in a periodically poled lithium niobate crystal, an engineered quasi-phase-matched material [249], [250]. This crystal features periodic poles with opposite electric dipole moments. When incident photons pass through these poles, they generate new photons with a 180º phase shift. This arrangement ensures a consistent phase match between the incident and generated photons. By selecting an appropriate poling period for the crystal, tailored to a specific wavelength, it becomes possible to maximise the production of non-interfering generated photons, thereby optimising the efficiency of the nonlinear second harmonic generation process (Fig. 5.13 (b)).

This stage includes free-space optical elements such as collimation lenses, a long-pass filter, quarter- and half-wave plates, PPLN crystal, and dichroic mirrors. A schematic diagram of the SHG stage is illustrated in Figure 5.9 (SHG stage section).

The filter operates by selectively attenuating the intensity of wavelengths below 1600 nm. In combination, the QWP and HWP transform elliptical polarisation into linear polarisation and adjust its orientation, aligning the polarisation axis of the incident light with the dipole moment of the PPLN crystal. This alignment is crucial for effectively using the nonlinear characteristics of the PPLN crystal.

The main element in the frequency doubling stage is the PPLN crystal that uses the second-order nonlinear effect to efficiently double the frequency of incident light. The crystal's periodic poling structure, with alternating regions of opposite polarisation, creates the phase-matching condition necessary for the conversion of two photons from the fundamental frequency into one photon at double frequency.

The 0.3 mm long PPLN crystal with a poling period of 20.6-23.3 μm is designed to efficiently convert a fundamental wavelength of 1700 nm to second harmonic generation, resulting in a wavelength of 850 nm. The optical spectra of the fundamental frequency with a central wavelength from 1625 nm to 1700 nm and the corresponding spectra of SHG (812-850 nm) are shown in Figure 5.11 (a) and (b), respectively.

The developed SHG stage enables the generation of sub-180 femtosecond pulses within the wavelength range of 812-850 nm and an average output power of 18-56 mW, respectively. The relation between pulse duration, wavelength, and output power of the SHG stage is shown in Figure 5.14.

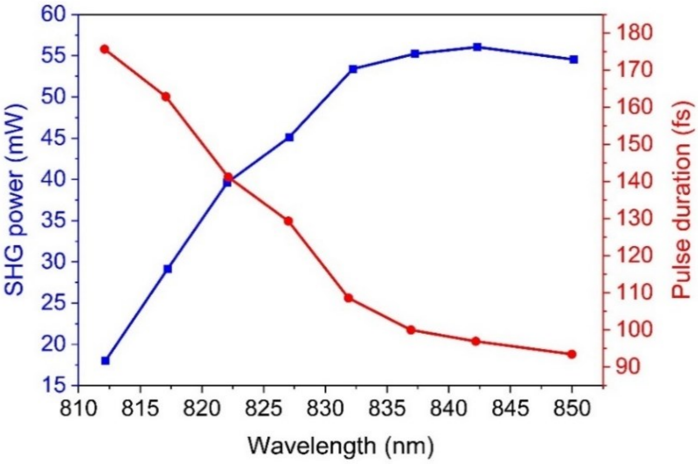

Figure 5.14. Relation between soliton central wavelength, soliton duration and output power in the SHG stage.

The developed system, operating at the wavelength of 835 nm, was tested on the pulse stability for 5 hours. Figure 5.15 demonstrates the long-term stability of the femtosecond generation with an output power of 50.3±1.0 mW.

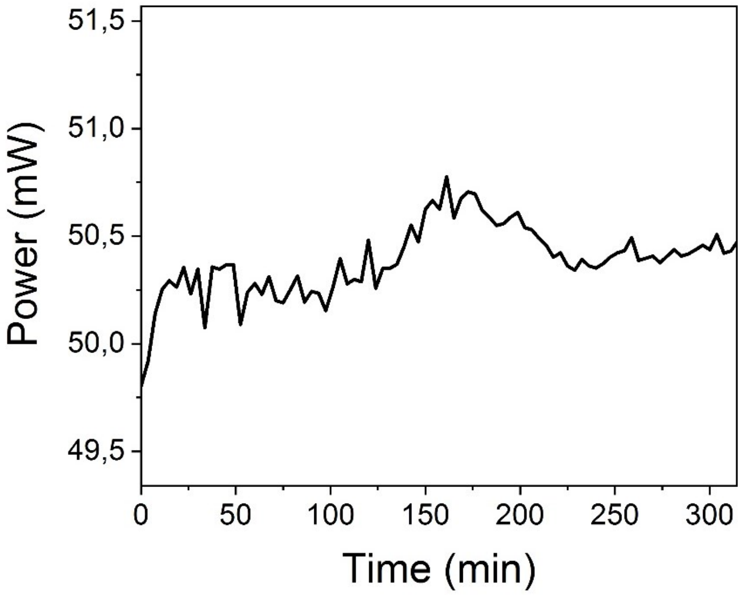

Figure 5.15. Time-dependence of the output power of the developed laser operating at 835 nm wavelength.

The laser system operates within the first and third biological windows with a repetition rate of 10.94 MHz and an average power of up to 56 mW (at 845 nm) and up to 107 mW (at 1700 nm).

5.4 Conclusion

The developed fibre laser system demonstrates a stable sub-170 fs pulse generation with an average power of 107 mW within the third biological window. The use of a soliton self-frequency shift technique provides a spectral tuning range from 1625 nm to 1700 nm with a pulse energy of up to 10 nJ at a repetition rate of 10.94 MHz.

Moreover, the use of a PPLN crystal in the process of second harmonic generation has exhibited a conversion efficiency of 54% and achieved an output power of up to 56 mW. The laser system, operating in the spectral tunability range of 815-850 nm, has a pulse duration of less than 180 fs.

These advances pave the way for advanced cancer diagnostics based on multimodal imaging, where the developed laser system plays a crucial role. This laser system offers the necessary 1700 nm and 850 nm wavelengths for the biomedical applications in the third and first tissue transparency windows, respectively.

An accurate and comprehensive multiphoton imaging technique of fluorophores requires a peak power density level of MW/cm^2 [251]-[253], which can be achieved by focusing the laser beam into a spot with a diameter of 0.26 mm, assuming that the average power of the developed laser is 0.5 mW, a pulse repetition rate is 10.94 MHz, and a pulse duration of 170 fs.

However, the exposure time should be no more than a few seconds to avoid fluorophore bleaching. This condition is driven by an estimated dose that can be delivered to the sample in 5 s (9.4 J/cm^2) since the bleaching threshold of most fluorophores is in the dose range of 18-200 J/cm^2. For example, eGFP experiences photobleaching at a dose of 200 J/cm^2 when irradiated by a 488 nm light [254], while cyanine dye loses 50% of the fluorescence emission intensity under a dose of 135 J/cm^2 which was observed after 30 minutes of irradiation by 661 nm light with a power density of 75 mW/cm^2 [255]. According to D. Vivo *et al.* [256], collagen can experience fluorescence photobleaching by 30% when irradiated for 6 minutes with a 532 nm laser with a pulse energy of 15 mJ (dose of 18 J/cm^2). However, since scanning multiphoton images typically takes microseconds or milliseconds per pixel, such laser irradiation does not cause bleaching of the fluorophore [257].

The femtosecond fibre laser has several advantages over traditional crystal-based solid-state lasers. Its compactness and light weight make it a promising lighting system for various biological and medical applications where space and weight constraints are essential. The system's environmental robustness, cost-effectiveness, and ease of triggering mode-locking without complex element adjustment make it the most attractive laser source operating at 1700 nm. This makes it very suitable for mass production and integration into optical instruments for hospital applications, for example, for detecting early-stage bladder cancer.

The laser source exhibits exceptional stability and performance, consistently generating stable femtosecond pulses for a prolonged duration of at least 5 hours. These remarkable achievements confirm its suitability for clinical applications in the field of early diagnosis of cancer.

Chapter 6

Overall Discussion, Conclusions and Future Works

6.1 Discussion and Conclusions

Laser methods and technologies are widely used in biomedical research, clinical diagnostics, and therapy. Its versatile application extends to various fields, including medical research, dentistry, dermatology, angiology, ophthalmology, neuroscience, and oncology.

This thesis presents the studies of complex dynamics of light-tissue interactions and the optical characteristics of light-sensitive proteins suitable for use as optogenetic tools and biomarkers. In addition, the work includes the development of laser systems designed to facilitate biological research, neuronal stimulation, and cancer diagnostics.

The design of laser systems and photonic instruments highly depends on the specific requirements of biomedical applications. Many issues need to be addressed before the practical development of optical sources for diagnostic or therapeutic instruments. That includes the determination of the optimal operating wavelength, laser modes and output parameters; the impact of the laser on biological tissues and surrounding areas, considering how it can be changed with various exposure times. Moreover, the laser source should be designed with the understanding that the end user is a medical specialist with average knowledge in optics and photonics working in the biological laboratory or clinics. Therefore, the system should be user-friendly and stable under environmental conditions such as temperature, humidity, and vibration fluctuations. It is necessary to evaluate the convenience of the design and physical dimensions of the laser system and the need to replace and adjust optical elements. These critical considerations form the basis for developing laser systems for biomedical applications.

Before developing the compact laser sources for neurostimulation, detailed studies of light interaction with post-mortem mouse head tissues were performed. The spectrophotometry technique was used to measure transmittance and diffuse reflectance spectra of mouse skin, skull, and brain samples and to discover their light propagation coefficients for the following computer modelling. The simulated penetration depths of all studied samples reached the maximum values in the second tissue transparency window. There are 3.7 mm, 3.8 mm, and 1.9 mm for the mouse skin, skull, and brain, respectively.

A NIR-II optical system with aligned CW and pulsed laser beams was developed to experimentally compare the propagation of continuous-wave light and femtosecond pulses through biological tissues. This study showed that laser irradiation in the femtosecond pulsed mode exhibited better propagation through the brain and skull, showing improvements of 1.5% and 4% compared with the CW mode. In the wavelength range 1080-1180 nm, the pulse transmittance through single-layer skin, skull and brain pulses reaches 47%, 59% and 21%, while in the case of a two-layer skin-skull system, the maximum value is 12%. Therefore, 12% of the original laser irradiation can pass through the 1 mm tissues, reaching a brain cortex non-invasively. The three-layer system, consisting of 0.5 mm thick skin, 0.5 mm thick skull, and 1.5 mm thick brain, transmits 2-3% of incident pulsed radiation due to high light absorption by water, haemoglobin and scattering in collagen components. The application of clearing techniques can enhance the light transmittance of tissues and can be used for non- or minimally invasive methods for biomedical diagnostics and treatments [29].

The study outcomes were implemented into developing a compact laser system for neurostimulation. Optogenetic activation of neuronal cells can be achieved through the delivery and expression of light-sensitive proteins such as opsins and phytochromes. Modern optogenetic methods provide remarkable results in the precise activation of specific neurons [258]. However, these methods require surgical procedures including the insertion of a cannula and an optical fibre into the brain to deliver light to light-sensitive proteins distributed among neurons. To improve this approach and reduce the need for surgical intervention, an optical system based on the NIR-II ultrashort laser can be used. The shift of light wavelength from the visible to the second tissue transparency window can increase the penetration depth and deliver the required light energy through the skin and skull to the brain cortex. One of the main goals of this study was to explore the nonlinear properties of photosensitive proteins at the NIR-II wavelength range to develop a non/minimally invasive tool for optogenetics.

In this work, two experimental systems based on a Ti:Sa laser were developed to study the optical properties of light-sensitive proteins. One of the systems was designed for two-photon activation, while another was created to examine two-photon fluorescence characteristics of photosensitive proteins. For genetically engineered truncated *Deinococcus radiodurans* bacterial phytochromes, two-photon Pr→Pfr conversion was successfully achieved in the wavelength range of 1180-1360 nm. The dimeric sample showed the highest conversion efficiency at 1280 nm (53%), while the monomeric sample displayed the best result of two-photon conversion to the Pfr yield under 1250 nm laser irradiation (62%). The efficiency was increased to 55% and 72% by applying a high peak power of 301 mJ/cm^2 and 339 mJ/cm^2 for dimer and monomer samples, respectively.

Moreover, both samples exhibited two-photon fluorescence at 720 nm, excited by a near-infrared laser operating at 810 nm. Notably, the fluorescence emission grows significantly under higher temperature conditions. Increasing the solution temperature from 19°C to 37°C improved the emission yield by 40% and 81% for dimeric and monomeric phytochromes, respectively. This outcome implies that delivering these phytochromes to the animal or human brain cortex with a 36-38°C temperature will enhance two-photon fluorescence emission. Consequently, these phytochrome samples can be used as biomarkers and optogenetic tools to monitor their proper expression among neurons and modulate brain functionality through two-photon conversion.

The outcomes, demonstrating the required peak power level for two-photon conversions, were used to define the essential parameters of a compact laser system designed for *in vivo* neurostimulation.

The need for a compact size limited the available laser options operating at NIR-II wavelengths and excluded crystal-based solid-state lasers from the list of possible laser solutions. Since semiconductor lasers are sensitive to the potential temperature fluctuations that can occur in biomedical or clinical laboratories, a fibre laser was selected as a compact laser source.

The main challenge in developing a fibre laser operating in the NIR-II wavelength range is the inability of conventional doped fibres to emit light in this wavelength range. To overcome this obstacle, a Yb-doped fibre laser system was developed using Yb-DCF, which effectively shifted the operating wavelength from 1064 nm to 1170 nm. A requirement of high peak power of 82 kW was achieved by reducing the pulse repetition rate from 9.1 MHz to 608 kHz using a pulse picker and increasing an average power to 250 mW by a system of Yb-doped fibre amplifiers.

The compact dimensions of the laser system (34x46x46 cm) make it suitable for use in biological laboratories and medical institutions. As part of future work, the study of non-invasive or minimally invasive *in vivo* optogenetics should be conducted using the developed versatile compact fibre laser system.

The thesis also includes the development of a laser source operating in the NIR-I and NIR-III wavelength ranges, which can potentially be used in a multimodal cancer detector. The compact laser source was developed using an Er-doped fibre laser and EDFAs. However, since Er ions emit light at a wavelength of 1550 nm, the desired operating wavelength required moving to longer wavelengths (1600-1700 nm). This shift was achieved by introducing a PCF LMA fibre in which the nonlinear SSFS effect was induced by high light intensity (≥30 kW).

The developed femtosecond laser can operate over a wide range of wavelengths from 1625 nm to 1700 nm, providing an output power of up to 107 mW at a repetition rate of 10.94 MHz. The NIR-III range, with its significant depth of tissue penetration, can be used for morphological imaging of tissues, exciting three-photon fluorescence of fluorophores such as collagen, porphyrin, elastin, and others [190]. While the frequency doubling of the 1625-1700 nm in the PPLN crystal generates sub-180 fs pulses at wavelength range of 812–850 nm. These wavelengths are within the NIR-I range and can be used for autofluorescence imaging of metabolic biomarkers. The system operating in the combined NIR-I and NIR-III spectral regions can be implemented as a laser source for the multimodal imaging tool. Potentially, the integration of these laser beams into an endoscopic system can be used to detect early-stage bladder cancer.

These studies demonstrate a comprehensive analysis of light-tissue interaction and the development of lasers for biological research, non- or minimally invasive optogenetics and cancer detection, promising significant improvement of the modern optical methods and techniques in biomedicine.

6.2 Future Works

Research on light tissue interactions, as described in this thesis, has been limited to the study of post-mortem mouse head tissues. The extension of this study to *in vivo* samples, incorporating the complexities introduced by blood circulation and the brain activities, can offer invaluable insights into the dynamics of light propagation within living biological tissues.

Understanding the penetration depth of light, especially concerning polarisation, becomes a crucial determinant in various scientific and medical applications. In neuroscience, for instance, the interaction of polarised light with the brain cells can provide vital information about neural activity and connectivity. This knowledge could potentially enhance the understanding and detection of neurological diseases such as Alzheimer's [56] and contribute to developing novel diagnostic and therapeutic approaches.

Furthermore, in medical imaging, particularly in techniques such as optical coherence tomography and diffuse optical imaging, a comprehensive understanding of light-tissue interaction can significantly improve the accuracy and resolution of imaging methods. This has implications for early disease detection, treatment monitoring, and the overall advancement of medical diagnostics.

The translational applicability of the study's findings to human subjects, with a meticulous examination of how light interacts with human skin, skull, and brain tissues, is pivotal for integrating these insights into clinical practice.

Similar problems exist in optogenetic studies because modern experiments for activating neuronal cells were implemented only on rodents [81]-[84]. Although optogenetics has made significant advances in these models, transferring it to larger, more complex brain structures remains challenging. Future studies should explore and adapt optogenetic methods in larger animal models, including non-human primates, to cover the gap between preclinical studies and potential clinical applications.

Moreover, a primary goal to improve optogenetics is to selectively target individual cell types in complex neural networks which often involve viral vectors to deliver genes. This may raise concerns regarding long-term biocompatibility and potential immune responses. Future research should focus on developing enhanced genetic targeting strategies and new optogenetic actuators to enable precise and exclusive modulation of desired neuronal populations, avoiding adverse effects on healthy neighbouring cells.

The investigation of the optical properties of phytochrome presented in this thesis holds promising potential to contribute significantly to developing new tools and strategies for further investigations in the optogenetic field.

At the same time, the developed laser systems for optogenetic study and multimodal cancer diagnostics are prospective to advance current research and overcome challenges related to the compactness of sources, reliable cost, and laser output stabilities. The laser sources have been designed considering the requirements of the fields and the safety of studied tissues and fluorescent proteins.

In future work, implementing the developed laser systems for *in vivo* studies can help enhance existing knowledge, develop more accurate diagnostic and therapeutic techniques, and improve the translational applicability of findings for clinical use.

Bibliography

[1] G. Keiser, *Biophotonics*. Springer, 2016.

[2] M. J. Weber, *Handbook of laser wavelengths*. CRC press, 2018.

[3] A. T. Gursel, ‘Fiber lasers and their medical applications’, *Optical Amplifiers—A Few Different Dimensions*, p. 13, 2018.

[4] B. L. Diffey, ‘Sources and measurement of ultraviolet radiation’, *Methods*, vol. 28, no. 1, pp. 4–13, 2002.

[5] D. Basting and G. Marowsky, ‘Excimer laser technology’, 2005.

[6] A. M. Luke, S. Mathew, M. M. Altawash, and B. M. Madan, ‘Lasers: A review with their applications in oral medicine’, *J Lasers Med Sci*, vol. 10, no. 4, p. 324, 2019.

[7] C. Chudoba *et al.*, ‘All-solid-state Cr: forsterite laser generating 14-fs pulses at 1.3 μm’, *Opt Lett*, vol. 26, no. 5, pp. 292–294, 2001.

[8] J. Šulc and H. Jelínková, ‘Solid-state lasers for medical applications’, in *Lasers for medical applications*, Elsevier, 2013, pp. 127–176.

[9] C. Jauregui, J. Limpert, and A. Tünnermann, ‘High-power fibre lasers’, *Nat Photonics*, vol. 7, no. 11, pp. 861–867, 2013.

[10] M. R. Hofmann and S. W. Koch, ‘Semiconductor Lasers’, in *Springer Handbook of Semiconductor Devices*, Springer, 2022, pp. 851–864.

[11] M.-C. Amann, ‘Semiconductor light sources’, in *Optical Properties of Semiconductors*, Springer, 1993, pp. 291–320.

[12] H. Jelínková, *Lasers for medical applications: diagnostics, therapy and surgery*. Elsevier, 2013.

[13] Z. Darzynkiewicz, E. Holden, W. Telford, and D. Wlodkowic, ‘Recent Advances in Cytometry, Part B: Advances in Applications’, 2011.

[14] Y.-M. Moon, H.-C. Kim, K.-S. Bae, S.-H. Baek, W.-J. Shon, and W. Lee, ‘Effect of laser-activated irrigation of 1320-nanometer Nd: YAG laser on sealer penetration in curved root canals’, *J Endod*, vol. 38, no. 4, pp. 531–535, 2012.

[15] D. J. Goldberg, ‘Benign pigmented lesions of the skin: Treatment with the Q-switched ruby laser’, *J Dermatol Surg Oncol*, vol. 19, no. 4, pp. 376–379, 1993.

[16] B. Finkel, Y. D. Eliezri, A. Waldman, and M. Slatkine, ‘Pulsed alexandrite laser technology for noninvasive hair removal’, *J Clin Laser Med Surg*, vol. 15, no. 5, pp. 225–229, 1997.

[17] N. Saedi, A. Metelitsa, K. Petrell, K. A. Arndt, and J. S. Dover, ‘Treatment of tattoos with a picosecond alexandrite laser: a prospective trial’, *Arch Dermatol*, vol. 148, no. 12, pp. 1360–1363, 2012.

[18] V. Andresen, S. Alexander, W.-M. Heupel, M. Hirschberg, R. M. Hoffman, and P. Friedl, ‘Infrared multiphoton microscopy: subcellular-resolved deep tissue imaging’, *Curr Opin Biotechnol*, vol. 20, no. 1, pp. 54–62, 2009.

[19] C. M. Philipp, E. Rohde, and H. Berlien, ‘Nd: YAG laser procedures in tumor treatment’, in *Seminars in surgical oncology*, Wiley Online Library, 1995, pp. 290–298.

[20] M. Kreisler, H. Götz, H. Duschner, and B. d’Hoedt, ‘Effect of Nd: YAG, Ho: YAG, Er: YAG, CO 2, and GaAlAs Laser Irradiation on Surface Properties of Endosseous Dental Implants.’, *International Journal of Oral & Maxillofacial Implants*, vol. 17, no. 2, 2002.

[21] V. V Tuchin, ‘Light-tissue interactions’, *Biomedical Photonics Handbook*, pp. 1–3, 2003.

[22] V. V Tuchin, ‘Tissue optics and photonics: biological tissue structures’, *J Biomed Photonics Eng*, vol. 1, no. 1, pp. 3–21, 2015.

[23] J. F. Algorri, M. Ochoa, P. Roldán-Varona, L. Rodríguez-Cobo, and J. M. López-Higuera, ‘Light technology for efficient and effective photodynamic therapy: A critical review’, *Cancers (Basel)*, vol. 13, no. 14, p. 3484, 2021.

[24] E. Hemmer, A. Benayas, F. Légaré, and F. Vetrone, ‘Exploiting the biological windows: current perspectives on fluorescent bioprobes emitting above 1000 nm’, *Nanoscale Horiz.*, vol. 1, no. 3, pp. 168–184, 2016, doi: 10.1039/C5NH00073D.

[25] S. Golovynskyi *et al.*, ‘Optical windows for head tissues in near-infrared and short-wave infrared regions: Approaching transcranial light applications’, *J Biophotonics*, vol. 11, no. 12, p. e201800141, 2018, doi: https://doi.org/10.1002/jbio.201800141.

[26] S. G. Sokolovski *et al.*, ‘Two-photon conversion of a bacterial phytochrome.’, *Biophys J*, vol. 120, no. 5, pp. 964–974, Mar. 2021, doi: 10.1016/j.bpj.2021.01.028.

[27] M. S. Ozturk, M. G. Montero, L. Wang, L. M. Chaible, M. Jechlinger, and R. Prevedel, ‘Intravital mesoscopic fluorescence molecular tomography allows non-invasive in vivo monitoring and quantification of breast cancer growth dynamics.’, *Commun Biol*, vol. 4, no. 1, p. 556, May 2021, doi: 10.1038/s42003-021-02063-8.

[28] S. Haleh, G. Hirac, and P. Frédéric, ‘Optical properties of mice skull bone in the 455- to 705-nm range.’, *J Biomed Opt*, vol. 22, no. 1, p. 10503, Jan. 2017, doi: 10.1117/1.JBO.22.1.010503.

[29] M. S. Cano-Velázquez *et al.*, ‘Enhanced near infrared optical access to the brain with a transparent cranial implant and scalp optical clearing.’, *Biomed Opt Express*, vol. 10, no. 7, pp. 3369–3379, Jul. 2019, doi: 10.1364/BOE.10.003369.

[30] M. Wang, C. Wu, D. Sinefeld, B. Li, F. Xia, and C. Xu, ‘Comparing the effective attenuation lengths for long wavelength in vivo imaging of the mouse brain’, *Biomed. Opt. Express*, vol. 9, no. 8, pp. 3534–3543, Aug. 2018, doi: 10.1364/BOE.9.003534.

[31] M. Mesradi *et al.*, ‘Experimental and analytical comparative study of optical coefficient of fresh and frozen rat tissues.’, *J Biomed Opt*, vol. 18, no. 11, p. 117010, Nov. 2013, doi: 10.1117/1.JBO.18.11.117010.

[32] E. A. Genina *et al.*, ‘Optical properties of brain tissues at the different stages of glioma development in rats: pilot study’, *Biomed. Opt. Express*, vol. 10, no. 10, pp. 5182–5197, Oct. 2019, doi: 10.1364/BOE.10.005182.

[33] D. Han *et al.*, ‘Penetrating effect of high-intensity infrared laser pulses through body tissue’, *RSC Adv*, vol. 8, no. 56, pp. 32344–32357, Sep. 2018, doi: 10.1039/c8ra05285a.

[34] J. T. Hashmi *et al.*, ‘Effect of pulsing in low-level light therapy’, *Lasers Surg Med*, vol. 42, no. 6, pp. 450–466, Aug. 2010, doi: 10.1002/lsm.20950.

[35] J. Huang, S. Xia, Y. Chen, X. Li, K. Wang, and Y. Rui, ‘Experimental study of thermal damage to in vitro skin tissue welding by femtosecond laser’, *Infrared Phys Technol*, vol. 129, p. 104536, 2023, doi: https://doi.org/10.1016/j.infrared.2022.104536.

[36] T. Ando *et al.*, ‘Comparison of therapeutic effects between pulsed and continuous wave 810-nm wavelength laser irradiation for traumatic brain injury in mice.’, *PLoS One*, vol. 6, no. 10, p. e26212, 2011, doi: 10.1371/journal.pone.0026212.

[37] P. Brondon, I. Stadler, and R. J. Lanzafame, ‘Pulsing influences photoradiation outcomes in cell culture.’, *Lasers Surg Med*, vol. 41, no. 3, pp. 222–226, Mar. 2009, doi: 10.1002/lsm.20740.

[38] B. S. Sushko, I. P. Lymans’kyĭ, and S. O. Huliar, ‘Action of the red and infrared electromagnetic waves of light-emitting diodes on the behavioral manifestation of somatic pain.’, *Fiziol Zh*, vol. 53, no. 3, pp. 51–60, 2007.

[39] P. A. Lapchak and L. De Taboada, ‘Transcranial near infrared laser treatment (NILT) increases cortical adenosine-5’-triphosphate (ATP) content following embolic strokes in rabbits.’, *Brain Res*, vol. 1306, pp. 100–105, Jan. 2010, doi: 10.1016/j.brainres.2009.10.022.

[40] P. A. Lapchak, K. F. Salgado, C. H. Chao, and J. A. Zivin, ‘Transcranial near-infrared light therapy improves motor function following embolic strokes in rabbits: an extended therapeutic window study using continuous and pulse frequency delivery modes.’, *Neuroscience*, vol. 148, no. 4, pp. 907–914, Sep. 2007, doi: 10.1016/j.neuroscience.2007.07.002.

[41] J. Kymplová, L. Navrátil, and J. Knízek, ‘Contribution of phototherapy to the treatment of episiotomies.’, *J Clin Laser Med Surg*, vol. 21, no. 1, pp. 35–39, Feb. 2003, doi: 10.1089/10445470360516725.

[42] Y. Ueda and N. Shimizu, ‘Effects of pulse frequency of low-level laser therapy (LLLT) on bone nodule formation in rat calvarial cells.’, *J Clin Laser Med Surg*, vol. 21, no. 5, pp. 271–277, Oct. 2003, doi: 10.1089/104454703322564479.

[43] F. A. H. Al-Watban and X. Y. Zhang, ‘The comparison of effects between pulsed and CW lasers on wound healing.’, *J Clin Laser Med Surg*, vol. 22, no. 1, pp. 15–18, Feb. 2004, doi: 10.1089/104454704773660921.

[44] D. Gigo-Benato *et al.*, ‘Low-power laser biostimulation enhances nerve repair after end-to-side neurorrhaphy: a double-blind randomized study in the rat median nerve model.’, *Lasers Med Sci*, vol. 19, no. 1, pp. 57–65, 2004, doi: 10.1007/s10103-004-0300-3.

[45] B. Braverman, R. J. McCarthy, A. D. Ivankovich, D. E. Forde, M. Overfield, and M. S. Bapna, ‘Effect of helium-neon and infrared laser irradiation on wound healing in rabbits.’, *Lasers Surg Med*, vol. 9, no. 1, pp. 50–58, 1989, doi: 10.1002/lsm.1900090111.

[46] R. I. Barbosa, E. C. de O. Guirro, L. Bachmann, H. E. Brandino, and R. R. de J. Guirro, ‘Analysis of low-level laser transmission at wavelengths 660, 830 and 904 nm in biological tissue samples’, *J Photochem Photobiol B*, vol. 209, p. 111914, 2020, doi: https://doi.org/10.1016/j.jphotobiol.2020.111914.

[47] A. Barbora, O. Bohar, A. A. Sivan, E. Magory, A. Nause, and R. Minnes, ‘Higher pulse frequency of near-infrared laser irradiation increases penetration depth for novel biomedical applications’, *PLoS One*, vol. 16, no. 1, pp. 1–11, 2021, doi: 10.1371/journal.pone.0245350.

[48] D. Manahan-Vaughan, ‘Chapter 3 - Special Considerations When Using Mice for In Vivo Electrophysiology and Long-Term Studies of Hippocampal Synaptic Plasticity During Behavior’, in *Handbook of Neural Plasticity Techniques*, vol. 28, D. B. T.-H. of B. N. Manahan-Vaughan, Ed., Elsevier, 2018, pp. 63–84. doi: https://doi.org/10.1016/B978-0-12-812028-6.00003-3.

[49] P. W. Milonni and J. H. Eberly, *Laser physics*. John Wiley & Sons, 2010.

[50] E. Dervieux, Q. Bodinier, W. Uhring, and M. Théron, ‘Measuring hemoglobin spectra: searching for carbamino-hemoglobin’, *J Biomed Opt*, vol. 25, no. 10, p. 105001, 2020, doi: 10.1117/1.JBO.25.10.105001.

[51] L. Sordillo *et al.*, ‘Third therapeutic spectral window for deep tissue imaging’, *Proceedings of SPIE - The International Society for Optical Engineering*, vol. 8940, Mar. 2014, doi: 10.1117/12.2040604.

[52] S. A. Prahl, ‘The adding-doubling method’, in *Optical-thermal response of laser-irradiated tissue*, Springer, 1995, pp. 101–129.

[53] S. A. Prahl, M. J. C. van Gemert, and A. J. Welch, ‘Determining the optical properties of turbid media by using the adding--doubling method’, *Appl. Opt.*, vol. 32, no. 4, pp. 559–568, Feb. 1993, doi: 10.1364/AO.32.000559.

[54] B. D. Bunday, *Basic optimisation methods*. 1984.

[55] S. R. Arridge, ‘Optical tomography in medical imaging’, *Inverse Probl*, vol. 15, no. 2, p. R41, 1999.

[56] M. Borovkova *et al.*, ‘Evaluating β-amyloidosis progression in Alzheimer’s disease with Mueller polarimetry.’, *Biomed Opt Express*, vol. 11 8, pp. 4509–4519, 2020.

[57] R. J. Rockwell and L. Goldman, *Research on human skin laser damage thresholds*. University of Cincinnati, 1974.

[58] R. Vincelette *et al.*, ‘Porcine skin damage thresholds for 0.6 to 9.5 cm beam diameters from 1070-nm continuous-wave infrared laser radiation’, *J Biomed Opt*, vol. 19, no. 3, p. 35007, 2014.

[59] C. P. Cain *et al.*, ‘Infrared laser damage thresholds for skin at wavelengths from 0.810 to 1.54 microns for femtosecond to microsecond pulse durations’, in *Optical Interactions with Tissue and Cells XVIII*, SPIE, 2007, pp. 222–233.

[60] J. W. Oliver *et al.*, ‘Infrared skin damage thresholds from 1319-nm continuous-wave laser exposures’, *J Biomed Opt*, vol. 18, no. 12, p. 125002, 2013.

[61] L. Jiao, J. Wang, Y. Fan, and Z. Yang, ‘Porcine skin damage thresholds and histological damage characteristics from 1319-nm laser radiation’, *J Biomed Opt*, vol. 24, no. 9, p. 95003, 2019.

[62] E. Ortega, D. Nicholls, N. D. Browning, and N. de Jonge, ‘High temporal-resolution scanning transmission electron microscopy using sparse-serpentine scan pathways’, *Sci Rep*, vol. 11, no. 1, p. 22722, 2021.

[63] A. S. Stender *et al.*, ‘Single cell optical imaging and spectroscopy’, *Chem Rev*, vol. 113, no. 4, pp. 2469–2527, 2013.

[64] World Health Organization, *Neurological disorders: public health challenges*. World Health Organization, 2006.

[65] World Health Organization, ‘WHO Epilepsy Fact Sheet’. [Online]. Available: https://www.who.int/news-room/fact-sheets/detail/epilepsy

[66] Parkinson’s Foundation, ‘Statistics’. [Online]. Available: https://www.parkinson.org/understanding-parkinsons/statistics

[67] Pan American Health Organization, ‘The burden of Neurological conditions in the Region of the Americas, 2000-2019’. [Online]. Available: https://www.paho.org/en/enlace/burden-neurological-conditions

[68] U. N. D. of Economic and P. D. Social Affairs, ‘World population prospects 2022: Summary of results’. United Nations New York, NY, USA, 2022.

[69] C. L. S. Marques, M. H. Borgato, E. de Moura, R. Bazan, and G. J. Luvizutto, ‘Physical therapy in patients with Alzheimer’s disease: a systematic review of randomized controlled clinical trials’, *Fisioterapia e Pesquisa*, vol. 26, pp. 311–321, 2019.

[70] M. L. Cera, K. Z. Ortiz, P. H. F. Bertolucci, and T. S. C. Minett, ‘Speech and orofacial apraxias in Alzheimer’s disease’, *Int Psychogeriatr*, vol. 25, no. 10, pp. 1679–1685, 2013.

[71] E. Welsby, S. Berrigan, and K. Laver, ‘Effectiveness of occupational therapy intervention for people with Parkinson’s disease: systematic review’, *Aust Occup Ther J*, vol. 66, no. 6, pp. 731–738, 2019.

[72] C. O. Oluigbo, A. Salma, and A. R. Rezai, ‘Deep brain stimulation for neurological disorders’, *IEEE Rev Biomed Eng*, vol. 5, pp. 88–99, 2012.

[73] D. M. Patel, H. C. Walker, R. Brooks, N. Omar, B. Ditty, and B. L. Guthrie, ‘Adverse events associated with deep brain stimulation for movement disorders: analysis of 510 consecutive cases’, *Operative Neurosurgery*, vol. 11, no. 1, pp. 190–199, 2015.

[74] S. Z. K. Tan, M.-L. Fung, J. Koh, Y.-S. Chan, and L. W. Lim, ‘The Paradoxical Effect of Deep Brain Stimulation on Memory.’, *Aging Dis*, vol. 11, no. 1, pp. 179–190, Feb. 2020, doi: 10.14336/AD.2019.0511.

[75] K. Appasani, *Optogenetics: From neuronal function to mapping and disease biology*. Cambridge University Press, 2017.

[76] O. Yizhar, L. E. Fenno, T. J. Davidson, M. Mogri, and K. Deisseroth, ‘Optogenetics in neural systems.’, *Neuron*, vol. 71, no. 1, pp. 9–34, Jul. 2011, doi: 10.1016/j.neuron.2011.06.004.

[77] A. Terakita and T. Nagata, ‘Functional properties of opsins and their contribution to light-sensing physiology’, *Zoolog Sci*, vol. 31, no. 10, pp. 653–659, 2014.

[78] P. Mahmoudi, H. Veladi, and F. G. Pakdel, ‘Optogenetics, tools and applications in neurobiology’, *J Med Signals Sens*, vol. 7, no. 2, p. 71, 2017.

[79] K. Lehtinen, M. S. Nokia, and H. Takala, ‘Red light optogenetics in neuroscience’, *Front Cell Neurosci*, vol. 15, p. 778900, 2022.

[80] K. M. Tye and K. Deisseroth, ‘Optogenetic investigation of neural circuits underlying brain disease in animal models’, *Nat Rev Neurosci*, vol. 13, no. 4, pp. 251–266, 2012, doi: 10.1038/nrn3171.

[81] A. Z. Snyder and A. Q. Bauer, ‘Mapping Structure-Function Relationships in the Brain.’, *Biol Psychiatry Cogn Neurosci Neuroimaging*, vol. 4, no. 6, pp. 510–521, Jun. 2019, doi: 10.1016/j.bpsc.2018.10.005.

[82] I. Goshen, ‘The optogenetic revolution in memory research’, *Trends Neurosci*, vol. 37, no. 9, pp. 511–522, 2014, doi: https://doi.org/10.1016/j.tins.2014.06.002.

[83] C. Lee, A. Lavoie, J. Liu, S. X. Chen, and B.-H. Liu, ‘Light Up the Brain: The Application of Optogenetics in Cell-Type Specific Dissection of Mouse Brain Circuits.’, *Front Neural Circuits*, vol. 14, p. 18, 2020, doi: 10.3389/fncir.2020.00018.

[84] A. Guillaumin, G. Pietro Serra, F. Georges, and Å. Wallén-Mackenzie, ‘Experimental investigation into the role of the subthalamic nucleus (STN) in motor control using optogenetics in mice’, *Brain Res*, vol. 1755, p. 147226, 2021, doi: https://doi.org/10.1016/j.brainres.2020.147226.

[85] V. Gradinaru, M. Mogri, K. R. Thompson, J. M. Henderson, and K. Deisseroth, ‘Optical deconstruction of parkinsonian neural circuitry.’, *Science*, vol. 324, no. 5925, pp. 354–359, Apr. 2009, doi: 10.1126/science.1167093.

[86] C. Yu, I. R. Cassar, J. Sambangi, and W. M. Grill, ‘Frequency-Specific Optogenetic Deep Brain Stimulation of Subthalamic Nucleus Improves Parkinsonian Motor Behaviors’, *Journal of Neuroscience*, vol. 40, no. 22, pp. 4323–4334, 2020, doi: 10.1523/JNEUROSCI.3071-19.2020.

[87] J. N. Bentley, C. Chestek, W. C. Stacey, and P. G. Patil, ‘Optogenetics in epilepsy.’, *Neurosurg Focus*, vol. 34, no. 6, p. E4, Jun. 2013, doi: 10.3171/2013.3.FOCUS1364.

[88] I. Daou *et al.*, ‘Optogenetic Silencing of Nav1.8-Positive Afferents Alleviates Inflammatory and Neuropathic Pain.’, *eNeuro*, vol. 3, no. 1, 2016, doi: 10.1523/ENEURO.0140-15.2016.

[89] M. M. Doroudchi *et al.*, ‘Virally delivered channelrhodopsin-2 safely and effectively restores visual function in multiple mouse models of blindness.’, *Mol Ther*, vol. 19, no. 7, pp. 1220–1229, Jul. 2011, doi: 10.1038/mt.2011.69.

[90] D. Riga, M. R. Matos, A. Glas, A. B. Smit, S. Spijker, and M. C. den Oever, ‘Optogenetic dissection of medial prefrontal cortex circuitry’, *Front Syst Neurosci*, vol. 8, 2014, doi: 10.3389/fnsys.2014.00230.

[91] B. T. Chen *et al.*, ‘Rescuing cocaine-induced prefrontal cortex hypoactivity prevents compulsive cocaine seeking’, *Nature*, vol. 496, no. 7445, pp. 359–362, 2013, doi: 10.1038/nature12024.

[92] M. Prigge *et al.*, ‘Color-tuned Channelrhodopsins for Multiwavelength Optogenetics’, *J Biol Chem*, vol. 287, pp. 31804–31812, 2012, doi: 10.1074/jbc.M112.391185.

[93] A. K. Michael, J. L. Fribourgh, R. N. Van Gelder, and C. L. Partch, ‘Animal Cryptochromes: Divergent Roles in Light Perception, Circadian Timekeeping and Beyond.’, *Photochem Photobiol*, vol. 93, no. 1, pp. 128–140, Jan. 2017, doi: 10.1111/php.12677.

[94] M. E. Auldridge and K. T. Forest, ‘Bacterial phytochromes: More than meets the light’, *Crit Rev Biochem Mol Biol*, vol. 46, no. 1, pp. 67–88, Feb. 2011, doi: 10.3109/10409238.2010.546389.

[95] E. S. Burgie and R. D. Vierstra, ‘Phytochromes: an atomic perspective on photoactivation and signaling’, *Plant Cell*, vol. 26, no. 12, pp. 4568–4583, 2014.

[96] V. V Lychagov, A. A. Shemetov, R. Jimenez, and V. V Verkhusha, ‘Microfluidic System for In-Flow Reversible Photoswitching of Near-Infrared Fluorescent Proteins.’, *Anal Chem*, vol. 88, no. 23, pp. 11821–11829, Dec. 2016, doi: 10.1021/acs.analchem.6b03499.

[97] K. Müller *et al.*, ‘Multi-chromatic control of mammalian gene expression and signaling.’, *Nucleic Acids Res*, vol. 41, no. 12, p. e124, Jul. 2013, doi: 10.1093/nar/gkt340.

[98] G. Salvadori, V. Macaluso, G. Pellicci, L. Cupellini, G. Granucci, and B. Mennucci, ‘Protein control of photochemistry and transient intermediates in phytochromes’, *Nat Commun*, vol. 13, no. 1, p. 6838, 2022, doi: 10.1038/s41467-022-34640-8.

[99] N. C. Rockwell, L. Shang, S. S. Martin, and J. C. Lagarias, ‘Distinct classes of red/far-red photochemistry within the phytochrome superfamily’, *Proceedings of the National Academy of Sciences*, vol. 106, no. 15, pp. 6123–6127, Apr. 2009, doi: 10.1073/pnas.0902370106.

[100] K. Tang, H. M. Beyer, M. D. Zurbriggen, and W. Gärtner, ‘The Red Edge: Bilin-Binding Photoreceptors as Optogenetic Tools and Fluorescence Reporters.’, *Chem Rev*, vol. 121, no. 24, pp. 14906–14956, Dec. 2021, doi: 10.1021/acs.chemrev.1c00194.

[101] Y. Yang *et al.*, ‘Ultrafast proton-coupled isomerization in the phototransformation of phytochrome’, *Nat Chem*, vol. 14, no. 7, pp. 823–830, 2022, doi: 10.1038/s41557-022-00944-x.

[102] J. Y. Lin, ‘A user’s guide to channelrhodopsin variants: features, limitations and future developments.’, *Exp Physiol*, vol. 96, no. 1, pp. 19–25, Jan. 2011, doi: 10.1113/expphysiol.2009.051961.

[103] X. Yu, H. Liu, J. Klejnot, and C. Lin, ‘The Cryptochrome Blue Light Receptors.’, *Arabidopsis Book*, vol. 8, p. e0135, Sep. 2010, doi: 10.1199/tab.0135.

[104] M. Ahmad *et al.*, ‘Action spectrum for cryptochrome-dependent hypocotyl growth inhibition in Arabidopsis.’, *Plant Physiol*, vol. 129, no. 2, pp. 774–785, Jun. 2002, doi: 10.1104/pp.010969.

[105] N. Y. Jun and J. A. Cardin, ‘Activation of Distinct Channelrhodopsin Variants Engages Different Patterns of Network Activity’, *eNeuro*, vol. 7, no. 1, 2020, doi: 10.1523/ENEURO.0222-18.2019.

[106] C. A. Emerling, H. T. Huynh, M. A. Nguyen, R. W. Meredith, and M. S. Springer, ‘Spectral shifts of mammalian ultraviolet-sensitive pigments (short wavelength-sensitive opsin 1) are associated with eye length and photic niche evolution’, *Proceedings of the Royal Society B: Biological Sciences*, vol. 282, no. 1819, p. 20151817, 2015, doi: 10.1098/rspb.2015.1817.

[107] T. W. Cronin and M. J. Bok, ‘Photoreception and vision in the ultraviolet’, *Journal of Experimental Biology*, vol. 219, no. 18, pp. 2790–2801, 2016, doi: 10.1242/jeb.128769.

[108] T. Kyung *et al.*, ‘Optogenetic control of endogenous Ca2+ channels in vivo’, *Nat Biotechnol*, vol. 33, no. 10, pp. 1092–1096, 2015, doi: 10.1038/nbt.3350.

[109] A. S. Chuong *et al.*, ‘Noninvasive optical inhibition with a red-shifted microbial rhodopsin’, *Nat Neurosci*, vol. 17, no. 8, pp. 1123–1129, 2014, doi: 10.1038/nn.3752.

[110] R. A. Sharrock, ‘The phytochrome red/far-red photoreceptor superfamily’, *Genome Biol*, vol. 9, no. 8, p. 230, 2008, doi: 10.1186/gb-2008-9-8-230.

[111] L. Shi, L. A. Sordillo, A. Rodríguez-Contreras, and R. Alfano, ‘Transmission in near-infrared optical windows for deep brain imaging’, *J Biophotonics*, vol. 9, no. 1–2, pp. 38–43, 2016, doi: https://doi.org/10.1002/jbio.201500192.

[112] I.-W. Chen *et al.*, ‘In Vivo Submillisecond Two-Photon Optogenetics with Temporally Focused Patterned Light’, *Journal of Neuroscience*, vol. 39, no. 18, pp. 3484–3497, 2019, doi: 10.1523/JNEUROSCI.1785-18.2018.

[113] E. Chaigneau *et al.*, ‘Two-Photon Holographic Stimulation of ReaChR’, *Front Cell Neurosci*, vol. 10, 2016, doi: 10.3389/fncel.2016.00234.

[114] A. M. Packer, D. S. Peterka, J. J. Hirtz, R. Prakash, K. Deisseroth, and R. Yuste, ‘Two-photon optogenetics of dendritic spines and neural circuits’, *Nat Methods*, vol. 9, no. 12, pp. 1202–1205, 2012, doi: 10.1038/nmeth.2249.

[115] A. M. Packer, L. E. Russell, H. W. P. Dalgleish, and M. Häusser, ‘Simultaneous all-optical manipulation and recording of neural circuit activity with cellular resolution in vivo’, *Nat Methods*, vol. 12, no. 2, pp. 140–146, 2015, doi: 10.1038/nmeth.3217.

[116] R. Prakash *et al.*, ‘Two-photon optogenetic toolbox for fast inhibition, excitation and bistable modulation.’, *Nat Methods*, vol. 9, no. 12, pp. 1171–1179, Dec. 2012, doi: 10.1038/nmeth.2215.

[117] T. Fu *et al.*, ‘Exploring two-photon optogenetics beyond 1100 nm for specific and effective all-optical physiology’, *iScience*, vol. 24, no. 3, p. 102184, 2021, doi: https://doi.org/10.1016/j.isci.2021.102184.

[118] H. Yawo, R. Egawa, S. Hososhima, and L. Wen, ‘General Description: Future Prospects of Optogenetics’, in *Optogenetics: Light-Sensing Proteins and Their Applications*, H. Yawo, H. Kandori, and A. Koizumi, Eds., Tokyo: Springer Japan, 2015, pp. 111–131. doi: 10.1007/978-4-431-55516-2_8.

[119] B. Stüven, R. Stabel, R. Ohlendorf, J. Beck, R. Schubert, and A. Möglich, ‘Characterization and engineering of photoactivated adenylyl cyclases’, *Biol Chem*, vol. 400, no. 3, pp. 429–441, 2019.

[120] T. M. Wannier *et al.*, ‘Monomerization of far-red fluorescent proteins’, *Proceedings of the National Academy of Sciences*, vol. 115, no. 48, pp. E11294–E11301, 2018.

[121] K. Mishra, J. P. Fuenzalida-Werner, V. Ntziachristos, and A. C. Stiel, ‘Photocontrollable proteins for optoacoustic imaging’, *Anal Chem*, vol. 91, no. 9, pp. 5470–5477, 2019.

[122] J. R. Wagner, J. Zhang, J. S. Brunzelle, R. D. Vierstra, and K. T. Forest, ‘High resolution structure of Deinococcus bacteriophytochrome yields new insights into phytochrome architecture and evolution’, *Journal of biological chemistry*, vol. 282, no. 16, pp. 12298–12309, 2007.

[123] K. G. Chernov, T. A. Redchuk, E. S. Omelina, and V. V Verkhusha, ‘Near-infrared fluorescent proteins, biosensors, and optogenetic tools engineered from phytochromes’, *Chem Rev*, vol. 117, no. 9, pp. 6423–6446, 2017.

[124] H. Li, E. S. Burgie, Z. T. K. Gannam, H. Li, and R. D. Vierstra, ‘Plant phytochrome B is an asymmetric dimer with unique signalling potential’, *Nature*, vol. 604, no. 7904, pp. 127–133, 2022.

[125] D. M. Shcherbakova, M. Baloban, A. V Emelyanov, M. Brenowitz, P. Guo, and V. V Verkhusha, ‘Bright monomeric near-infrared fluorescent proteins as tags and biosensors for multiscale imaging’, *Nat Commun*, vol. 7, no. 1, p. 12405, 2016.

[126] N. C. Conley, S. W. Choi, and T. Buma, ‘Photoacoustic microscopy of lipids at 1.2 and 1.7 µm using a pulsed supercontinuum laser’, in *2017 IEEE International Ultrasonics Symposium (IUS)*, 2017, pp. 1–4. doi: 10.1109/ULTSYM.2017.8092147.

[127] S.-H. Chia *et al.*, ‘A sub-100fs self-starting Cr:forsterite laser generating 1.4W output power’, *Opt. Express*, vol. 18, no. 23, pp. 24085–24091, Nov. 2010, doi: 10.1364/OE.18.024085.

[128] A. A. Ivanov, G. N. Martynov, A. A. Lanin, A. B. Fedotov, and A. M. Zheltikov, ‘High-energy self-mode-locked Cr:forsterite laser near the soliton blowup threshold’, *Opt. Lett.*, vol. 45, no. 7, pp. 1890–1893, Apr. 2020, doi: 10.1364/OL.384850.

[129] R. Torres *et al.*, ‘Extension of high harmonic spectroscopy in molecules by a 1300 nm laser field’, *Opt. Express*, vol. 18, no. 3, pp. 3174–3180, Feb. 2010, doi: 10.1364/OE.18.003174.

[130] K. Piatkevich, F. Subach, and V. Verkhusha, ‘ChemInform Abstract: Engineering of Bacterial Phytochromes for Near-Infrared Imaging, Sensing, and Light-Control in Mammals’, *Chem Soc Rev*, vol. 42, Jan. 2013, doi: 10.1039/c3cs35458j.

[131] B. M. Teska, C. Li, B. C. Winn, K. K. Arthur, Y. Jiang, and J. P. Gabrielson, ‘Comparison of quantitative spectral similarity analysis methods for protein higher-order structure confirmation’, *Anal Biochem*, vol. 434, no. 1, pp. 153–165, 2013.

[132] E. S. Burgie, J. Zhang, and R. D. Vierstra, ‘Crystal structure of Deinococcus phytochrome in the photoactivated state reveals a cascade of structural rearrangements during photoconversion’, *Structure*, vol. 24, no. 3, pp. 448–457, 2016.

[133] K. D. Piatkevich *et al.*, ‘Near-infrared fluorescent proteins engineered from bacterial phytochromes in neuroimaging’, *Biophys J*, vol. 113, no. 10, pp. 2299–2309, 2017.

[134] K. A. Rumyantsev, D. M. Shcherbakova, N. I. Zakharova, A. V Emelyanov, K. K. Turoverov, and V. V Verkhusha, ‘Minimal domain of bacterial phytochrome required for chromophore binding and fluorescence’, *Sci Rep*, vol. 5, no. 1, p. 18348, 2015.

[135] Y. Hontani *et al.*, ‘Real-time observation of tetrapyrrole binding to an engineered bacterial phytochrome’, *Commun Chem*, vol. 4, no. 1, p. 3, 2021.

[136] N. M. Rzechorzek *et al.*, ‘A daily temperature rhythm in the human brain predicts survival after brain injury’, *Brain*, vol. 145, no. 6, pp. 2031–2048, Jun. 2022, doi: 10.1093/brain/awab466.

[137] E. S. Burgie *et al.*, ‘Differing biophysical properties underpin the unique signaling potentials within the plant phytochrome photoreceptor families’, *Proceedings of the National Academy of Sciences*, vol. 118, no. 22, p. e2105649118, 2021.

[138] I. Njimona, R. Yang, and T. Lamparter, ‘Temperature effects on bacterial phytochrome’, *PLoS One*, vol. 9, no. 10, p. e109794, 2014.

[139] A. S. Kalmbach and J. Waters, ‘Brain surface temperature under a craniotomy’, *J Neurophysiol*, vol. 108, no. 11, pp. 3138–3146, Sep. 2012, doi: 10.1152/jn.00557.2012.

[140] S. Ilic, S. Leichliter, J. Streeter, A. Oron, L. DeTaboada, and U. Oron, ‘Effects of power densities, continuous and pulse frequencies, and number of sessions of low-level laser therapy on intact rat brain.’, *Photomed Laser Surg*, vol. 24, no. 4, pp. 458–466, Aug. 2006, doi: 10.1089/pho.2006.24.458.

[141] D. Galiakhmetova *et al.*, ‘Ultra-Short Laser Pulses Propagation Through Mouse Head Tissues: Experimental and Computational Study’, *IEEE Journal of Selected Topics in Quantum Electronics*, vol. 29, no. 4: Biophotonics, pp. 1–11, 2023, doi: 10.1109/JSTQE.2022.3214788.

[142] K. Deisseroth, ‘Optogenetics: 10 years of microbial opsins in neuroscience’, *Nat Neurosci*, vol. 18, no. 9, pp. 1213–1225, 2015, doi: 10.1038/nn.4091.

[143] H.-J. Shim *et al.*, ‘Protocol for mouse optogenetic fMRI at ultrahigh magnetic fields’, *STAR Protoc*, vol. 3, no. 4, p. 101846, 2022.

[144] S. Chen, J. Haam, M. Walker, E. Scappini, J. Naughton, and N. P. Martin, ‘Recombinant viral vectors as neuroscience tools’, *Curr Protoc Neurosci*, vol. 87, no. 1, p. e67, 2019.

[145] K. Vlasov, C. J. Van Dort, and K. Solt, ‘Optogenetics and chemogenetics’, in *Methods in enzymology*, vol. 603, Elsevier, 2018, pp. 181–196.

[146] A. Guru, R. J. Post, Y.-Y. Ho, and M. R. Warden, ‘Making sense of optogenetics’, *International Journal of Neuropsychopharmacology*, vol. 18, no. 11, p. pyv079, 2015.

[147] S. J. Davis *et al.*, ‘Singlet Molecular Oxygen: from COIL Lasers to Photodynamic Cancer Therapy’, *J Phys Chem B*, vol. 127, no. 11, pp. 2289–2301, 2023.

[148] H. Hora and H. J. Schwarz, ‘Laser Interaction and Related Plasma Phenomena (Report on the 4th International Workshop, Troy, 1976)’, *Nuclear Fusion*, vol. 17, no. 1, p. 165, 1977.

[149] G. Parker, ‘Encyclopedia of materials: science and technology’, 2001.

[150] T. C. Huang, Q. He, X. W. Shu, and C. Liu, ‘Characteristic analysis of praseodymium doped superfluorescent fluoride fiber source operating at 1.3 μm’, *Opt Quantum Electron*, vol. 48, pp. 1–11, 2016.

[151] M. A. Casas-Ramos, G. E. Sandoval-Romero, V. Argueta-Diaz, and E. F. Pinzon-Escobar, ‘Experimental results: spectrum output analysis of an EDFA with yterrbium-oped fiber using a superluminescent diode source’, *Revista mexicana de física*, vol. 62, no. 6, pp. 565–569, 2016.

[152] Y. Wang, S. Wang, A. Halder, and J. Sahu, ‘Bi-doped optical fibers and fiber amplifiers’, *Optical Materials: X*, vol. 17, p. 100219, 2023.

[153] H. Luo, L. Zhan, Z. Wang, L. Zhang, C. Feng, and X. Shen, ‘All-Fiber Generation of Sub-30 fs Pulses at 1.3-μm via Cherenkov Radiation With Entire Dispersion Management’, *Journal of Lightwave Technology*, vol. 35, no. 11, pp. 2325–2330, 2017.

[154] D. A. Sidorov-Biryukov, K. A. Kudinov, A. A. Podshivalov, and A. M. Zheltikov, ‘Widely tunable 70-MHz near-infrared source of ultrashort pulses based on a mode-locked

ytterbium laser and a photonic-crystal fiber', *Laser Phys Lett*, vol. 7, no. 5, p. 355, Mar. 2010, doi: 10.1002/lapl.200910157.

[155] M. J. Guy, D. U. Noske, A. Boskovic, and J. R. Taylor, 'Femtosecond soliton generation in a praseodymium fluoride fiber laser', *Opt. Lett.*, vol. 19, no. 11, pp. 828–830, Jun. 1994, doi: 10.1364/OL.19.000828.

[156] Yong-Won Song, S. Y. Set, S. Yamashita, C. S. Goh, and T. Kotake, '1300-nm pulsed fiber lasers mode-locked by purified carbon nanotubes', *IEEE Photonics Technology Letters*, vol. 17, no. 8, pp. 1623–1625, Aug. 2005, doi: 10.1109/LPT.2005.850883.

[157] D. Galiakhmetova *et al.*, 'Direct measurement of carbon nanotube temperature between fiber ferrules as a universal tool for saturable absorber stability investigation', *Carbon N Y*, vol. 184, pp. 941–948, 2021, doi: https://doi.org/10.1016/j.carbon.2021.08.032.

[158] H. Ahmad, S. N. Aidit, and Z. C. Tiu, 'Multi-wavelength Praseodymium fiber laser using stimulated Brillouin scattering', *Opt Laser Technol*, vol. 99, pp. 52–59, Feb. 2018, doi: 10.1016/j.optlastec.2017.09.044.

[159] G. P. Agrawal, 'Nonlinear fiber optics', in *Nonlinear Science at the Dawn of the 21st Century*, Springer, 2000, pp. 195–211.

[160] N. K. Thipparapu, Y. Wang, S. Wang, A. A. Umnikov, P. Barua, and J. K. Sahu, 'Bi-doped fiber amplifiers and lasers', *Opt. Mater. Express*, vol. 9, no. 6, pp. 2446–2465, Jun. 2019, doi: 10.1364/OME.9.002446.

[161] I. A. Bufetov *et al.*, 'Efficient bi-doped fiber lasers and amplifiers for the spectral region 1300-1500 nm', in *Proc.SPIE*, Feb. 2010. doi: 10.1117/12.840666.

[162] R. Gumenyuk, J. Puustinen, A. V Shubin, I. A. Bufetov, E. M. Dianov, and O. G. Okhotnikov, '1.32 um mode-locked bismuth-doped fiber laser operating in anomalous and normal dispersion regimes', *Opt. Lett.*, vol. 38, no. 20, pp. 4005–4007, Oct. 2013, doi: 10.1364/OL.38.004005.

[163] N. K. Thipparapu, C. Guo, A. A. Umnikov, P. Barua, A. Taranta, and J. K. Sahu, 'Bismuth-doped all-fiber mode-locked laser operating at 1340 nm', *Opt. Lett.*, vol. 42, no. 24, pp. 5102–5105, Dec. 2017, doi: 10.1364/OL.42.005102.

[164] H.-Y. Wang, S.-W. Huang, D.-R. Li, B.-S. Lin, and M.-C. Chan, 'Nonlinear Light Microscopy by a 1.2 um Fiber-Laser-Based Femtosecond Dispersive Wave Source', *IEEE Photonics J*, vol. 7, no. 3, pp. 1–8, 2015, doi: 10.1109/JPHOT.2015.2432077.

[165] Y. Qin, Y.-H. Ou, B. Cromey, O. Batjargal, J. K. Barton, and K. Kieu, 'Watt-level all-fiber optical parametric chirped-pulse amplifier working at 1300 nm.', *Opt Lett*, vol. 44, no. 14, pp. 3422–3425, Jul. 2019, doi: 10.1364/OL.44.003422.

[166] P. Muniz-Cánovas, Y. O. Barmenkov, A. V Kir'yanov, J. L. Cruz, and M. V Andrés, 'Ytterbium-doped fiber laser as pulsed source of narrowband amplified spontaneous emission', *Sci Rep*, vol. 9, no. 1, p. 13073, 2019, doi: 10.1038/s41598-019-49695-9.

[167] A. F. J. Runge, C. Aguergaray, R. Provo, M. Erkintalo, and N. G. R. Broderick, 'All-normal dispersion fiber lasers mode-locked with a nonlinear amplifying loop mirror', *Optical Fiber Technology*, vol. 20, no. 6, pp. 657–665, 2014, doi: https://doi.org/10.1016/j.yofte.2014.07.010.

[168] P. Bowen, H. Singh, A. Runge, R. Provo, and N. G. R. Broderick, 'Mode-locked femtosecond all-normal all-PM Yb-doped fiber laser at 1060 nm', *Opt Commun*, vol. 364, pp. 181–184, 2016.

[169] Y. S. Fedotov, A. V Ivanenko, S. M. Kobtsev, and S. V Smirnov, ‘High average power mode-locked figure-eight Yb fibre master oscillator’, *Opt Express*, vol. 22, no. 25, pp. 31379–31386, 2014.

[170] M. Fernandez-Vallejo, S. Rota-Rodrigo, and M. Lopez-Amo, ‘Comparative study of ring and random cavities for fiber lasers’, *Appl Opt*, vol. 53, no. 16, pp. 3501–3507, 2014.

[171] V. F. Pecile, A. S. Mayer, J. K. C. Ballentin, and O. H. Heckl, ‘Amplitude noise suppression in Yb: doped NALM oscillators utilizing saturable absorber settings’, *Opt Express*, vol. 31, no. 22, pp. 36824–36835, 2023.

[172] A. S. Mayer *et al.*, ‘Flexible all-PM NALM Yb: fiber laser design for frequency comb applications: operation regimes and their noise properties’, *Opt Express*, vol. 28, no. 13, pp. 18946–18968, 2020.

[173] J.-H. Lin *et al.*, ‘Noise-like pulse generation around 1.3-μm based on cascaded Raman scattering’, *Opt Express*, vol. 28, no. 8, pp. 12252–12261, 2020.

[174] P. Sidorenko, W. Fu, and F. Wise, ‘Nonlinear ultrafast fiber amplifiers beyond the gain-narrowing limit’, *Optica*, vol. 6, no. 10, pp. 1328–1333, 2019.

[175] P. M. Ferlay J, Ervik M, Lam F, Colombet M, Mery L, ‘Global Cancer Observatory: Cancer Today. Lyon: International Agency for Research on Cancer’. 2020.

[176] Max Roser and Hannah Ritchie, ‘Cancer’, *Our World in Data*, 2015.

[177] National Cancer Institute, ‘Age and Cancer Risk’. 2021.

[178] H. M. Bruins, K. K. H. Aben, T. J. Arends, A. G. van der Heijden, and A. J. Witjes, ‘The effect of the time interval between diagnosis of muscle-invasive bladder cancer and radical cystectomy on staging and survival: A Netherlands Cancer Registry analysis’, *Urologic Oncology: Seminars and Original Investigations*, vol. 34, no. 4, pp. 166.e1-166.e6, Apr. 2016, doi: 10.1016/j.urolonc.2015.11.006.

[179] B. Gramatikov, ‘“Handbook of biomedical optics”, edited by David A. Boas, Constantinos Pitris, and Nimmi Ramanujam’, *Biomed Eng Online*, vol. 11, Feb. 2012, doi: 10.1186/1475-925X-11-7.

[180] K. S. Litvinova, I. E. Rafailov, A. V. Dunaev, S. G. Sokolovski, and E. U. Rafailov, ‘Non-invasive biomedical research and diagnostics enabled by innovative compact lasers’, *Progress in Quantum Electronics*, vol. 56. Elsevier Ltd, pp. 1–14, Nov. 01, 2017. doi: 10.1016/j.pquantelec.2017.10.001.

[181] F. LaRocca, D. Nankivil, S. Farsiu, and J. A. Izatt, ‘True color scanning laser ophthalmoscopy and optical coherence tomography handheld probe’, *Biomed. Opt. Express*, vol. 5, no. 9, pp. 3204–3216, Sep. 2014, doi: 10.1364/BOE.5.003204.

[182] D. Coca, Y. Zheng, J. E. W. Mayhew, and S. A. Billings, ‘Nonlinear system identification and analysis of complex dynamical behaviour in reflected light measurements of vasomotion’, *International Journal of Bifurcation and Chaos*, vol. 10, no. 02, pp. 461–476, Feb. 2000, doi: 10.1142/S021812740000030X.

[183] A. Sharma, Srishti, V. Periyasamy, and M. Pramanik, ‘Photoacoustic imaging depth comparison at 532-, 800-, and 1064-nm wavelengths: Monte Carlo simulation and experimental validation’, *J Biomed Opt*, vol. 24, no. 12, p. 121904, 2019.

[184] Q. Li *et al.*, 'An 800 nm driven NaErF 4@ NaLuF 4 upconversion platform for multimodality imaging and photodynamic therapy', *Nanoscale*, vol. 10, no. 26, pp. 12356–12363, 2018.

[185] X. Xie *et al.*, 'Emerging≈ 800 nm excited lanthanide-doped upconversion nanoparticles', *Small*, vol. 13, no. 6, p. 1602843, 2017.

[186] W. R. Zipfel, R. M. Williams, R. Christie, A. Y. Nikitin, B. T. Hyman, and W. W. Webb, 'Live tissue intrinsic emission microscopy using multiphoton-excited native fluorescence and second harmonic generation', *Proceedings of the National Academy of Sciences*, vol. 100, no. 12, pp. 7075–7080, 2003.

[187] E. Dimitrow *et al.*, 'Spectral fluorescence lifetime detection and selective melanin imaging by multiphoton laser tomography for melanoma diagnosis', *Exp Dermatol*, vol. 18, no. 6, pp. 509–515, 2009.

[188] W. J. Choi and R. K. Wang, 'Swept-source optical coherence tomography powered by a 1.3-μm vertical cavity surface emitting laser enables 2.3-mm-deep brain imaging in mice in vivo', *J Biomed Opt*, vol. 20, no. 10, p. 106004, 2015.

[189] M. Yamanaka, T. Teranishi, H. Kawagoe, and N. Nishizawa, 'Optical coherence microscopy in 1700 nm spectral band for high-resolution label-free deep-tissue imaging.', *Sci Rep*, vol. 6, p. 31715, Aug. 2016, doi: 10.1038/srep31715.

[190] S. Kurilchik *et al.*, 'Advanced multimodal laser imaging tool for urothelial carcinoma diagnosis (AMPLITUDE)', *JPhys Photonics*, vol. 2, no. 2, 2020, doi: 10.1088/2515-7647/ab7bab.

[191] L. A. Sordillo, Y. Pu, S. Pratavieira, Y. Budansky, and R. R. Alfano, 'Deep optical imaging of tissue using the second and third near-infrared spectral windows', *J Biomed Opt*, vol. 19, no. 5, pp. 1–6, May 2014, doi: 10.1117/1.JBO.19.5.056004.

[192] M. A. Yaseen *et al.*, 'Fluorescence lifetime microscopy of NADH distinguishes alterations in cerebral metabolism in vivo', *Biomed Opt Express*, vol. 8, no. 5, pp. 2368–2385, 2017.

[193] Q. Wang, T. Chen, B. Zhang, M. Li, Y. Lu, and K. P. Chen, 'All-fiber passively mode-locked thulium-doped fiber ring laser using optically deposited graphene saturable absorbers', *Appl Phys Lett*, vol. 102, no. 13, 2013, doi: 10.1063/1.4800036.

[194] F. Xia, C. Wu, D. Sinefeld, B. Li, Y. Qin, and C. Xu, 'In vivo label-free confocal imaging of the deep mouse brain with long-wavelength illumination', *Biomed. Opt. Express*, vol. 9, no. 12, pp. 6545–6555, Dec. 2018, doi: 10.1364/BOE.9.006545.

[195] H. Cheng *et al.*, 'Deep-brain 2-photon fluorescence microscopy in vivo excited at the 1700 nm window', *Opt. Lett.*, vol. 44, no. 17, pp. 4432–4435, Sep. 2019, doi: 10.1364/OL.44.004432.

[196] M. Yamanaka, N. Hayakawa, and N. Nishizawa, 'High-spatial-resolution deep tissue imaging with spectral-domain optical coherence microscopy in the 1700-nm spectral band', *J Biomed Opt*, vol. 24, no. 7, pp. 1–4, Jul. 2019, doi: 10.1117/1.JBO.24.7.070502.

[197] R. Phelan *et al.*, 'Mid-infrared InP-based discrete mode laser diodes', *Optical Fiber Applications*, p. 15, 2019.

[198] S.-H. Jeong, T. Mizumoto, M. Takenaka, and Y. Nakano, 'All-optical wavelength conversion in a GaInAsP/InP optical gate loaded with a Bragg reflector', *Appl Opt*, vol. 42, no. 33, pp. 6672–6677, 2003.

[199] M. Guina, A. Rantamäki, and A. Härkönen, 'Optically pumped VECSELs: review of technology and progress', *J Phys D Appl Phys*, vol. 50, no. 38, p. 383001, 2017.

[200] L. Xu *et al.*, 'Yb-fiber amplifier pumped idler-resonant PPLN optical parametric oscillator producing 90 femtosecond pulses with high beam quality', *Applied Physics B*, vol. 117, no. 4, pp. 987–993, 2014, doi: 10.1007/s00340-014-5918-7.

[201] J. Krauth, A. Steinmann, R. Hegenbarth, M. Conforti, and H. Giessen, 'Broadly tunable femtosecond near- and mid-IR source by direct pumping of an OPA with a 41.7 MHz Yb:KGW oscillator', *Opt. Express*, vol. 21, no. 9, pp. 11516–11522, May 2013, doi: 10.1364/OE.21.011516.

[202] J. Fan *et al.*, 'Dielectric-mirror-less femtosecond optical parametric oscillator with ultrabroad-band tunability', *Opt. Lett.*, vol. 43, no. 10, pp. 2316–2319, May 2018, doi: 10.1364/OL.43.002316.

[203] Y.-W. Tzeng *et al.*, 'High repetition rate optical parametric amplification based on a single Yb:fiber laser', in *Conference on Lasers and Electro-Optics/International Quantum Electronics Conference*, Optical Society of America, 2009, p. CWJ7. doi: 10.1364/CLEO.2009.CWJ7.

[204] L. Kiani, T. Lu, and J. E. Sharping, 'Comparison of amplitude noise of a fiber-optical parametric oscillator and a supercontinuum source', *J. Opt. Soc. Am. B*, vol. 31, no. 8, pp. 1986–1990, Aug. 2014, doi: 10.1364/JOSAB.31.001986.

[205] L. R. Marshall, J. Kasinski, A. D. Hays, and R. Burnham, 'Efficient optical parametric oscillator at 1.6 μm', *Opt. Lett.*, vol. 16, no. 9, pp. 681–683, May 1991, doi: 10.1364/OL.16.000681.

[206] M. V O'Connor *et al.*, 'Synchronously pumped optical parametric oscillator driven by a femtosecond mode-locked fiber laser', *Opt. Lett.*, vol. 27, no. 12, pp. 1052–1054, Jun. 2002, doi: 10.1364/OL.27.001052.

[207] M. Kirchner *et al.*, 'Ultrafast Optical Parametric Oscillator Pumped by an All Normal Dispersion (ANDi) Yb: Fiber Oscillator', in *Conference on Lasers and Electro-Optics 2012*, Optical Society of America, 2012, p. CM1B.1. doi: 10.1364/CLEO_SI.2012.CM1B.1.

[208] H. Linnenbank and S. Linden, 'High repetition rate femtosecond double pass optical parametric generator with more than 2 W tunable output in the NIR', *Opt. Express*, vol. 22, no. 15, pp. 18072–18077, Jul. 2014, doi: 10.1364/OE.22.018072.

[209] X. Meng, Z. Wang, W. Tian, H. He, S. Fang, and Z. Wei, 'Watt-level widely tunable femtosecond mid-infrared KTiOAsO4 optical parametric oscillator pumped by a 1.03 μm Yb:KGW laser', *Opt. Lett.*, vol. 43, no. 4, pp. 943–946, Feb. 2018, doi: 10.1364/OL.43.000943.

[210] F. Mörz, T. Steinle, A. Steinmann, and H. Giessen, 'Multi-Watt femtosecond optical parametric master oscillator power amplifier at 43 MHz', *Opt. Express*, vol. 23, no. 18, pp. 23960–23967, Sep. 2015, doi: 10.1364/OE.23.023960.

[211] T. Steinle, F. Mörz, A. Steinmann, and H. Giessen, 'Ultra-stable high average power femtosecond laser system tunable from 1.33 to 20 μm', *Opt. Lett.*, vol. 41, no. 21, pp. 4863–4866, Nov. 2016, doi: 10.1364/OL.41.004863.

[212] T. Noronen, S. Firstov, E. Dianov, and O. G. Okhotnikov, ‘1700 nm dispersion managed mode-locked bismuth fiber laser’, *Sci Rep*, vol. 6, no. 1, p. 24876, 2016, doi: 10.1038/srep24876.

[213] G.-R. Lin, J.-Y. Chang, Y.-S. Liao, and H.-H. Lu, ‘L-band erbium-doped fiber laser with coupling-ratio controlled wavelength tunability’, *Opt Express*, vol. 14, no. 21, pp. 9743–9749, 2006.

[214] T. Noronen, O. Okhotnikov, and R. Gumenyuk, ‘Electronically tunable thulium-holmium mode-locked fiber laser for the 1700-1800 nm wavelength band’, *Opt. Express*, vol. 24, no. 13, pp. 14703–14708, Jun. 2016, doi: 10.1364/OE.24.014703.

[215] C. Li *et al.*, ‘High-energy all-fiber gain-switched thulium-doped fiber laser for volumetric photoacoustic imaging of lipids’, *Photonics Res*, vol. 8, no. 2, pp. 160–164, 2020.

[216] S. D. Emami, M. M. Dashtabi, H. J. Lee, A. S. Arabanian, and H. A. A. Rashid, ‘1700 nm and 1800 nm band tunable thulium doped mode-locked fiber lasers’, *Sci Rep*, vol. 7, no. 1, p. 12747, 2017, doi: 10.1038/s41598-017-13200-x.

[217] X. Quan, R. Ma, H. Wu, Z. Y. Bai, D. Y. Fan, and J. Liu, ‘Low threshold and high spectral purity 1.7 µm random fiber laser based on hybrid gain’, *Opt Laser Technol*, vol. 155, p. 108410, 2022.

[218] A. Khegai, M. Melkumov, K. Riumkin, V. Khopin, S. Firstov, and E. Dianov, ‘NALM-based bismuth-doped fiber laser at 1.7 um’, *Opt. Lett.*, vol. 43, no. 5, pp. 1127–1130, Mar. 2018, doi: 10.1364/OL.43.001127.

[219] K. Li, Q. Huang, J. Jiang, Z. Huang, and C. Mou, ‘Wavelength-tunable L-band high repetition rate erbium-doped fiber laser based on dissipative four-wave mixing’, *Sensors*, vol. 21, no. 17, p. 5975, 2021.

[220] R. Becheker *et al.*, ‘High-energy dissipative soliton-driven fiber optical parametric oscillator emitting at 1.7 µm’, *Laser Phys Lett*, vol. 15, no. 11, p. 115103, 2018, doi: 10.1088/1612-202X/aadfcd.

[221] L. Vazquez-Zuniga and Y. Jeong, ‘Super-Broadband Noise-Like Pulse Erbium-Doped Fiber Ring Laser With a Highly Nonlinear Fiber for Raman Gain Enhancement’, *IEEE Photonics Technology Letters*, vol. 24, pp. 1549–1551, Sep. 2012, doi: 10.1109/LPT.2012.2208451.

[222] H. Li, W. Pei, W. Huang, M. Wang, and Z. Wang, ‘Highly Efficient Nanosecond 1.7 µm Fiber Gas Raman Laser by H2-Filled Hollow-Core Photonic Crystal Fibers’, *Crystals (Basel)*, vol. 11, p. 32, Dec. 2020, doi: 10.3390/cryst11010032.

[223] A. Zach, M. Mohseni, C. Polzer, J. W. Nicholson, and T. Hellerer, ‘All-fiber widely tunable ultrafast laser source for multimodal imaging in nonlinear microscopy’, *Opt Lett*, vol. 44, no. 21, pp. 5218–5221, 2019.

[224] X. Fang, Z. Wang, and L. Zhan, ‘Efficient generation of all-fiber femtosecond pulses at 1.7 µm via soliton self-frequency shift’, *Optical Engineering*, vol. 56, p. 046107, Apr. 2017, doi: 10.1117/1.OE.56.4.046107.

[225] J. Zeng, A. E. Akosman, and M. Y. Sander, ‘Supercontinuum Generation From a Thulium Ultrafast Fiber Laser in a High NA Silica Fiber’, *IEEE Photonics Technology Letters*, vol. 31, no. 22, pp. 1787–1790, 2019, doi: 10.1109/LPT.2019.2946835.

[226] L. Jiang, R. Song, J. He, and J. Hou, ‘714 W all-fiber supercontinuum generation from an ytterbium-doped fiber amplifier’, *Opt Laser Technol*, vol. 161, p. 109168, 2023, doi: https://doi.org/10.1016/j.optlastec.2023.109168.

[227] J. Takayanagi, N. Nishizawa, H. Nagai, M. Yoshida, and T. Goto, ‘Generation of high-power femtosecond pulse and octave-spanning ultrabroad supercontinuum using all-fiber system’, *IEEE Photonics Technology Letters*, vol. 17, no. 1, pp. 37–39, Jan. 2005, doi: 10.1109/LPT.2004.837741.

[228] N. S. Shahabuddin *et al.*, ‘Supercontinuum generation using a passive mode-locked stretched-pulse bismuth-based erbium-doped fiber laser’, *Opt Laser Technol*, vol. 44, no. 4, pp. 741–743, 2012.

[229] X. Ma, ‘Nonlinear effects-based 1.7 μm fiber lasers: A review and prospect’, *MATEC Web Conf.*, vol. 382, 2023, doi: 10.1051/matecconf/202338201028.

[230] S. K. O. Soman, ‘A tutorial on fiber Kerr nonlinearity effect and its compensation in optical communication systems’, *Journal of Optics*, vol. 23, no. 12, p. 123502, 2021.

[231] G. P. Agrawal, ‘Nonlinear fiber optics: its history and recent progress’, *JOSA B*, vol. 28, no. 12, pp. A1–A10, 2011.

[232] S. V Firstov *et al.*, ‘Laser-Active Fibers Doped With Bismuth for a Wavelength Region of 1.6–1.8 μm’, *IEEE Journal of Selected Topics in Quantum Electronics*, vol. 24, no. 5, pp. 1–15, 2018, doi: 10.1109/JSTQE.2018.2801461.

[233] R. Billington, ‘A report of four-wave mixing in optical fibre and its metrological applications.’, 1999.

[234] L. Sirleto and M. A. Ferrara, ‘Fiber amplifiers and fiber lasers based on stimulated Raman scattering: a review’, *Micromachines (Basel)*, vol. 11, no. 3, p. 247, 2020.

[235] X. He *et al.*, ‘Robust 1.7-um, all-polarization-maintaining femtosecond fiber laser source based on standard telecom fibers’, *Applied Physics Express*, vol. 12, no. 7, p. 72007, Jul. 2019, doi: 10.7567/1882-0786/ab266f.

[236] V. V Alexander *et al.*, ‘Modulation instability initiated high power all-fiber supercontinuum lasers and their applications’, *Optical Fiber Technology*, vol. 18, no. 5, pp. 349–374, 2012, doi: https://doi.org/10.1016/j.yofte.2012.07.014.

[237] J. W. Nicholson, A. D. Yablon, P. S. Westbrook, K. S. Feder, and M. F. Yan, ‘High power, single mode, all-fiber source of femtosecond pulses at 1550 nm and its use in supercontinuum generation’, *Opt. Express*, vol. 12, no. 13, pp. 3025–3034, Jun. 2004, doi: 10.1364/OPEX.12.003025.

[238] C. Xia *et al.*, ‘Supercontinuum Generation in Silica Fibers by Amplified Nanosecond Laser Diode Pulses’, *IEEE Journal of Selected Topics in Quantum Electronics*, vol. 13, no. 3, pp. 789–797, May 2007, doi: 10.1109/JSTQE.2007.897414.

[239] X. Li, P. Zhang, D. Wu, K. Han, S. Tong, and H. Jiang, ‘Single-/dual-pulse repetition rate variable supercontinuum light source with peak wavelength around 1.7 {\textmu}m using a modulated pump’, *Appl. Opt.*, vol. 59, no. 11, pp. 3458–3466, Apr. 2020, doi: 10.1364/AO.387225.

[240] G. Lopez-Galmiche *et al.*, ‘Visible supercontinuum generation in a graded index multimode fiber pumped at 1064 nm’, *Opt. Lett.*, vol. 41, no. 11, pp. 2553–2556, Jun. 2016, doi: 10.1364/OL.41.002553.

[241] A. Kudlinski *et al.*, ‘Zero-dispersion wavelength decreasing photonic crystal fibers for ultraviolet-extended supercontinuum generation’, *Opt. Express*, vol. 14, no. 12, pp. 5715–5722, Jun. 2006, doi: 10.1364/OE.14.005715.

[242] J. M. Stone and J. C. Knight, ‘Visibly “white” light generation in uniform photonic crystal fiber using a microchip laser’, *Opt. Express*, vol. 16, no. 4, pp. 2670–2675, Feb. 2008, doi: 10.1364/OE.16.002670.

[243] W. Drexler and J. G. Fujimoto, *Optical Coherence Tomography*. 2008.

[244] V. Ivanov, ‘Compact optical grating compressor’, *Opt Express*, vol. 30, no. 20, pp. 35338–35347, 2022.

[245] D. Stoliarov, A. Koviarov, D. Korobko, D. Galiakhmetova, and E. Rafailov, ‘Fibre laser system with wavelength tuning in extended telecom range’, *Optical Fiber Technology*, vol. 72, p. 102994, 2022.

[246] K. Wang, N. G. Horton, K. Charan, and C. Xu, ‘Advanced fiber soliton sources for nonlinear deep tissue imaging in biophotonics’, *IEEE Journal of Selected Topics in Quantum Electronics*, vol. 20, no. 2, pp. 50–60, 2013.

[247] S. Tong, X. Chen, J. Li, P. Qiu, and K. Wang, ‘Elliptically-polarized soliton self-frequency shift in isotropic optical fiber’, *Journal of Lightwave Technology*, vol. 39, no. 5, pp. 1334–1339, 2020.

[248] J. Martorell, R. Vilaseca, and R. Corbalan, ‘Second harmonic generation in a photonic crystal’, *Appl Phys Lett*, vol. 70, no. 6, pp. 702–704, 1997.

[249] L. E. Myers and W. R. Bosenberg, ‘Periodically poled lithium niobate and quasi-phase-matched optical parametric oscillators’, *IEEE J Quantum Electron*, vol. 33, no. 10, pp. 1663–1672, 1997.

[250] I. A. Ghambaryan, R. Guo, R. K. Hovsepyan, A. R. Poghosyan, E. S. Vardanyan, and V. G. Lazaryan, ‘Periodically poled structures in lithium niobate crystals: growth and photoelectric properties.’, *Journal of Optoelectronics and Advanced Materials*, vol. 5, no. 1, pp. 61–68, 2003.

[251] G. A. Blab, P. H. M. Lommerse, L. Cognet, G. S. Harms, and T. Schmidt, ‘Two-photon excitation action cross-sections of the autofluorescent proteins’, *Chem Phys Lett*, vol. 350, no. 1–2, pp. 71–77, 2001.

[252] K. Schenke-Layland, ‘Non-invasive multiphoton imaging of extracellular matrix structures’, *J Biophotonics*, vol. 1, no. 6, pp. 451–462, 2008.

[253] S. W. Perry, R. M. Burke, and E. B. Brown, ‘Two-photon and second harmonic microscopy in clinical and translational cancer research’, *Ann Biomed Eng*, vol. 40, pp. 277–291, 2012.

[254] T. Bernas, M. Zarębski, R. R. Cook, and J. W. Dobrucki, ‘Minimizing photobleaching during confocal microscopy of fluorescent probes bound to chromatin: role of anoxia and photon flux’, *J Microsc*, vol. 215, no. 3, pp. 281–296, 2004.

[255] N. S. James, R. R. Cheruku, J. R. Missert, U. Sunar, and R. K. Pandey, ‘Measurement of cyanine dye photobleaching in photosensitizer cyanine dye conjugates could help in optimizing light dosimetry for improved photodynamic therapy of cancer’, *Molecules*, vol. 23, no. 8, p. 1842, 2018.

[256] D. Yova, V. Hovhannisyan, and T. Theodossiou, ‘Photochemical effects and hypericin photosensitized processes in collagen’, *J Biomed Opt*, vol. 6, no. 1, pp. 52–57, 2001.

[257] R. Niesner, V. Andresen, J. Neumann, H. Spiecker, and M. Gunzer, ‘The power of single and multibeam two-photon microscopy for high-resolution and high-speed deep tissue and intravital imaging’, *Biophys J*, vol. 93, no. 7, pp. 2519–2529, 2007.

[258] O. A. Shemesh *et al.*, ‘Temporally precise single-cell-resolution optogenetics’, *Nat Neurosci*, vol. 20, no. 12, pp. 1796–1806, 2017.